11th DELTA
User Meeting

&

Annual Report 2015

Dortmund
25. November 2015

Edited by C. Sternemann, R. Wagner,
D. Lützenkirchen-Hecht (2015)

Preface

Dear reader, dear colleague,

again a successful year of DELTA operation has almost finished, meanwhile researchers from several different institutions have carried out their experiments using the instruments at the DELTA beamlines, with contributions in chemistry, biology, physics, materials and accelerator science. Those activities are visible in peer-reviewed publications and numerous conference talks and posters, for example on the 12th International Conference on Synchrotron Radiation Instrumentation in New York in July, the 16th International Conference on X-ray Absorption Fine Structure in Karlsruhe in August, or the 9th International Conference on Inelastic X-ray Scattering in Hsinchu, Taiwan, to mention just a few. This annual report is a collection of the various activities of the past year and is also meant as an overview of possible applications using synchrotron radiation from DELTA.

The success of DELTA is closely related to the high motivation and engagement of all the staff members of the synchrotron who all have contributed in many ways to the success of each individual project. Not to forget the educational mission of DELTA, giving young scientists unique opportunities for the development of their own research, and leading to many successful thesis works each year.

Last not least we would like to thank for the manifold support of DELTA by the involved universities and research institutions, the different funding agencies and the local government. We are looking forward to the upcoming beamtime periods, hoping that they will be as productive and successful as during the past year!

Christian Sternemann, Ralph Wagner & Dirk Lützenkirchen-Hecht

Contents:

Instrumentation

Transmission mode XAFS data acquisition with the Pilatus 100 K detector at DELTA beamline 10

Dirk Lützenkirchen-Hecht, Jan-Christoph Gasse, Raphael Bögel, Ralph Wagner, Ronald Frahm

Fachbereich C - Physik, Bergische Universität Wuppertal, Gaußstr. 20, 42097 Wuppertal, Germany.

Transmission mode EXAFS measurements of inhomogeneous samples (lateral variation of thickness, composition, holes, etc.) may show severely distorted EXAFS spectra. Holes in the area transmitted by the X-ray beam lead to substantially damped EXAFS oscillations compared to a perfect sample, because commonly used ionization chambers measure an absorption signal averaged over the illuminated sample region. The determined coordination numbers and Debye-Waller factors are thus erroneous [1]. In the case of ex-situ experiments, a careful sample preparation may prevent such artifacts. In the case of in-situ studies, however, the sample often changes inhomogeneously as a result of the applied reaction conditions e.g. in catalysis [2] or electrochemistry [3], where the reactions are generally initiated at the sample surfaces in contact with a reactive medium.

In this contribution, we have thus explored the feasibility of transmission mode EXAFS experiments using the Pilatus 100 K detector [4] at DELTA beamline 10. Incident and transmitted intensities from the sample were monitored by N_2-filled ionization chambers, and the 2D-detector was placed behind the second ionization chamber in order to measure the lateral distribution of the transmitted X-rays.

In Fig. 1(a), the intensity distribution behind a Co metal foil on the Pilatus detector measured for a photon energy of 7600 eV is shown. From the size of the X-ray beam of about 7 mm width and 1 mm height corresponds to about 40 lines of 6 pixels each, and is well in accordance with the size of the detector pixels of 176 µm [4]. In figure 1(b), the raw absorption data measured using the ionization chambers are compared to different areas of the pixel detector. As can be seen, the data quality of a spectrum calculated from a single pixel is excellent with respect to the reproduction of sharp absorption features close to the edge as well as to the low noise of the k^3-weighted $\chi(k)$ data depicted in figure 1(c). Furthermore, the data quality slightly improves if a vertical cross section of the beam, i.e. a line of 6 pixels, is used for the calculation of an absorption spectrum.

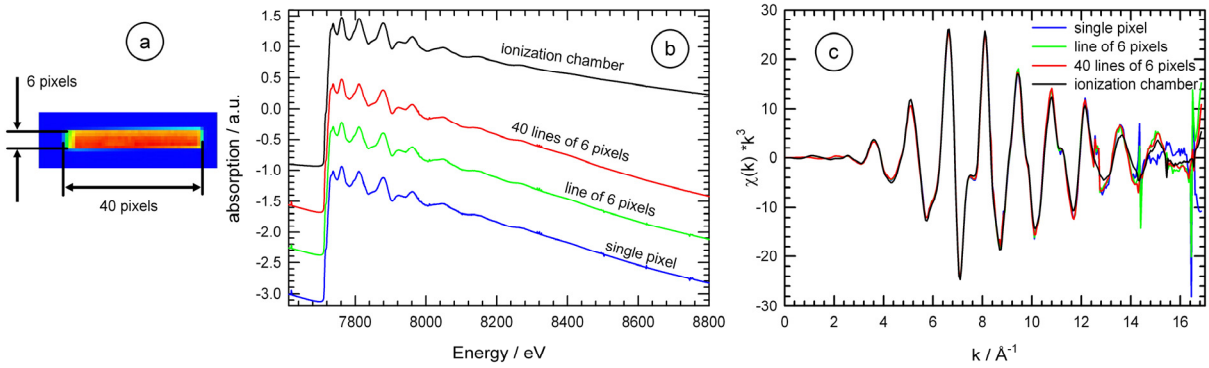

Fig. 1: (a) Intensity distribution downstream a Co metal foil on the Pilatus detector measured at E = 7600 eV. (b) Comparison of the K-edge X-ray absorption spectrum of a Co metal foil measured in transmission at room temperature using ionization chambers as detectors (—) and using the intensities on the 2D-detector (1 s / point). Different regions of this detector were used for the spectrum calculation: a single pixel (—), a vertical cross section of 6 pixels (—) and the entire illuminated area (40x6 pixel, —). (c) k^3-weighted EXAFS oscillations $\chi(k) * k^3$ for the different spectra depicted in (b).

If the entire region of the sample that is illuminated from the beam is taken into consideration (40 lines of 6 pixels = 240 pixels), the obtained spectrum is almost indistinguishable to that from the ionization chamber. At least up to ca. 12 $Å^{-1}$, no substantial differences can be seen in the extracted $\chi(k)*k^3$ data (see figure 1(c)).

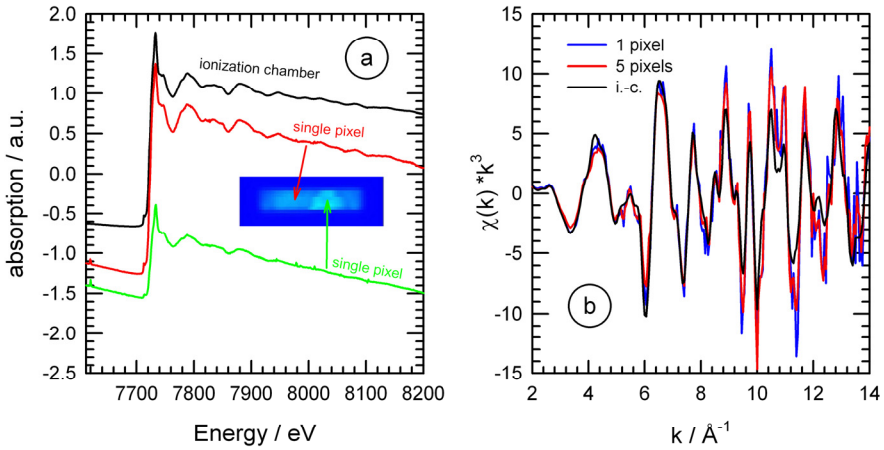

Fig. 2: (a) Raw XAFS data for an inhomogeneous Co_3O_4 powder sample with an intensity map. (b) $\chi(k)*k^3$ data extracted from a single pixel (—) and 5 neighboring pixels (——) in comparison to the ionization chamber data (—).

An example of a Co_3O_4 powder sample dispersed on a sticky tape is given in Fig. 2(a). The inhomogeneous intensity distribution on the 2D-detector is directly reflected in a variation of the edge jump on two selected positions (see the arrows in the insert of Fig. 2(a)). As depicted in Fig. 2(b), the EXAFS oscillations measured using the ionization chamber appear to have a substantially smaller amplitude compared to the data of selected single pixels especially at larger k-values. These observations clearly prove that it is required to take these sample inhomogeneities into account for a reliable data analysis, i.e. to obtain physical meaningful coordination numbers.

In conclusion, from the quality of the EXAFS data obtained with the Pilatus 100 K area detector, it can be deduced that laterally resolved EXAFS spectra of inhomogeneous samples are feasible on a length scale of the pixel size of the detector, i.e. about 200 µm in the present case, which make this setup promising for future experiments at DELTA beamlines 8 and 10. Due to the large radiation fan provided by the superconducting asymmetric wiggler (SAW), the atomic structure of larger samples with inhomogeneities may be mapped using X-ray absorption spectroscopy. Furthermore, the huge amount of collected X-ray absorption spectra allows the application of more sophisticated data analysis techniques [5].

References

[1] F. Bridges, G.G. Li and X. Wang, Nucl. Instrum. Meth. A 320 (1992) 548

[2] C.G. Schroer and J.-D. Grunwaldt, In: In-situ characterization of heterogeneous catalysts. Eds.: J.A. Rodriguez, J.C. Hanson, and P.J. Chupas. John Wiley & Sons (2013) pp. 49.

[3] H. Tanida, H. Yamashige, Y. Orikasa, M. Oishi, Y. Takanashi, T. Fujimoto, K. Sato, D. Takamatsu, H. Murayama, H. Arai H, et. al., J. Synchrotron Rad. 18 (2011) 919

[4] P. Kraft, A. Bergamaschi, C. Broennimann, R. Dinapoli, E.F. Eikenberry, B. Henrich, I. Johnson, A. Mozzanica, C.M. Schlepütz, P.R. Willmott and B. Schmitt, J. Synchrotron Rad. 16 (2009) 368

[5] R. Bögel, Bachelor thesis, Wuppertal University (2015)

Development of a Scanning Reflection X-ray Microscope (SRXM)

A. Schümmer[1], M. Gilbert[1], C. Jansing[1], H.-Ch. Mertins[1],
R. Adam[2], C. M. Schneider[2], L. Juschkin[3]

[1] University of Applied Sciences, Münster Stegerwaldstraße 39, 48565 Steinfurt, Germany
[2] Forschungszentrum Jülich, Wilhelm-Johnen-Straße, 52428 Jülich, Germany
[3] Rhein Westfälische Technische Hochschule Aachen, Templergraben 55, 52062 Aachen, Germany

We present a new project and propose a design of a scanning reflection x-ray microscope (SRXM). This operation in reflection mode will allow the study of surfaces and interfaces even of thick samples. It also will enable imaging of magnetic domains in buried layers exploiting magneto-optical reflection spectroscopy like XMLD and XMCD. Working at the DELTA beamline 12 in the extreme ultraviolet (EUV) regime, i.e. the range of 3p absorption edges of 3d transition metals will provide for sufficient intensities of reflected light which is not achievable at the relevant 2p edges [1, 2].

Introduction

Modern x-ray microscopes can be divided into two categories: full-field transmission x-ray microscopes (TXM) and scanning transmission x-ray microscopes (STXM). Both microscopes use Fresnel zone plates as high resolution optics in the soft x-ray region. First experiments with full-field x-ray microscope in reflective mode showed the possibility to design a microscope based on the reflection principle [3].

TXM

The TXM is a full-field imaging technique. A condenser optic (condenser lens, tube, zone plate or Kirkpatrick-Baez mirror) illuminates the sample and a high-resolution zone plate images the sample on a spatial detector [4]. For a higher image contrast all higher orders (≥2) are blocked by a pinhole (order selecting aperture). Additionally a central stop blocks the zero order.

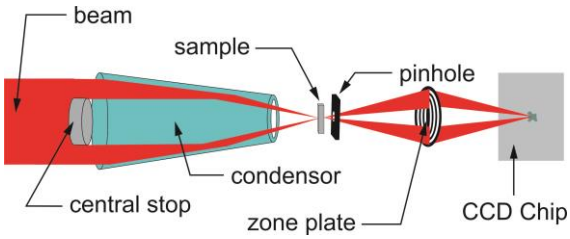

Fig. 1 Sample setup of a transmission x-ray microscope (TXM)

STXM

The STXM images the sample by scanning. The beam is focused on the sample by a high resolution zone plate and the transmitted radiation is monitored, from which a two dimensional picture is reconstructed. The advantage of STXM over TXM is the smaller photon flux hitting the target [4]. In particular, biological applications benefit from low doses, which avoid destruction of the specimen. The disadvantages of STXM compared to TXM are the slower sampling rate and the higher influences of vibrations, source drifts and positioning errors.

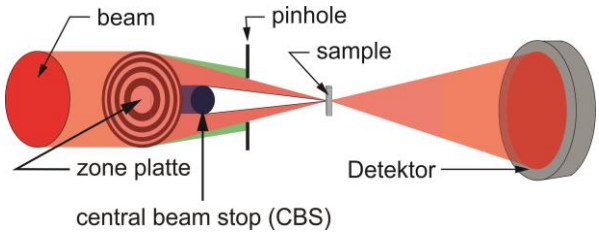

Fig. 2 Sample setup of a scanning transmission x-ray microscope (STXM)

Scanning Reflection X-ray Microscopy (SRXM)

Setup

The first element of the projected SRXM is a high resolution Fresnel zone plate that focuses the beam to a small spot of 100 nm diameter. A central beam stop (CBS) is placed between the zone plate and the sample to block zero order radiation. The higher orders are blocked by an order selecting aperture (OSA), like it is done in STXM and TXM. In contrast to STXM the sample is illuminated not perpendicular to the surface, but at grazing incidence near 20-45°. This angle allows magneto-optical reflection spectroscopy as T-MOKE, L-MOKE or XMLD. The contrast depends on the orientation between the light's linear polarization vector and the magnetization direction. This enables the detection of magnetic domains of ferromagnetic and anti-ferromagnetic materials. Using EUV synchrotron radiation near the 3p absorption edges of 3d transition metals about 50eV – 70eV, results in sufficient reflected intensities, which are about 2 orders of magnitude larger than those at the respective 2p edges due to the higher reflectivity in the EUV regime. Additionally at incidence angles close to Brewster's angle highest contrast is achieved for magneto-optical effects.

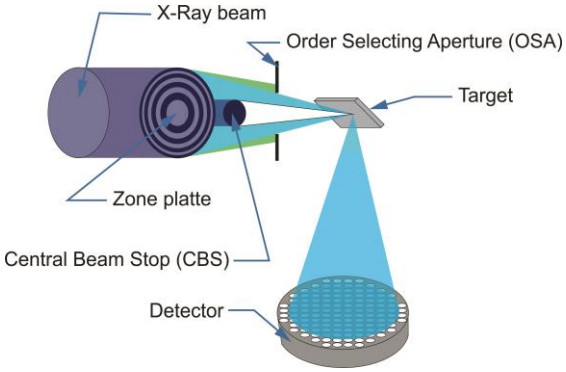

Fig. 3 Setup of the scanning reflection x-ray microscope

Challenges

Despite the relatively high reflectance of metallic samples in the EUV a high photon flux is needed. Therefore, the scanning method has been selected since a smaller photon flux is required compared to the full field imaging. High resolution zone plates with a spatial resolution near 100 nm result in short focal length of about 1 mm in the EUV region. This limits the mechanical operation range of samples and detectors. As a first step the central beam stop will be integrated into the zone plate structure. The depth of focus limits the angles, so that grazing incidence angles smaller than 20° cannot be realized. Aberrations due to the grazing incidence angles change the shape and the size of the focus spot on the sample.

Outlook

The proposed project will be realized at the DELTA beam line 12 within the next year. After successful characterization of the beam characteristics in the past, adopted zone plates will be designed, fabricated and tested at beamline 12.

[1] H.-C. Mertins, S. Valencia, A. Gaupp, W. Gudat, P.M. Oppeneer; C.M. Schneider „Magneto-optical polarisation spectroscopy with soft X-rays“ Appl. Phys. A80,1011-1020 (2005)

[2] M. F. Tesch, M. C. Gilbert, H.-Ch. Mertins, D. E. Bürgler, U. Berges, and C. M. Schneider "X-ray magneto-optical polarization spectroscopy: an analysis from the visible region to the x-ray regime"., Applied Optics 52, 4294-4310 doi: 10.1364/AO.52.004294 (2013)

[3] Greg Denbeaux, Peter Fischer, Farhad Salmassi, Kathleen Dunn, James Evertsen „Reflection Mode Imaging with High Resolution X-ray Microscopy“ Proc. 8th Int.Conf. X-ray Microscopy IPAP Conf. Series 7 pp.375-376 (2006)

[4] Settimio Mobilio, Federico Boscherini, Carlo Menengihini „Synchrotron Radiation“ Springer ISBN 978-3-642-55314-1 (2015)

Beamline 10: TRXRD probes the mechanisms of electromechanical couplings in $Na_{0.5}Bi_{0.5}TiO_3$ single crystal

J. Bieker[1], M.Paulus[1], M. Tolan[1], U. Pietsch[2], S. Gorfman[2]

[1]Department of Physics, TU Dortmund University, Dortmund, Germany
[2] Department of Physics, University of Siegen, Siegen, Germany

In many recent studies the electromechanical couplings in perovskite-based ferroelectrics has been investigated, with the general aim to understand the connection between piezoelectricity and ferroelectricity [1]. Besides that, there is also the interest to design environmentally friendly replacements to the currently dominating lead-based $PbZr_{1-x}Ti_xO_3$ (PZT) [2]. Quite promising candidates are $Na_{0.5}Bi_{0.5}TiO_3$ - $BaTiO_3$ (NBT-BT) solid solutions [3,4].

The focus of our studies is to investigate the structural mechanisms of converse piezoelectricity in multi-domain single crystal of $Na_{0.5}Bi_{0.5}TiO_3$ (NBT) - the end-member of NBT-BT.Therefore we use a custom built, FPGA-based data-acquisition system (DAQ) for stroboscopic time-resolved X-Ray diffraction (TRXRD), developed by the Electronic Lab of the University of Siegen [5]. This system has been successfully implemented at Beamline 10 at the Delta synchrotron facility, allowing the synchronization of detector signals with the timing of a periodically applied electric field. In figure 1 the used experimental setup is shown schematically.

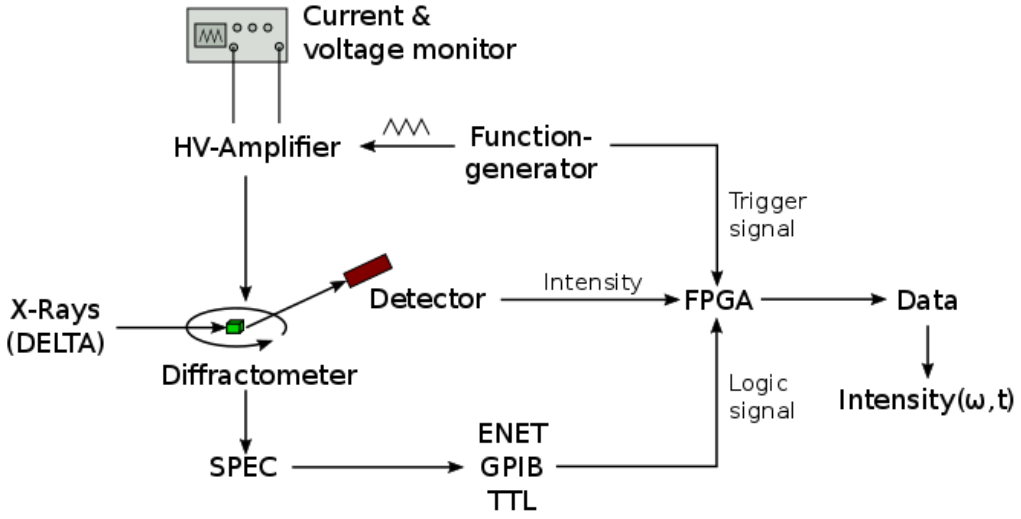

figure1: sceme of the custom-built, stroboscopic based experimental setup for TRXRD.

We applied a periodically, triangular shaped voltage of ±1 kV with a frequency of 100 Hz to the single crystal and used a X-ray beam with an energy of 13.0 keV to measure several $\{00l\}_{pc}$Bragg rocking curves.
Further on we analyzed the dynamic of the corresponding average *c*-lattice parameter as a function of time and electric field.

Representing the behavior of all $\{00l\}_{pc}$Bragg rocking curves - one can see in figure 2 our observation of a broadening of the $\{006\}_{pc}$rocking curve for a negative applied voltage, but only a shift at positive voltage. Looking at the center of mass ‹ω› of the rocking curve - shown in figure 3 - one can see, that the average piezoelectric response of the single crystal increases at negative applied voltage. Therefore it is important to find out, what leads to the broadening of the rocking curves.

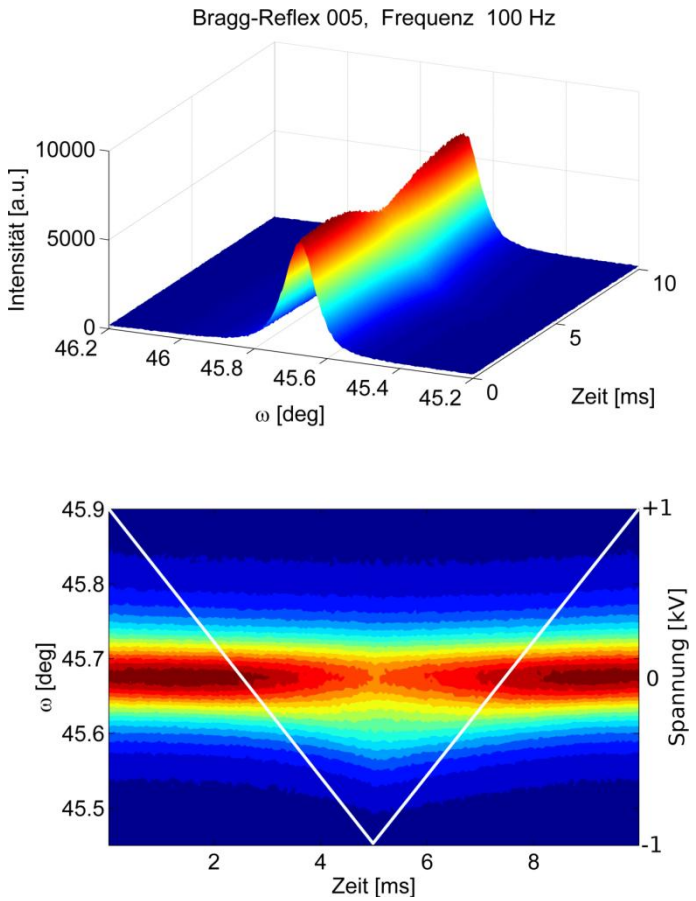

Figure 2: $\{006\}_{pc}$ rocking curve in dependence of time within a period of the triangular shaped voltage.
On the top: 3D plot.
At the bottom: top view and applied voltage.

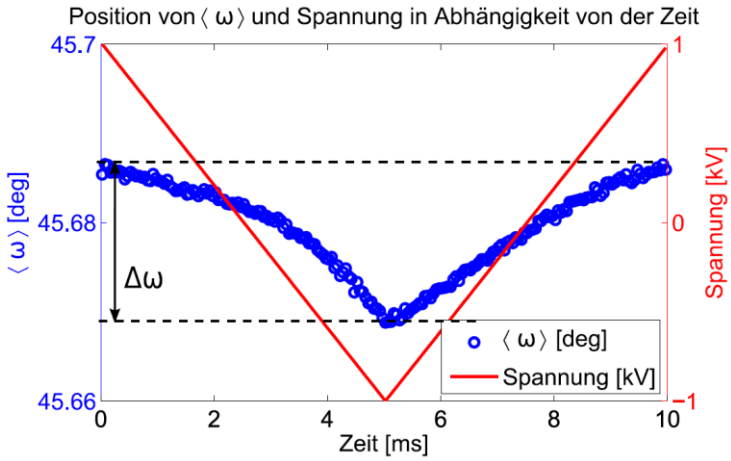

Figure 3: the position of the center of mass ‹ω› in dependence of the time within the period of the applied electric field is shown in blue. The applied voltage is drawn in red.

We inspected the fine structure of the diffraction profiles and discovered that the application of the negative electric voltage separates the probed $Na_{0.5}Bi_{0.5}TiO_3$ volume into two volume fractions with different electromechanical properties.

There are several possible mechanisms leading to this separation. For example extrinsic mechanisms, i.e. mechanisms that change the domain distribution – like domain wall motions, or intrinsic mechanisms, i.e. mechanisms that occur within a single domain – like polarization rotation and extension.

From the in-depth-analysis of the rocking curves we concluded, that the intrinsic mechanisms are most probably the root of the asymmetric behavior. We suggest that the polarization rotation of monoclinic M_A-domains leads to an increase of strain within the crystal lattice. Simultaneously rhombohedral domains have a lower piezoelectric response, because their symmetry only allows polarization extension. This would explain the observed rocking curve splitting.

However, this observations and conclusions merit further investigations.

References

[1] Damjanovic, Dragan: Comments on Origins of Enhanced Piezoelectric Properties in Ferroelectrics. In: *IEEE Transactions on Ultrasonics, Ferroelectrics, and Frequency Control* 56 (2009), August, Nr. 8, 1574–1585.

[2] Saito, Yasuyoshi ; Takao, Hisaaki ; Tani, Toshihiko ; Nonoyama, Tatsuhiko; Takatori, Kazumasa ; Homma, Takahiko ; Nagaya, Toshiatsu; Nakamura, Masaya: Lead-free piezoceramics. In: *Nature* 432 (2004), November, Nr. 7013, 84–87.

[3] Keeble, Dean S.; Barney, Emma R.; Keen, David A.; Tucker, Matthew G.; Kreisel, Jens; Thomas, Pam A.: Bifurcated Polarization Rotation in Bismuth-Based Piezoelectrics. In: *Advanced Functional Materials* 23 (2013), January, Nr. 2, 185–190.

[4] Roleder, K.; Franke, I.; Glazer, A.M.; Thomas, P.A.; Miga, S.; Suchanicz, J. The piezoelectric effect in $Na_{0.5}Bi_{0.5}TiO_3$ ceramics. In: *J. Phys. Condens. Matter* **2002**, 14, 5399–5406.

[5] Gorfman, S., Schmidt, O., Ziolkowski, M., von Kodzierowski, M., Pietsch, U. Time-resolved X-ray diffraction studies of the piezoelectric crystal response to a fast change of an applied electric field. J Appl Phys, 108, 064911, (2010)

Commissioning of a von-Hamos spectrometer for x-ray emission and x-ray Raman scattering studies

Christian Sternemann[1], Manuel Harder[1,2], Thomas Büning[1], Christian Bressler[3,4], Holger Göhring[1], Christopher Weis[1], Wojciech Gawelda[3], Andreas Galler[3], Metin Tolan[1]

[1] Physik / DELTA, Technische Universität Dortmund, D-44221 Dortmund, Germany; [2] Deutsches Elektronen-Synchrotron DESY, D-22607 Hamburg, Germany; [3] European XFEL, D-22607 Hamburg, Germany; [4] Centre for Ultrafast Imaging, D-22761 Hamburg, Germany.

A von-Hamos spectrometer for time-resolved x-ray emission and x-ray Raman scattering experiments on femto- to millisecond timescales will be installed at the FXE endstation of the European free electron laser (XFEL). This spectrometer was tested and characterized at beamline BL9 of the synchrotron radiation source DELTA. The spectrometer itself was equipped with 8 Si (220) cylindrically bent analyzer crystals and the analyzed radiation was detected using a Pilatus 100-K area detector. The analyzer crystals were aligned such that 8 separate spectra could be measured simultaneously by the area detector. The energy scale of each spectrum was calibrated employing elastic scattering from a kapton foil. Spectra of the cobalt K_α and iron K_β fluorescence lines were measured showing the general ability of the setup to study transition metal complexes. Moreover, momentum transfer dependent measurements of the dynamic structure factor of Be metal were performed (see figure 1 left) and the capability of the setup to measure absorption edges of low Z elements bulk sensitively by x-ray Raman scattering was demonstrated for the beryllium (see figure 1 right) and C K-edge. During this beamtime the von-Hamos spectrometer was successfully tested and characterized. It is currently used for time-resolved x-ray emission experiments at beamline P01 of PETRAIII before it will be transferred finally to XFEL.

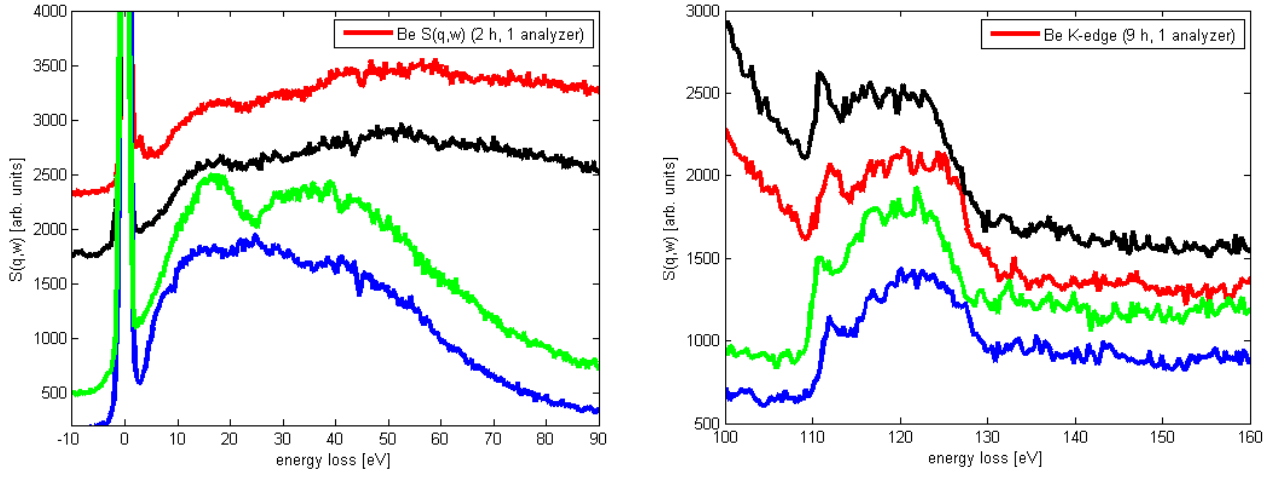

Figure 1: Momentum transfer dependence of (left) the dynamic structure factor and (right) the K-edge x-ray Raman spectra of beryllium single crystal measured with the von-Hamos spectrometer.

This work was carried out within FSP-302 of the BMBF. MH and TB thank the BMBF (05K13PE2) for financial support. TB acknowledges funding via MERCUR (AN-2014-0036) and HG via SFB (TR160C6). CB, AG, WG thank for financial support by the German research foundation (DFG) via SFB925 (TPA4), and by the Centre of Ultrafast Imaging.

Soft X-ray Spectroscopy

Magnetic linear dichroism in the angular distribution of photoelectrons

M. Gehlmann[1,2], S. Döring[1,2], M. Eschbach[1], E. Mlynczak[1], P. Gospodaric[1], S. Cramm[1], L. Plucinski[1,2], C.M. Schneider[1,2]

[1] Peter Grünberg Institut, PGI-6, Forschungszentrum Jülich GmbH, D-52425 Jülich, Germany
[2] Experimentalphysik - Universität Duisburg-Essen, Lotharstr. 1, 47057 Duisburg

(November 2015)

Magnetism has its origin in the electronic structure of metals. Electronic energy levels are shifted depending on the spin of the electrons and this results in spin-polarized electronic bands. Therefore, angle resolved photoemission experiments that probe the electronic band structure are in principle well suited to investigate magnetism on this microscopic scale.

Of course, the experiment must be modified to show spin-contrast that can be related to magnetism. One way to achieved this contrast is to measure the spin of the emitted photoelectrons directly with an appropriate detector [1]. Generally, those detectors are not very efficient and this limits the range of applications for spin-resolved photoemission experiments.

A different way to achieve magnetic contrast is using dichroic effects. The cross-section that is connected to the photoemission intensity is a function of the polarization of the incoming radiation and the magnetization of the sample that emits the photoelectrons. Dipole selection rules are responsible for this so-called magnetic dichroism. The photoemission intensity changes when either the magnetization of the sample or the polarization direction of the light is reversed. In the experiment, conventional spin-integrated photoemission spectra are recorded at either different magnetization or polarization directions and the difference between those spectra represents the dichroic effect.

By measuring angle-resolved photoemission spectra (ARPES) we investigate the angular distribution of the magnetic linear dichroism (MLD). Because the beamline BL5 provides exclusively horizontally linear polarized light we have to reverse the magnetization of the sample in order to record the contrast.

As a model system we chose thin ferromagnetic Co films on Cu(001). This system is well-understood in principle, but new methods may result in new surprises: We found that the strength of the MLD effect in the valence band depends strongly on the photon energy. At the maximum around $h\nu = 55$ eV the effect is ten times stronger than at lower photon energies which are used for conventional ARPES experiments with lab sources. The contrast also decreases at higher photon energies.

Figure 1 shows a set of angle resolved MLD spectra at this special energy. The spectra were recorded around normal emission which is the gamma point in k-space of this system. Blue areas represent parts of the spectrum that are stronger for one magnetization (positive difference) while the red areas show the parts with lower intensity for this magnetization direction (negative difference). The single panels show different cuts through the 3D data slab that we recorded.

Theoretical studies are conducted at the moment in order to gain a better understanding. It is not trivial to connect the angular distribution of the MLD to the electronic band structure. The MLD contrast follows only some bands and is not equally strong for different points of the band structure.

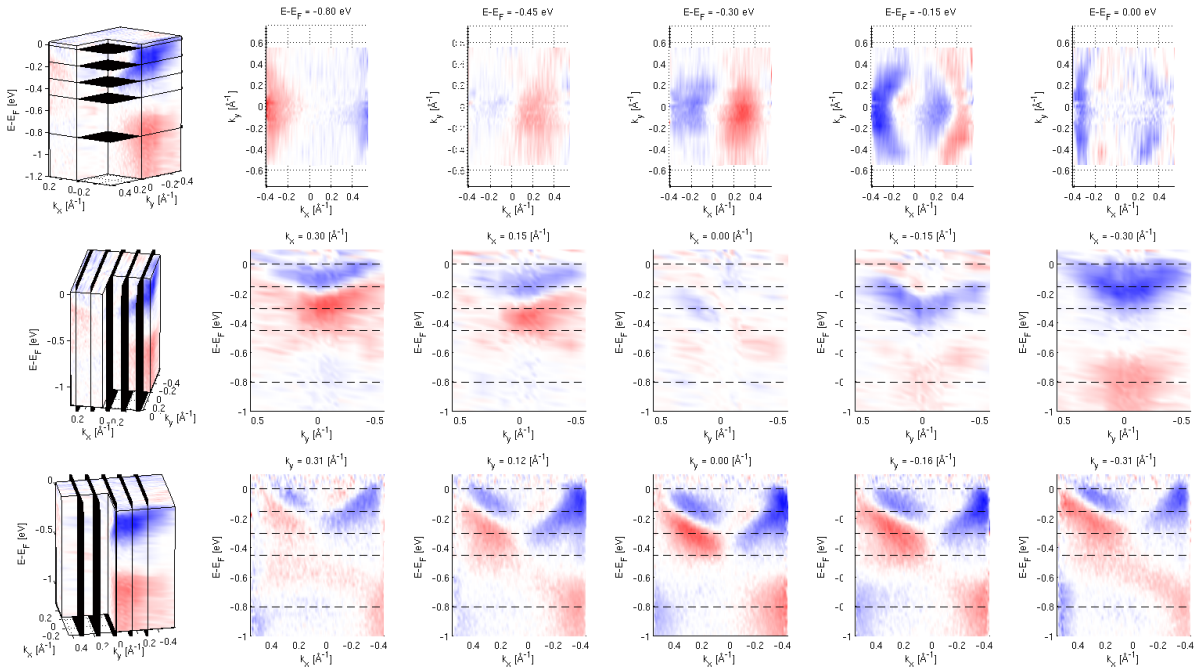

Figure 1: The magnetic linear dichroism in the valence band of a thin Co film on Cu(001) shows a strong angular dependence.

One goal of those experiments at BL5 is the connection to the short-pulse project. The ARPES detector can be gated in order to achieve time-resolved photoemission experiments excited by a combination of short laser and CHG pulses [2]. The repetition rate of those pulses is rather low compared to the conventional synchrotron light and, therefore, the overall intensity is not sufficient to conduct spin-resolved photoemission experiments. But a better understanding of the MLD effect will allow us to use this window into magnetization dynamics at a microscopic, and therefore very basic, level.

[1] L. Plucinski, A. Oelsner, F. Matthes und C. Schneider, *A hemispherical photoelectron spectrometer with 2-dimensional delay-line detector and integrated spin-polarization analysis*, Journal of Electron Spectroscopy and Related Phenomena **181**, 215 (2010). [2] S. Khan, F. Bahnsen, S. Cramm, S. Döring, J. Grewe, M. Höner, H. Huck, M. Huck, R. Molo, L. Plucinski, A. Schick, C. M. Schneider und P. Ungelenk,*Generation of Ultrashort and Coherent Synchrotron Radiation Pulses at DELTA*, Synchrotron Radiation News **26**, 25 (2013).

Beamline 5: Quasi 2D electronic states with high spin-polarization in centrosymmetric MoS_2 bulk crystals

Mathias Gehlmann[1], Gustav Bihlmayer[2], Irene Aguilera[2], Ewa Mlynczak[1,2], Markus Eschbach[1], Sven Döring[1], Pika Gospodaric[1], Stefan Cramm[1], Beata Kardynal[4], Lukasz Plucinski[1], Stefan Blügel[2], Claus M. Schneider[1]

[1]PGI-6, Forschungszentrum Jülich GmbH, D-52425 Jülich, Germany
[2]PGI-1/IAS-1, Forschungszentrum Jülich GmbH and JARA, D-52425 Jülich, Germany
[3]Faculty of Physics and Applied Computer Science, AGH University of Science and Technology, al. Mickiewicza 30, 30-059 Kraków, Poland
[4]PGI-9, Forschungszentrum Jülich GmbH, D-52425 Jülich, Germany

Two-dimensional materials are considered excellent candidates for next-generation electronic devices that could overcome the restrictions of classical, Si-based electronics. Apart from the possibility of a reduced size compared to state of the art transistor devices, thinning down materials like molybdenum disulphide (MoS_2) gives rise to new phenomena that might allow entirely different approaches for applications such as spintronics, valleytronics, solar cells, or optical sensors [1].

Time reversal symmetry dictates that electronic states in nonmagnetic, centrosymmetric crystals cannot be spin-polarized. However, a recent publication by Zhang and Liu et al. [2] introduces a "hidden spin-polarization" resulting from specific site asymmetries instead of the crystal space group. MoS_2 is a model material which exhibits such effects. It is a layered crystal that consists of two-dimensional S-Mo-S atomic trilayers with broken inversion symmetry within the plane. In A-B stacking these trilayers recover inversion symmetry and therefore the bulk shows a centrosymmetric space group. One of the most remarkable features of MoS_2 is the strong spin-splitting of the valence band at the $\overline{\mathrm{K}}$ point. While this splitting is well known to be highly spin-polarized in isolated monolayers it is a commonly accepted opinion that in the bulk the polarization is forbidden by the crystal symmetry.

In a recent study we performed angle resolved photoemission spectroscopy (ARPES) on bulk MoS_2 [3]. The extreme surface sensitivity and the momentum-resolution capabilities of our method in combination with a SPLEED spin-detector allow the direct observation of the hidden spin-polarization in this material.

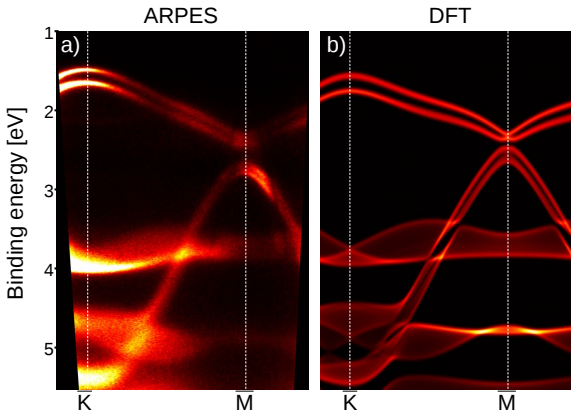

Figure 1: a) ARPES spectrum along $\overline{\mathrm{KM}}$ direction measured with $h\nu = 21.2$ eV using He-VUV source, b) the corresponding calculation of bulk projected band structure for MoS_2. In the calculated maps bright areas indicate sharp bands with little out-of-plane dispersion, darker bands a broader projection. In b) the Fermi energy is shifted for comparison with a).

Figure 1 depicts a comparison of the measured ARPES data with the calculated bulk projected band structure of MoS_2 along the $\overline{\mathrm{KM}}$ direction. Although our experiment is extremely surface sensitive we find a very good agreement of the ARPES spectra with the density functional theory (DFT) calculation which is not surprising for this class of materials since the layers do not give rise to dangling bonds in the (0001) direction and show almost no surface relaxation. The ARPES and the bulk projection both reveal two very sharp subbands of the topmost valence band at the $\overline{\mathrm{K}}$ point. In the spectrum the splitting seems obvious but since it only cuts a 2D plane out of the 3D Brillouin Zone (BZ) the observation of the two sharp bands alone does not prove that they remain split along the entire out-of-plane KH direction. However, in photoemission the out-of-plane momentum of the photoelectron can be scanned by varying the photon energy. Figures 2 a)-c) show the ARPES spectra along the high symmetry direction $\overline{\mathrm{KM}}$ for three different photon energies. All three spectra represent a part of the 3D-BZ with a different out-of-plane photoelectron momentum $k_\perp$. The values for $k_\perp$ were estimated using

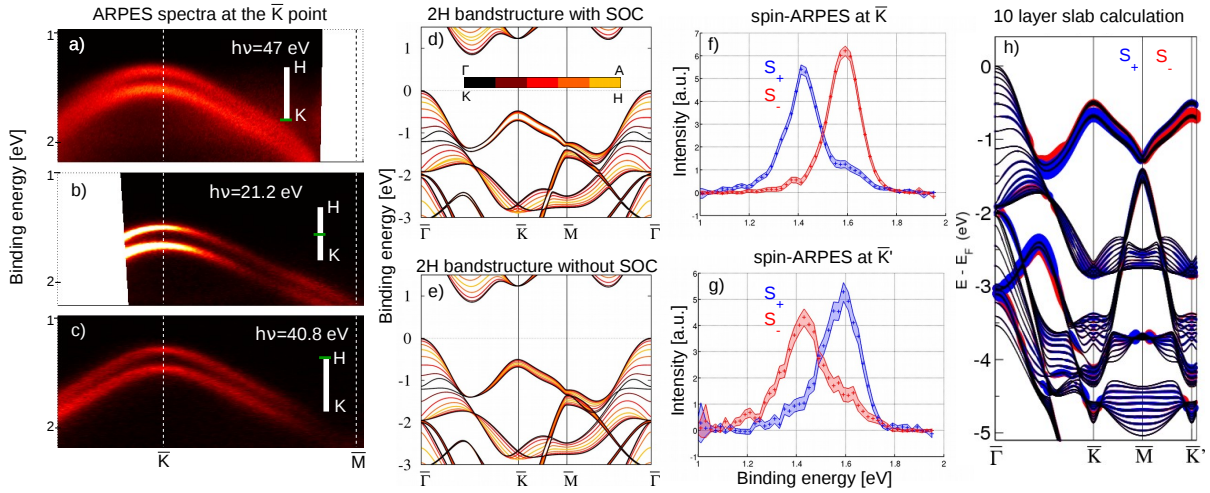

Figure 2: a-c) ARPES spectra of the VBM at the $\overline{\text{K}}$ point taken at different photon energies to map the $k_\perp$ dependence, d-e) DFT calculation of the bulk band structure of MoS_2 with and without spin orbit coupling, color coded for different values of $k_\perp$, f-g) spin-ARPES spectra of the valence band at the $\overline{\text{K}}$/$\overline{\text{K}}$' point. These spectra are corrected for the spin-detector efficiency and the non-zero emission angle. The filled area represents the statistical error, h) 10-layer slab calculation of MoS_2 band structure. The size of the red and blue circles represent the out-of-plane spin-polarization in the topmost monolayer.

the free electron final state model and assuming an inner potential of 10 eV. There is almost no change in the size of the splitting measured with different photon energies. This lack of out-of-plane dispersion in ARPES and DFT shows that even in the bulk these states are almost completely confined within two dimensions and are therefore similar to those in the freestanding monolayers.

Figures 2 f) and g) show the spin-ARPES spectra taken at the $\overline{\text{K}}$ point and the $\overline{\text{K}}$' point on the opposite side of the BZ. One can immediately see that these states are highly spin-polarized and that the polarization reverses at the $\overline{\text{K}}$' point. For the polarization we find $\approx 65\%$ at $\overline{\text{K}}$ and $\approx 50\%$ at $\overline{\text{K}}$'. The directly observed degree of polarization is reduced compared to the actual polarization of the electronic state by a mixed contribution of A- and B-oriented layers to the spectrum. There are two major reasons for this intermixing. On one hand the surface is not purely A- or B-terminated. This explains the different polarization found at $\overline{\text{K}}$ and $\overline{\text{K}}$' since the position of the beamspot is marginally shifted. On the other hand our probing depth is slightly higher than the thickness of a single monolayer. With a model calculation we estimated that the valence band almost fully spin-polarized at the at $\overline{\text{K}}$ point.

Using a combination of ARPES and DFT calculations we were able to show that the distinct valleys in the electronic band structure of bulk MoS_2 are quasi two-dimensional and highly spin-polarized despite its three-dimensional, centrosymmetric space group. Our findings represent the first observation of this recently introduced type of hidden spin-polarization in MoS_2. This class of materials could broaden the playground for novel spintronic applications as long as the compensated nature of the spin-polarization, both in real and reciprocal space, is taken into account.

References

[1] Geim, A. K. & Grigorieva, I. V. Van der Waals heterostructures. *Nature* **499**, 419–425 (2013).

[2] Zhang, X., Liu, Q., Luo, J.-W., Freeman, A. J. & Zunger, A. Hidden spin polarization in inversion-symmetric bulk crystals. *Nat Phys* **10**, 381–393 (2014).

[3] Gehlmann, M. *et al.* Quasi 2D electronic states with high spin-polarization in centrosymmetric MoS_2 bulk crystals. *arXiv:1510.04101* (2015).

XPS/XPD study of the topological insulator BiTe

P. Espeter[1,2,*], S. Döring[2,3], M. Eschbach[3], M. Gehlmann[2,3], C. Keutner[1,2], C. Kohlmann[1,2], D. Krull[1,2], L. Plucinski[3], U. Berges[1,2], C.M. Schneider[3], C. Westphal[1,2]

[1] Experimentelle Physik I - Technische Universität Dortmund, Otto-Hahn-Str. 4, D-44227 Dortmund
[2] DELTA - Technische Universität Dortmund, Maria-Goeppert-Mayer-Str. 2, D-44227 Dortmund
[3] Forschungszentrum Jülich, D-52425 Jülich
[*] corresponding author: philipp.espeter@tu-dortmund.de

Three-dimensional topological insulators are considered to be a new state of quantum matter. They show an electronic bulk band structure with an insulating gap while they also possess metallic and highly spin-polarized surface states. In recent years, Bi_2Te_3 has become kind of a textbook example for strong topological insulators and has been the focus of many experimental and theoretical studies [1]. Other stoichiometric stable phases in the Bi-Te alloy family raised only little interest, even though they promise exciting properties. The Bi_1Te_1 alloy, for example, ist supposed to be a so-called weak topological insulator due to changes in the crystal structure in comparison to Bi_2Te_3. Since the most interesting effects occur at the surface of topological insulators, a precise knowledge of the surface morphology and structure is crucial to understand its electronic structure, especially the spin-dependent surface band structure.
In this study, we demonstrate a surface structure investigation of Bi_1Te_1 by means of photoelectron spectroscopy and diffraction.
The sample is illuminated with monochromatic X-rays, provided by the U55 PGM Beamline 11 at

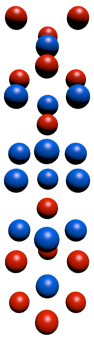

Figure 1: Lattice structure of bulk Bi_1Te_1, red spheres correspond to Tellur atoms, blue spheres correspond to Bismuth atoms.

DELTA. The photoelectron spectra are recorded as a function of azimuthal and polar angle [2]. The

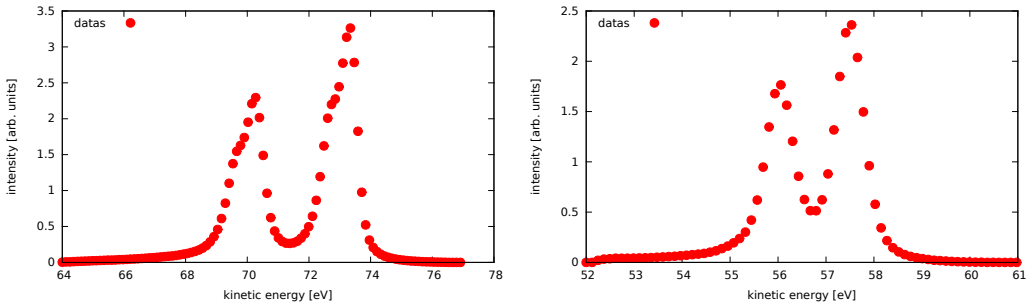

Figure 2: High-resolution XPS spectra of Bismuth-5d- (left) and Tellur-4d-signals (right). The Bismuth-5d-spectrum shows a double-peak structure, indicating two different chemical environments for the Bi atoms.

observed anisotropic modulations recorded in the XPD pattern provide information about the local environment of the emitting atoms.
The analysis is performed by three iterating steps, first generating a structure model, second simulation of the XPD pattern by using the MSPHD programm and third comparison with the experimental data [3]. As the degree of accordance the reliability-factor (R-factor) is used, where a R-factor of 0 means exact accordance and a R-factor of 2 means exact anticorrelation. A sufficient accordance between the experimental and simulated data is reached if the R-factor is less than 0.1 [4].
Here we present the results of primary simulations of Bi_1Te_1. They are based on the known unit

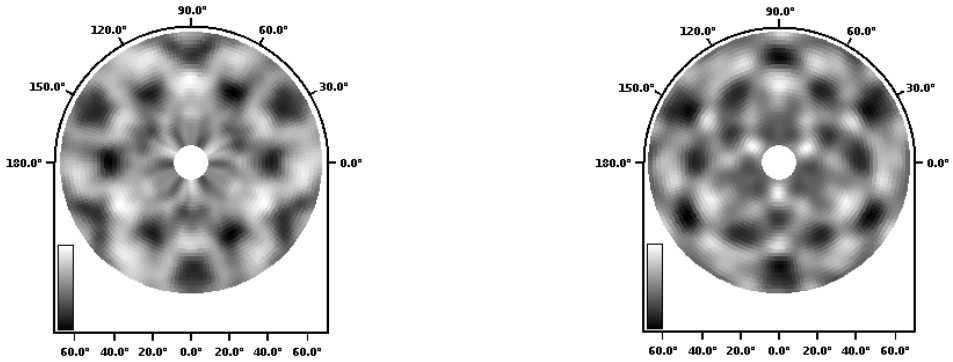

Figure 3: Measured XPD pattern of BiTe (left) and best simulated XPD pattern (right).

cell of bulk Bi_1Te_1 and scanning tunneling microsopy results, which indicate a terraced surface with alternating Tellur and Bismuth termination.
First simulations with only Tellur or only Bismuth terminated surfaces yielded R-factors in the range between $R = 0.4$ and $R = 0.6$. Slight modulations of the atomic arrangement, i.e. building trimers in the topmost layer or shifting of layer distances, did not yield a significant improvement of the R-factor. Therefore, neccessary software extensions were realized for parallel simulation of many different terminations. Furthermore, a subroutine was implemented to weight the emitting atoms. Simulations of the extended software resulted in a enhanced R-factor of about $R = 0.16$. Due to the complex structure and post-treatment of the simulated data by subroutines more computing time is mandatory to achieve further improvements of the R-factor.

References

[1] Y. Xia, D. Qian, D. Hsieh, L. Wray, A. Pal, H. Lin, A. Bansil, D. Grauer, Y. Hor, R. Cava and M. Hasan, *Observation of a large-gap topological-insulator class with a single dirac cone on the surface*, Nature Physics **5**, 398 (2009).

[2] C. Westphal, *The study of the local atomic structure by means of X-ray photoelectron diffraction*, Surface Science Reports **50**, 1 (2003).

[3] R. Gunnella, F. Solal, D. Sebilleau and C. Natoli, *MSPHD: A full multiple scattering code for low energy photoelectron diffraction*, Computer Physics Communications **132**, 251 (2000).

[4] D. P. Woodruff and A. M. Bradshaw, *Adsorbate structure determination on surfaces using photoelectron diffraction*, Reports on Progress in Physics **57**, 1029 (1994).

Tetraphenylporphyrin layers on Au(111)

P. Roese[1,2,*], P. Espeter[1,2], C. Keutner[1,2], D. Krull[1,2], U. Berges[1,2], C. Westphal[1,2]

[1] Experimentelle Physik I - Technische Universität Dortmund, Otto-Hahn-Str. 4a, D-44221 Dortmund
[2] DELTA - Technische Universität Dortmund, Maria-Goeppert-Mayer-Str. 2, D-44221 Dortmund
[*] corresponding author: peter.roese@tu-dortmund.de

Porphyrins are important building blocks of life. Heme b is such an example whose function is to transport oxygen through the body [1]. It is a metalloporphyrine complex with an iron ion at the center. Another example is the magnesium containing chlorophyll which is relevant for the photosynthesis in plants [2]. By bonding different external groups at the meso positions and changing the metal ions in the center of the molecule, many different variants of porphyrins with differing chemical and electronic properties can be synthesized. This is the reason why the interest in using porphyrins as technical devices increased in recent years. Applications such as organic solar cells [3], organic LED's [4] or the usage of porphyrins as photosensibilisator in cancer treatment [5] utilize the strong absorption properties of porphyrins in the visible spectrum.

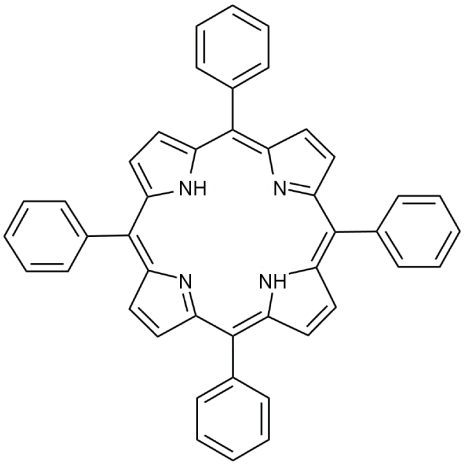

Figure 1: Structure of meso-Tetraphenylporphrin (2HTPP).

In this work, metalfree meso-tetraphenylporphyrin (2HTPP) was studied on an Au(111) surface using x-ray photoelectron spectroscopy (XPS). The experiments were performed at the U55 beamline 11 at DELTA. The structure of this molecule is shown in Figure 1. The herringbone reconstruction of the Au(111) surface [6] was covered by multiple layers of 2HTPP by using molecular beam epitaxy. Therefor, a new Knudsen cell was mounted at the experimental station in order to evaporate the molecules at 400 °C. The question whether 2HTPP forms bonds with the substrate is of particular interest. Therefor, appropriate parameters for the preparation of porphyrine monolayers by multilayer desorption have to be found.
An indicator for such a molecule-substrate interaction are the four nitrogen atoms in the center of 2HTPP. Without a bonding of the molecule to the substrate, the four nitrogen atoms are present in two different bonding states. The iminic nitrogen (=N-) bonds solely to carbon, while pyrrolic nitrogen (-NH-) in addition bonds to hydrogen. This hydrogen is lost, if there

is a bonding to a substrate or to a metal ion in the center (called metallation). In this case all four nitrogen atoms are present in the same bonding state. This leads to a single nitrogen peak in the nitrogen XPS spectrum instead of two separated peaks for the iminic and pyrrolic nitrogen.
Figure 2 shows the high resolution XPS spectrum of N 1s of 2HTPP on Au(111) for a polar angle of $\Theta = 60°$.

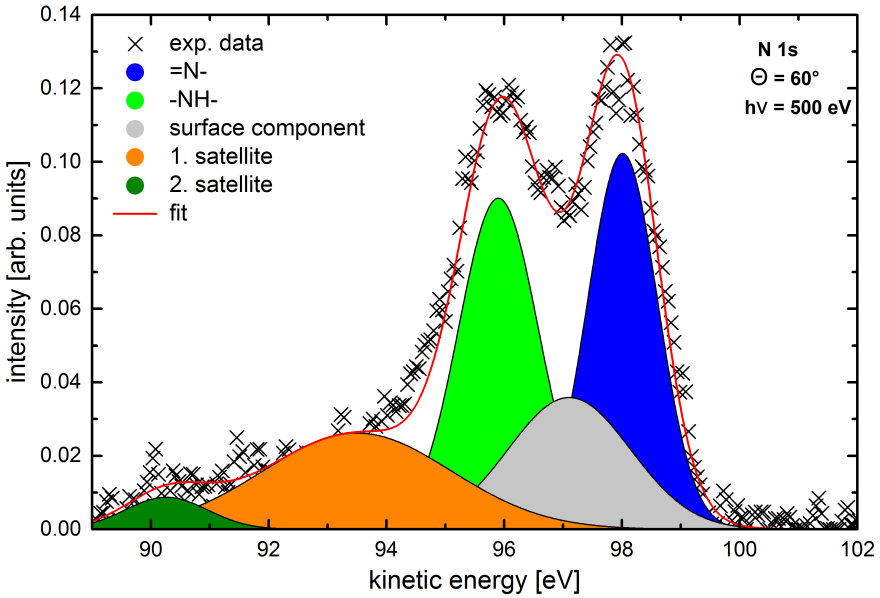

Figure 2: N 1s XPS spectrum of 2HTPP using a photon energy of hν = 500 eV of a polar angel of $\Theta = 60°$. The fitted peaks correspond to the pyrrolic nitrogen (light green, $E_{\mathrm{kin}} = 95.90$ eV), iminic nitrogen (blue, $E_{\mathrm{kin}} = 97.86$ eV), two satellite structures (dark green and orange) and a possible surface component (grey, $E_{\mathrm{kin}} = 97.10$ eV).

The distance between the iminic and pyrrolic peaks of about 2 eV is in excellent agreement with literature values [7]. Furthermore, the two shake-up satallite peaks at lower kinetic energies (dark green and orange) result from π-π^* transitions and are typical for these molecules. An additional peak at $E_{\mathrm{kin}} = 97.10$ eV is necessary for a proper signal fit. This light grey component is an evidence of a bonding between the substrate and some molecules in the first interface layer.
So far, multilayers of 2HTPP on Au(111) have been successfully prepared and studied. Recently, the preparation of a 2HTPP monolayer by multilayer desorption has been realized as well. The XPS measurements of this system are scheduled for the upcoming beamtime, in order to confirm our results. Further, photoelectron diffraction measurements of these molecules will be performed in the future.

References

[1] J. P. Collman et al., *Chemical Reviews* **104**, 561 (2004).
[2] J. M. Olson, *Biochimica et Biophysica Acta (BBA) - Reviews on Bioenergetics* **594**, 33 (1980).
[3] W. M. Campbell et al., *The Journal of Physical Chemistry C* **111**, 11760 (2007).
[4] Y. Harima et al., *Applied Physics Letters* **69**, 1059 (1996).
[5] W. M. Sharman et al., *Drug Discovery Today* **4**, 507 (1999).
[6] P. Mehring, SAMs organischer Halbleiter auf Au-Substraten, *Dissertation, TU Dortmund* (2013).
[7] C. Lal et al., *Journal of Materials Research and Technology* **3**, 42 (2014).

Long term XPS analysis of Fe/GaAs(100)

K. Shamout[1,2,*], D. Krull[1,2], P. Espeter [1,2], P. Roese[1,2], C. Keutner[1,2], U. Berges[1,2], C. Westphal[1,2]

[1] Experimentelle Physik I - Technische Universität Dortmund, Otto-Hahn-Str. 4, D-44221 Dortmund
[2] DELTA - Technische Universität Dortmund, Maria-Goeppert-Mayer-Str. 2, D-44221 Dortmund
[*] corresponding author: karim.shamout@tu-dortmund.de

The III-V compound semiconductor gallium arsenide is an applicable substrate for spintronic multi-layer systems due to its electronical und magnetic properties [1, 2, 3]. The structure of the layer 3-system MgO/Fe/GaAs(100) has already been discussed in detail and it has been shown that the Ga-rich surface reconstruction GaAs(4×2) can be investigated beneath the MgO and Fe layer by x-ray photoelectron diffraction (XPD) [4].
Since these XPD measurements last several hours and iron is highly reactive even at pressures p p $\leq 2 \cdot 10^{-10}$ mbar this study focuses on the long term oxidation of an Fe-film prepared on GaAs(100). Therefore, iron was evaporated up to 3 hours on a clean GaAs sample with an As-richer surface reconstruction of a interference of (4×2) and (2×6).
The experiment was performed at U55, Beamline 11 at DELTA. Evaporating 15 min in this vacuum chamber causes 20 Å of iron layers on the sample meaning on each evaporation procedure (3 hours) 180 Å were evaporated.
Figure 1a shows the Fe 3p XPS spectrum which has been obtained after waiting for 135 min. Evaporating for additional 3 hours and waiting for 960 min caused the spectrum in figure 1b.

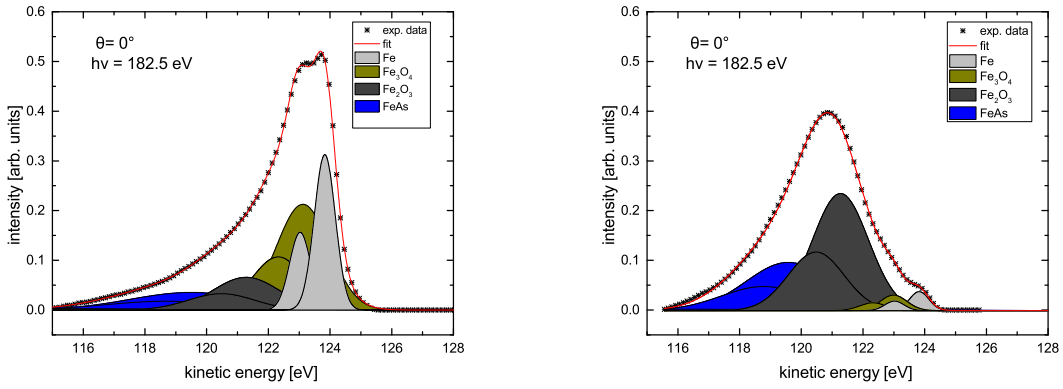

(a) 135 min.

(b) 960 min.

Figure 1: XPS spectra of the Fe-3p Signal on GaAs at p $\leq 5 \cdot 10^{-10}$ mbar after evaporating for 3 hours and waiting for a period of time.

Strong oxide components are visible in both spectra corresponding to Fe_3O_4 or Fe_2O_3 bonds. These components become stronger the longer the sample remains in the vacuum chamber. Interestingly, no FeO has been developed which can be explained by its instability to a temperature of 560°C [5]. Beneath this temperatures it dissolves into pure Fe and Fe_3O_4 or Fe_2O_3 which explains the minimal amount of unoxidized Fe in figure 1b. Since the oxidation only occurs at the surface and As is known to diffuse into the Fe-film, the Fe-As bondings can be explained.
With this work, we could demonstrate that XPD measurements of samples wit pure iron on the surface must be done as quickly as possible to avoid oxidation levels. Otherwise, these components must not be neglected.

References

[1] S.-H. Yang, B. Balke, C. Papp, S. Döring, U. Berges, L. Plucinski, C. Westphal, C.M. Schneider, S.S.P. Parkin, and C.S. Fadley. Determination of layerresolved composition, magnetization, and electronic structure of an Fe/MgO tunnel junction by standing-wave core and valence photoemission. *Phys. Rev.* B, **84**:184410, 2011.

[2] G. Autès, J. Mathon, and A. Umerski. Theory of tunneling magnetoresistance of Fe/-GaAs/Fe(001) junctions. *Phys. Rev.* B, **82**:115212, 2010.

[3] B. Kardasz, E.A. Montoya, C. Eyrich, E. Girt, and B. Heinrich. Spin dynamics and magnetic anisotropies at the Fe/GaAs(001) interface. *Journal of Applied Physics*, **109** (07D337):3, 2011.

[4] D. Handschak, T. Lühr, F. Schönbohm, S. Döring, C. Keutner, U. Berges, and C. Westphal. Structural investigation of the three-layer system MgO/Fe/GaAs(001) by means of photoelectron spectroscopy and diffraction. *Phys. Rev.* B, **88**:045313, 2013

[5] Georg Brauer: *Handbuch der Präparativen Anorganischen Chemie* Band III, Ferdinand Enke Verlag Stuttgart 1981, ISBN 3-432-87823-0

X-ray Scattering

Effect of high temperature treatment on microstructure and electric performance of PQT-12 OFETs

Batbileg Bat-Erdene, Ulrich Pietsch and Souren Grigorian

Department of Physics, Faculty of Science and Technology, University of Siegen, Germany

Poly(3,3‴-didodecylquaterthiophene) (PQT-12) is a solution processable conjugated polymer introduced for application of semiconductor material for OFETs. Its high regioregularity and appropriately distributed side chains along thiophene backbones are designed to provide excellent solution process ability as well as self-assemble.[1] The structure of semicrystalline polymer film comprises the amorphous regions and the embedded small crystallites. These small crystallites and their interconnection are supposed to be mainly responsible for the high charge transfer property of the thin films.[2] Annealing is well-known technique to increase the crystallinity of semicrystalline organic thin films.[3]

In this study we present the results of an in situ annealing study, evaluating the morphology of PQT-12 thin films during annealing treatment. Thin films spin-coated on silicon substrate were probed by grazing incident x-ray diffraction (GIXD) while annealing. The Bragg peaks of crystalline structure measured from the film and their temperature-dependence are shown in *Figure 1*. A significant improvement of the (100) intensity and its higher order peaks are found upon annealing up to 120°C. Interestingly, a second crystalline phase appeared, reaching its highest intensity at 100°C. The intensity of the peaks is starting to decrease with further heating, and complete melting of the polymer occurred at 140°C. After cooling down, the film recrystallized and the Bragg peaks from first crystalline phase are present only at room temperature.

Based on the microstructure the mobility of PQT-12 OFETs was measured as a function of annealing temperature. It allows us to correlate the microstructure with the respective electric performance of the OFETs.

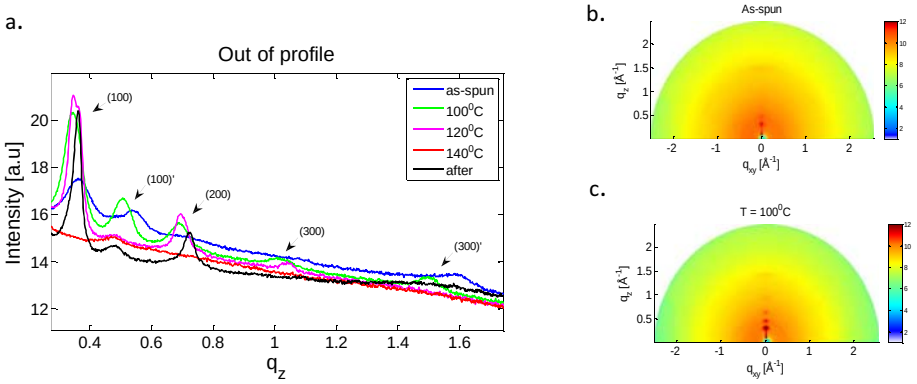

Figure 1. Out-of plane profiles of the thin film diffraction at different temperatures (a), and GIXD patterns of sample at RT and 140^{0}C (b and c).

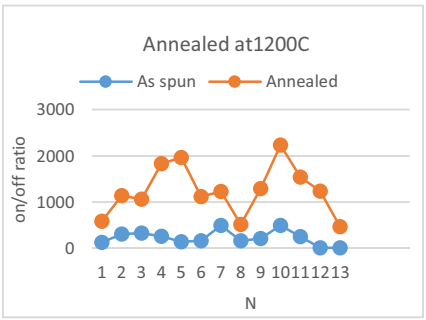

Figure 2. On/off ratio of PQT-12 OFETs before and after annealing. Transistor 1-4, 5-8, 9-12 and 13 has channel length 2.5, 5,10 and 20μm respectively.

For the electrical characterization the PQT-12 OFETs with channel length of 2.5 to 20μm are annealed at 100, 120 and 140°C. The on/off ratio was found to increase by around one order of magnitude for transistors annealed at 100°C and 120°C temperatures. A moderate increase in mobility to be ~5x10^{-3} was measured for transistors annealed at 100°C compared to RT value of ~2x10^{-3}.

Obtained results support, our assumption that the crystallinity of PQT-12 thin films can be increased by annealing at temperatures below its melting point, resulting and an increased electric performance in PQT-12 OFETs.

Reference: s

[1] Beng S. Ong et.al. , *Chem. Eur. J.* **14**, 4766 (2008)

[2] H. Sirringhaus et.al. , *Nature* 401, (1999)

[3] L. H. Jimison, A. Saleo, *Phys. Rev.* B **39**, 2643 (2008)

Supramolecular structure of 2E1H and halogen alkanes

Thomas Büning, Christian Sternemann, Catalin Gainaru, Michael Paulus, Markus Möhlenkamp, Holger Göhring, Jonas Lueg, Roland Böhmer and Metin Tolan

Fakultät Physik/DELTA, Technische Universität Dortmund, 44221 Dortmund, Germany

Hydrogen bonds are essential for the structure and dynamics of alcohols, aqueous solutions, and water. Due to their low tendency of crystallization and large variability in molecular configuration, monohydroxy alcohols (MAs) are often studied as model systems for hydrogen bonded fluids in general [1]. MAs are supposed to form supramolecular structures such as chains and rings via hydrogen bonding in the liquid phase with the hydrogen bonded oxygen atoms as a skeleton inside and the alkyl chains radiating outwards. These supramolecular clusters cause a pronounced absorption band in the mHz to GHz regime, referred to as Debye process. A MA exhibiting a strong Debye process is 2-ethyl-1-hexanol which has been investigated intensively in a wide range of temperature and pressure whereas several striking anomalies were discovered such as a nonlinear temperature evolution with a change of slope at 250 K [2] and an oppositional pressure dependence compared to the ring building MA 4M3H [3]. The origin of these phenomena the Debye process is supposed to be caused by structural rearrangements. Based on the work of Preuß et al. [4] it is known that mixing 2E1H with 2-ethylhexylbromide (2E1Br) which is the same molecule as 2E1H but with a bromine atom instead of a hydroxyl group, showing no Debye process, leads to a reduction of the Debye process. This happens non-linearly with a change of slope at a critical molar fraction of x_{crit}=0.5-0.6. Direct proof of the origin of the structures leading to the Debye process is missing. We used X-ray diffraction (XRD) at beamline BL9 at DELTA with the aim to get insights into the mechanism causing such dynamic anomalies. We diluted 2E1H with the two halogen alkanes 2E1Br and 2-ethylhexylchloride (2E1Cl) for which J. Lueg found similar results during his bachelor thesis (publication in progress). The mixtures were filled into borosilicate capillaries with a diameter of 2 mm and were then mounted to the diffractometer of beamline BL9 with a simple capillary holder. The measurements took place at room temperature and the incident energy was chosen to be 27 keV to be able to penetrate the highly absorbing liquids.
Figure 1 shows the diffraction pattern of 2E1H which is typical for an alcohol [5] it consists of two peaks in the medium *q*-range. The main diffraction peak features a less intense prepeak at smaller *q*-values. This prepeak is due to supramolecular arrangements and displays a typical distance between the oxygen skeletons of the supramolecular clusters separated by the carbon chains of the molecules [5, 6]. Hence there is no prepeak in 2E1Br and 2E1Cl where hydrogen bonds are absent.

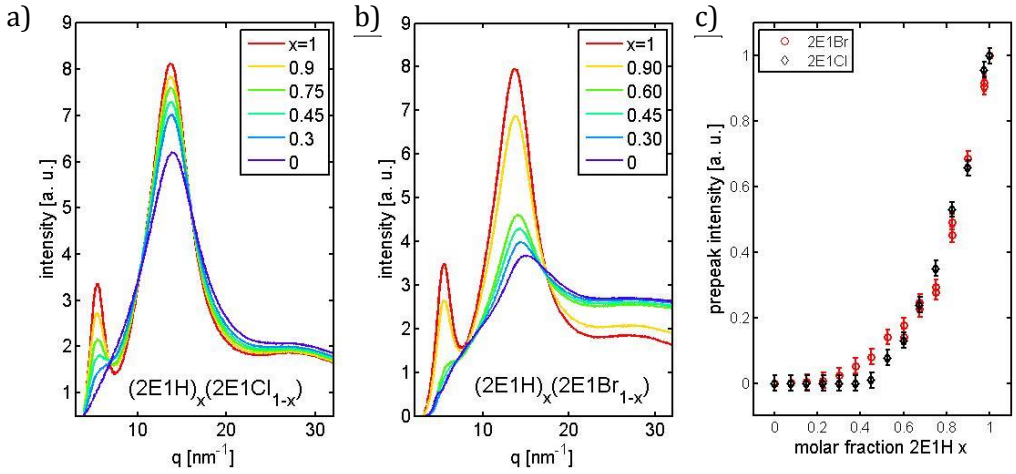

Figure 1: Diffraction pattern of mixtures of 2E1H and 2E1Cl (a), 2E1H and 2E1Br (b), and the integrated intensity of the prepeak as inferred from these pattern (c).

Furthermore figure 1 shows the effect of diluting 2E1H with these halogen alkanes (a, b) leading to a reduction of the prepeak intensity. For a detailed analysis we fitted the whole diffraction pattern with a superposition of two peak shaped functions (Pearson VII) and a linear scaled background arising from inelastic scattered photons and integrated the function displaying the prepeak over the whole *q*-range. This intensity is shown in figure 1c for a range of concentrations of both halogen alkanes. The intensity vanishes completely in both mixtures at a concentration of x=0.2 and a change of slope at x=0.4-0.6 is observed. So the atypical mixing behaviour observed with a dynamic probe is also present in XRD data. Interestingly less 2E1H is necessary to form supramolecular structures in a 2E1Br solution than in 2E1Cl. So 2E1Cl is more efficient in supressing such structures than 2E1Br.

[1] R. Böhmer, C. Gainaru, and R. Richert, Phys. Reports **545**, 125-195 (2014) and references therein; [2] C. Gainaru, S. Kastner, F. Mayr, P. Lunkenheimer, S. Schildmann, H. J. Weber, R. Böhmer et al. Physical review letters **107**, 118304 (2011); [3] S. Pawlus, M. Wikarek, C. Gainaru, M. Paluch, and R. Böhmer, The Journal of chemical physics **139**, 064501 (2013); [4] M. Preuß, C. Gainaru, T. Hecksher, S. Bauer, J. C. Dyre, R. Richert, and R.Böhmer, The Journal of chemical physics **137**, 144502 (2012); [5] M. Tomšič, A. Jamnik, G. Fritz-Popovski, O. Glatter, and L. Vlček, The Journal of Physical Chemistry B **111** 1738-1751 (2007); [6] S. P. Bierwirth, T. Büning, C. Gainaru, C. Sternemann, M. Tolan, and R. Böhmer, Physical Review E **90**, 052807 (2014).

Acknowledgement

We would like to thank the DELTA machine group for providing synchrotron radiation and technical support. Support of this project by the Deutsche Forschungsgemeinschaft (DFG) under Grant No. BO1301/8-2 is gratefully acknowledged. Thoms Büning thanks the BMBF (Project 05K13PE2 within FSP-302) and MERCUR (AN-2014-0036) for financial support, and we acknowledge the support by the cluster of excellence RESOLV funded by the DFG.

Effects of composition and formation conditions on ordering (crystallinity) and nanomorphology of self-assembled films of binary blends of conjugated polymers

Adam Kiersnowski[1], Krzysztof Janus[1], Marzena Grądzka[1], Łukasz Janasz[2], Wojciech Pisula[2], Tomasz Marszałek[2], Wojciech Zajączkowski[2]

[1] Faculty of Chemistry, Wroclaw University of Technology, Wybrzeze Wyspianskiego 27, 50-370 Wroclaw, Poland;
[1] Max Planck Institute for Polymer Research, Ackermannweg 10, 55128 Mainz, Germany;
*correspondence: adam.kiersnowski@pwr.edu.pl

The aim of this project was to investigate the crystalline structure of thin films of poly(3-hexylthiophene) (P3HT) blended with selected perylenediimide derivatives with a special emphasis on the blends with dicyanoperylenedicarboximide (PDI8-CN_2). In addition to the proposed project, the studies of ultra-thin (3-10 nm) films of pure P3HT were studied during the allocated beamtime.

First, it was found that blending P3HT with small molecular compounds clearly hinders crystallization of both phases. Pure P3HT typically forms highly crystalline layers. In the presence of PDI8-CN_2 the crystallinity of P3HT was found significantly reduced which was manifested a significant decrease in intensity diffracted by the polymer. These observations suggested that formation of both polymer and PDI-derivative crystals are driven by interactions between the blend components in solutions. Identifying these interactions is currently the aim of our research on these systems.

Table 1. Comparison of the P3HT layer thickness determined from widths of 100 GIWAXS peaks and AFM. I_{100} are normalized integral intensities of the 100 reflections.

Mean layer thickness (AFM) / [nm]	Mean crystal thickness (normal to the substrate) / [nm]	d_{100} / [nm]	normalized I_{100} / [a.u.]
3	5.8	1.80	0.29
5	8.1	1.70	0.66
7	9.9	1.70	2.26

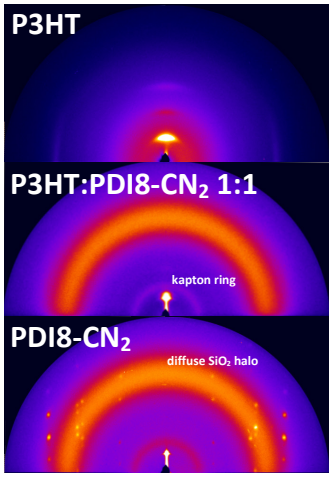

Figure 1. Exemplary GIWAXS patterns recorded for P3HT, PDI8-CN_2 and their 1:1 blend

Studies on the ultra-thin P3HT films provided insights in the structural organization of the layers. The most interesting finding from these measurements was that P3HT reveals no clear π-stacking in the films containing only just several thiophene layers, despite the layers clearly reveal electrical conductivity. The thickness of the films extracted from GIWAXS results was in the perfect agreement with the layer thickness determined by AFM. Relative increase in the intensity of the radiation scattered on h00 layers was found much greater than the relative increase in the thickness, which can only be explained by a gradual increase in lateral sizes of P3HT crystals. This indicates that increasing the layer thickness from 3 to 7 nm leads to a higher coverage of the solid surface with P3HT crystals.

In most of our GIWAXS experiments we did not use the usual vacuum setup and the measurements were performed in the air atmosphere instead. It has, however, turned out that

diffraction patterns recorded for the films with thickness above 50 nm (10keV/ beam width ~1mm/exp. time 900-1000s) had sufficient quality i.e. signal to noise ratios (>10 for weak peaks) and background level were low enough to perform a reasonable quantitative data analysis. In the case of the ultra-thin films the measurements in air were found only partly satisfactory. Hence, the GIWAXS experiments in the air can be considered reasonable for conventional crystalline thin films samples. Increasing the beam energy to avoid background effects (scattering on the air) should, however, be considered in any future experiments.

Acknowledgement:

The work was partly supported by the National Science Centre Poland through the grant 2013/08/M/ST5/00914 (Harmonia 4). The access to the BL9 beamline (15-19.09.2014) granted by a scientific council of DELTA synchrotron facility is gratefully acknowledged. The researchers involved in this project express their gratitude to Dr. Christian Sternemann and Dr. Michael Paulus for their help in the experiments.

The substrate temperature effect on structure and electrical perfromance of α,α'-DH5T thin films

Eduard Mikayelyan[1], Linda Grodd[1], Ullrich Pietsch[1], Sergei Ponomarenko[2] and Souren Grigorian[1]

[1]University of Siegen, Germany

[2]Enikolopov Institute of Synthetic Polymeric Materials RAS, Russia

Thiophene based polymers and oligomers are demonstrating relatively high mobility, excellent luminescence properties which used for application in field effect transistor, solar cells, etc. [1, 2].

The investigation of structure of 5,5′′′′-dihexyl-2,2′:5′,2′′:5′′,2′′′:5′′′,2′′′′-quinquethiophene (α,α'-DH5T) is performed for the films deposited at different substrate temperatures during the vacuum evaporation. The purpose of this study is to reveal the dependence of the substrate temperature on the structural modification and subsequently on the charge mobility changes. The highest mobility of 0.09 $cm^2/(Vs)$ was obtained for the film deposited at 60°C whereas the field effect mobility of 0.06 $cm^2/(Vs)$ and 0.052 $cm^2/(Vs)$was obtained for films deposited at 90°C and 36°C substrate temperatures, respectively. The grazing incidence x-ray diffraction (GIXD) patterns and azimuthally integrated line profiles for the different deposition temperatures are shown in the figure. In particular, the Bravais lattice parameters are calculated from three 110, 020 and 120 reflections and tilt of the molecules from up standing positions. The 020 reflections provide the information associated to π-π stacking. We found that increase of π-π structure order causes an improvement of the field effect mobility of OFET devices. The complete structure and morphology investigation with the correlation to the electrical performance reveals that the highest crystallinity is responsible for better electrical performance in OFETs. This work was supported by BMBF project No. 05K13PS4.

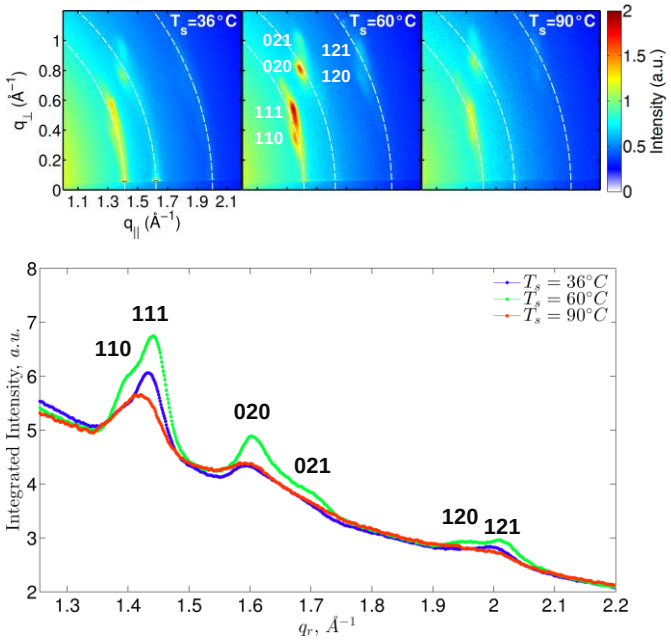

Figure: 2D GIXD patterns (top), the integrated intensity of reflections obtained from GIXD patterns of DH5T oligomer deposited at three different substrate temperatures: 36°C, 60°C and 90°C, respectively (bottom).

References

1. Ponomarenko, S.A., et al., *Decyl-end-capped thiophene-phenylene oligomers as organic semiconducting materials with improved oxidation stability.* Chemistry of Materials, 2006. **18**(2): p. 579-586.
2. Sirringhaus, H., et al., *Two-dimensional charge transport in self-organized, high-mobility conjugated polymers.* Nature, 1999. **401**(6754): p. 685-688.

Analysis of crystal structure of highly crystalline thin polymer films

Authors: Zahra Molla[1], Ullrich Pietsch[1], Ilja Vladimirov[2]

1) Solid state group physics Department University of Siegen **2)** BASF Company

According to a shared project between BASF Company and University of Siegen we had to determine the crystal structure of new oligomer molecules with exceptionally high electric mobility prepared as thin films. By previous beamtime at BL9 of Delta (June 2015), the first experimental 2D GISAXS pattern of the new polymer has been recorded using PILATUS detector. Unfortunately detailed information about the chemical nature of the molecules is secret and therefore the scheme of the molecule cannot be shown. The 2D GISAXS pattern exhibited a large number of Bragg spots arranged along q_z and q_{xy} (Fig.1). The analysis of these data could give us more information about crystalline structure of this new polymer and it was found out that the crystal structure can be described by triclinic crystal system and the crystal structure contains only one molecular layer visible along 11L where each molecule is tilted by a small angle with respect to the surface normal. The polymer film is composed by nanocrystals and all nanocrystals are stacked along the surface normal. All peaks could be indexed considering triclinic crystal structure with oblique 2D lattice parallel the surface (Fig.2). Finally the unit cell could be described by these lattice parameters and the angles between them: a= 8.54 (Å) , b=5.46 (Å) , c=17.45 (Å) and α=99.35° , β=90.31° , γ=112.71° .

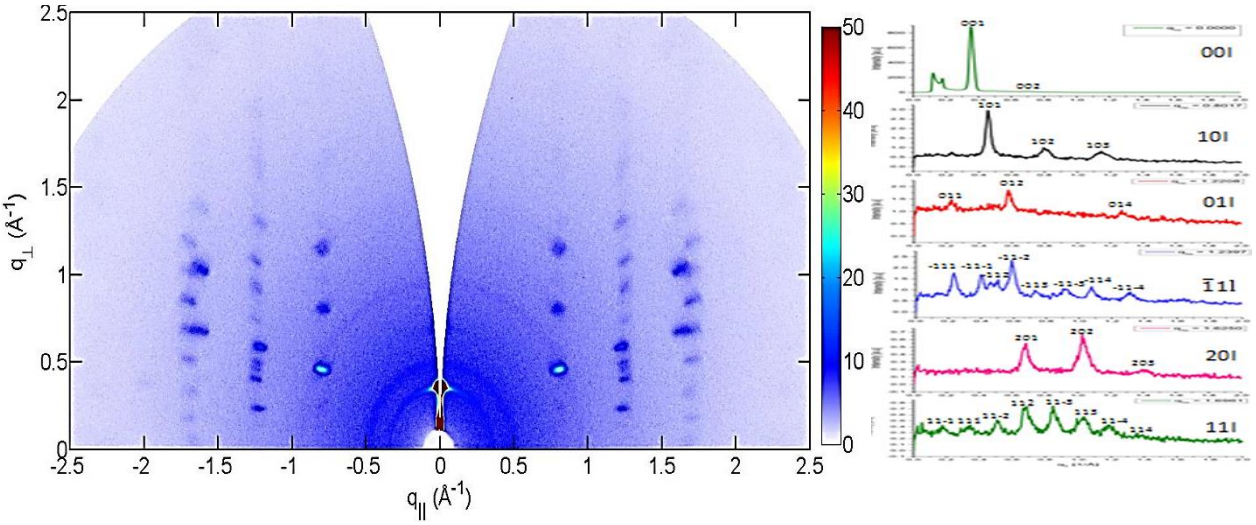

Fig.1 (a) Shows the first two-dimensional GIWAXS plots of the new polymer taken at BL9 of DELTA; **(b)** Out-of-plane line profiles, q_z is the perpendicular wave vector transfer with respect to substrate surface.

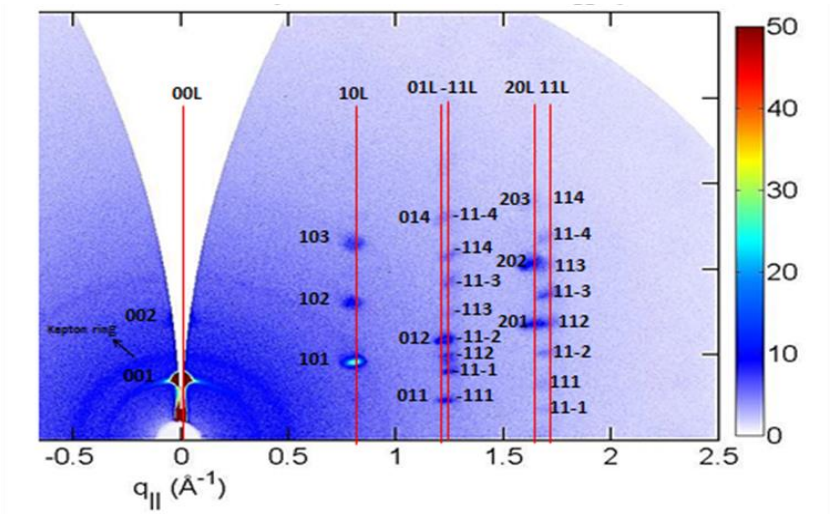

Fig.2 Indexed Bragg-spots of 2D GISAXS pattern considering triclinic crystal structure.

Surface Organization of Columnar Liquid Crystals in Thermally Evaporated and Spin-Coated Films

Wojciech Zajaczkowski,[1] Juliana Eccher,[2] Harald Bock,[3] Ivan H. Bechtold,[2] Wojciech Pisula[1,4,*]

[1]Max Planck Institute for Polymer Research, Ackermannweg 10, 55128 Mainz, Germany
[2]Departamento de Física, Universidade Federal de Santa Catarina–UFSC, 88040-900 Florianópolis, Santa Catarina, Brazil
[3]Centre de Recherche Paul Pascal, Université de Bordeaux & CNRS, 115 Avenue Schweitzer, 33600 Pessac, France
[4]Polymer Engineering and Technology Division, Wroclaw University of Technology, Wybrzeze Wyspianskiego 27, 50-370 Wroclaw, Poland
* Email: pisula@mpip-mainz.mpg.de

In contrast to our previous studies on conjugated polymers,[1,2] during our beamtime at the beamline 9 of the DELTA electron storage ring in Dortmund in March 2015 we have investgated the surface organization of a columnar liquid crystals, namely a diimidodiester derivative of benzo[*ghi*]perylene (see right Scheme) deposited either by spin-coating or by thermal evaporation into a typical OLED device. These results have been recently published in ACS Appl. Mater. Interfaces.[3]

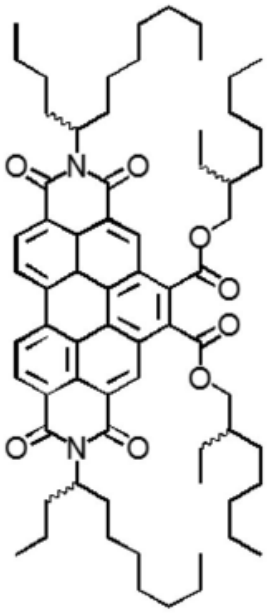

To investigate the molecular organization and the thermal annealing effects for the evaporated films, GIWAXS measurements (Figure 1) were performed for a diode structure in the regions outside and under the metallic electrode before and after annealing the device at 120 °C for 4 h. For the as evaporated films three distinct scattering spots in the small-angle region can be observed which are characteristic for a hexagonal arrangement of columns. The hexagonal lattice parameter determined from the h00 and 0k0 peak positions is ahex = 2.15 nm and is in agreement with the value found for the bulk structure. Thereby, the columnar axis is oriented parallel to the surface. The edge-on arrangement of the molecules was confirmed by in-plane π-stacking 001 reflection related to an intermolecular distance of 0.35 nm. The unit cell parameters are identical to the bulk and verify liquid crystallinity in the evaporated film. After annealing the film at 120 °C for 4 h, significant changes in the structure of the film became evident by the appearance of new scattering peaks (Figure 1a). The increased number of reflections is characteristic for an increased crystallinity due to the thermal annealing. The π-stacking peak, labeled as 002, is shifted from in-plane to an off-equatorial position indicating a molecular tilting (inset in Figure 1a). Thereby, the molecular plane was tilted by ca. 30° toward the surface maintaining an unchanged intermolecular distance of 0.35 nm. However, a minor fraction of molecules remained edge-on as evident from the low intensity 001* reflection. The columnar arrangement is slightly distorted from the hexagonal lattice to an oblique one with parameters of a = 2.19 nm and b = 2.07 nm. Within the stacks the molecules are assembled in a staggered fashion as implied by an additional off-equatorial reflection at q = 0.92 $Å^{-1}$ on the hk1 scattering line related to the doubled π-stacking distance of 0.68 nm. In this packing motif neighboring molecules are flipped by 180° so that every second disc possesses an identical positional arrangement in the column.

The GIWAXS pattern in Figures 1b indicated that the molecular organization is not influenced by the presence of the metallic electrode as a second surface on top of the film. In contrast to

spin-coated films, the GIWAXS patterns for the evaporated films after annealing were almost identical in the open area and in the area under the electrode (compare Figures 1a and 1b). For the evaporated films, the increase in crystallinity and considerable reorganization are mainly attributed to the substrate. The importance of the surface on the initiation of nucleation and crystallinity has been reported for various polymers and also for discotic liquid crystals.

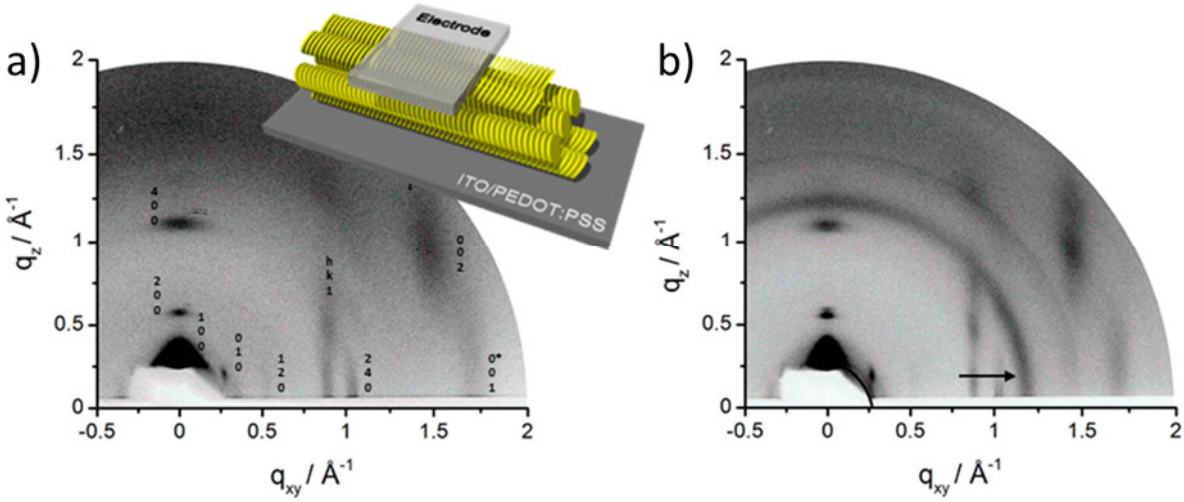

Figure 1. a) GIWAXS of evaporated perylene film measured in the open area after annealing. Reflections are assigned by Miller's indices; reflections* are attributed to the minor edge-on fraction (inset illustrates the corresponding molecular organization in the evaporated film); b) GIWAXS of evaporated film under the electrode area after annealing (arrow indicates isotropic reflection of the metal electrode).

1. F. Hinkel, T. Marszalek, W. Zajaczkowski, S. R. Puniredd, M. Baumgarten, W. Pisula, K. Müllen, *Chem. Mater.* **2014**, *26*, 4844.
2. M. Kuhn, J. Ludwig, T. Marszalek, T. Adermann, W. Pisula, K. Müllen, A. Colsmann, M. Hamburger, *Chem. Mater.* **2015**, *27*, 2678.
3. J. Eccher, W. Zajaczkowski, G. C. Faria, H. Bock, H. von Seggern, W. Pisula, I. H. Bechtold, *ACS Appl. Mater. Interfaces* **2015**, *7*, 16374.

"Structural investigations of conjugated polymers on the flexible substrate"

Kateryna Shchyrba[1], Ullrich Pietsch[2], Klaus Scheulen[2] , Souren Grigorian[1]

[1] Department of Physics , Faculty of Science and Technology, University of Siegen, Germany

[2]Institut für Textiltechnik (ITA), RWTH Aachen, Germany

Nowadays, stretchable organic electronics is a promising field [1] in terms of scientific and industrial application. The main task of research is the deposition of different organic compounds with special electrical (conductive/semiconductive) [2] or magnetic properties [3] onto flexible substrates for further implementation in organically- or biologically- based devices. There are different basic materials, such as: kapton, polyethylene, paper, polyimide, textiles, fibers, Si-elastomers, etc. [4][5] presently used as substrates. Unfortunately, up to date a lot of questions appeared regarding the influence of particular physical properties on the functionality of these devices such as the flexibility of the substrates, the influence of an external stretching force and other need to be answered and are part of our current scientific activities. In particular we conducted in-situ X-ray structural investigations of conjugated polymer films covered on top of different flexible/stretchable substrates. Using the grazing incidence X-ray diffraction method (GIXD) at BL9 at DELTA we investigated the behavior of the polymer morphology under external force, applied via uniaxial stretching. We made in- situ studies of PQT-12 and P3HT polymers drop cast onto Si-elastomer substrates. For stretching we applied a specially designed motorized stage, constructed at the University of Siegen, allows for application of different forces. The results, presented in the graph below, shows significant changes of polymer structural peaks as a function of elongation and comparison to a plain references elastomer and a coated one.

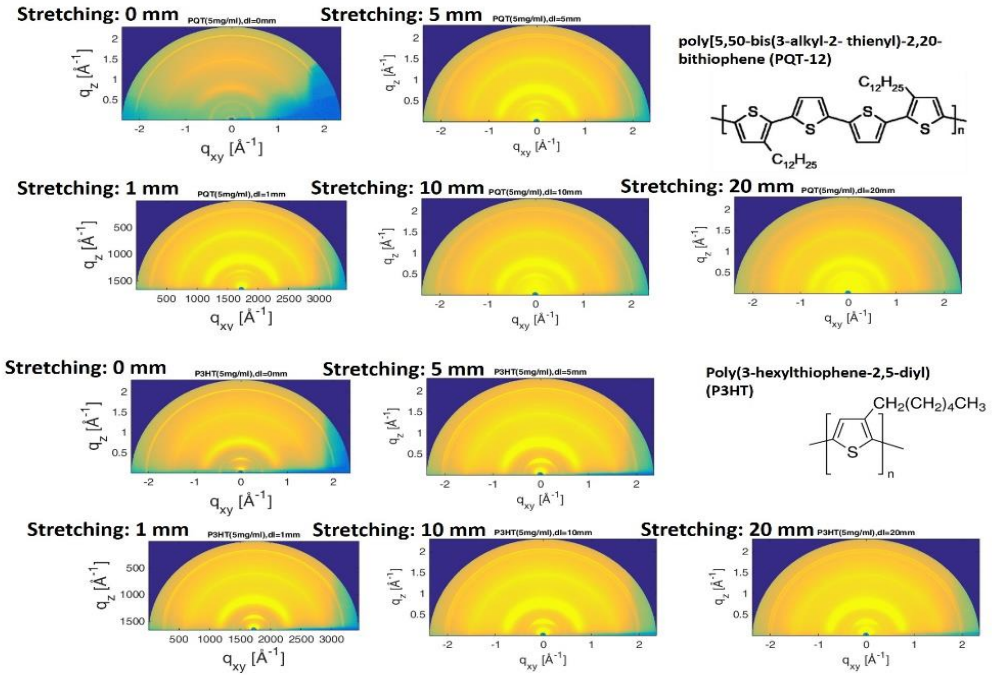

Fig. 1 XRD patterns of different conjugated polymers during the stretching procedre.

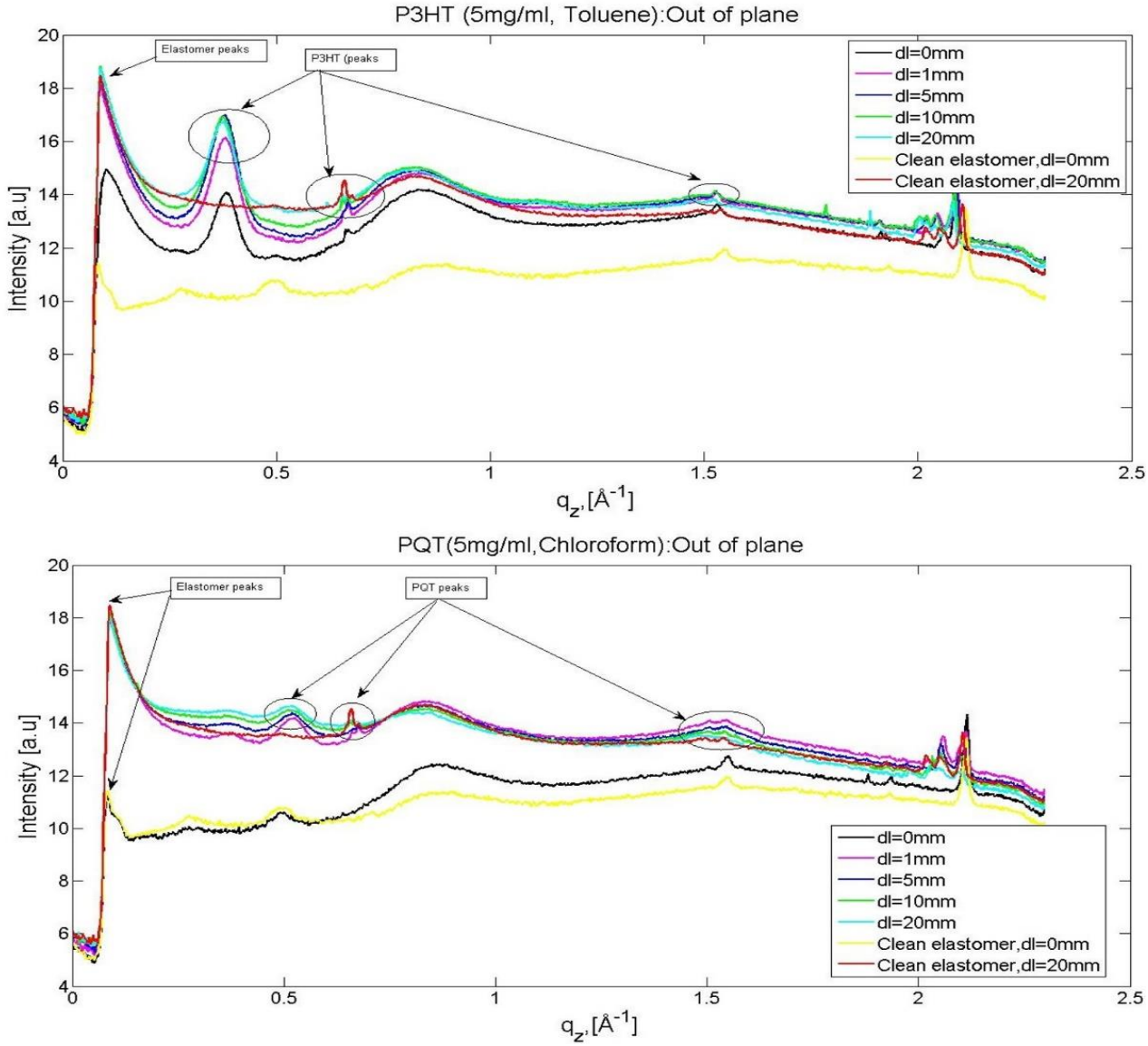

Fig. 2 Out of plane profiles for P3HT and PQT-12 : comparison of the structure after sample alongation and film deformation

On the picture above, one can see a remarkable broadening of the polymer peak during the stretching of the sample and also a angular shifting of peaks towards smaller angles indicating expansion of interplanar distances during deformation. For these finding one can conclude that external force and surface effects can induce strong modifications of the polymer structure and a rearrangement of polymer lamellae with respect to the substrate.

References

[1] P. M. Beaujuge and J. M. J. Fréchet, "Molecular Design and Ordering Effects in π-Functional Materials for Transistor and Solar Cell Applications," *J. Am. Chem. Soc.*, vol. 133, no. 50, pp. 20009–20029, Dec. 2011.

[2] S. Holliday, J. E. Donaghey, and I. McCulloch, "Advances in Charge Carrier Mobilities of Semiconducting Polymers Used in Organic Transistors," *Chem. Mater.*, vol. 26, no. 1, pp. 647–663, Jan. 2014.

[3] V. A. Dediu, L. E. Hueso, I. Bergenti, and C. Taliani, "Spin routes in organic semiconductors," *Nat. Mater.*, vol. 8, no. 9, pp. 707–716, Sep. 2009.

[4] J. A. Rogers, T. Someya, and Y. Huang, "Materials and Mechanics for Stretchable Electronics," *Science*, vol. 327, no. 5973, pp. 1603–1607, Mar. 2010.

[5] M. Stoppa and A. Chiolerio, "Wearable Electronics and Smart Textiles: A Critical Review," *Sensors*, vol. 14, no. 7, pp. 11957–11992, Jul. 2014.

Near surface behavior of a bicontinuous microemulsion under high hydrostatic pressure conditions

Melanie Berghaus[1], Michael Paulus[2], Paul Salmen[2], Samy Al-Ayoubi[1], Metin Tolan[2], and Roland Winter[1]

1 Physikalische Chemie I- Biophysikalische Chemie, TU Dortmund, D-44227 Dortmund, Germany
2 Fakultät Physik/DELTA, TU Dortmund, D-44221 Dortmund, Germany

The transition from a fluid lamellar phase to a bicontinuous lipid phase plays, for example, an important role in biomembrane phase transitions such as vesicle fusion. This transition has been studied for several lipids forming highly ordered cubic lipid phases [1–3], and can be initiated, for example, using pressure-jump methodologies. What was lacking so far, though also of high biological relevance, was the effect of interfaces and conformational disorder on such kind of phase transition. In order to mimic these effects, we studied the pressure-dependent phase behavior of a disordered bicontinuous microemulsion (BME) in the presence of a solid interface by X-ray reflectometry (XRR). BME are ternary systems consisting of water, oil and a surfactant occupying the interface between the latter. Interestingly, some BME show a transition from a lamellar phase close to a surface to a bicontinuous phase when approaching the bulk, as revealed by neutron reflectometry, recently.[4,5] We investigated how high hydrostatic pressure (HHP) influences the structure of this transition region. HHP is not only an important feature in marine environments and biotechnological applications, but can also be used as a physical parameter to study the mechanism and kinetics of lipid phase transitions and to continuously tune the lattice constant of lipid phases.

Experiments were performed at DELTA BL9 using a high pressure cell for XRR measurements on solid/liquid interfaces built by the Tolan group [6]. We studied the near surface phase behavior of a BME consisting of equal volumes of water and oil (n-octane) and 16 wt% of the surfactant tetraethylene glycol decanoyl ether, $C_{10}E_4$, on a hydrophilic Si wafer at 20 °C in the pressure range from 1 to 4000 bar. A high incident photon energy of 27 keV was used in order to obtain sufficient transmission through the high hydrostatic pressure cell with the strongly scattering diamond windows as well as the microemulsion (path length ~1 cm). Scans covered an angular range of 0-1.2°.

Figure 1 displays the recorded reflectometry data for water as well as the BME at 50 bar and at 4000 bar. In both reflectivity curves of the microemulsion, a correlation peak is visible, which shifts towards higher angles upon pressurization. This correlation peak refers to a length scale of about 150 Å for 50 bar and of about 115 Å for the 4000 bar measurement, respectively. It can thus be attributed to the lamellar phase which is compressed upon pressurization, the lattice compressibility amounting to 0.01 Å bar^{-1}.

Calculation of the real space electron density profiles (EDP) using Parratt algorithm [7] (Figure 2) allows a more detailed insight into the system. The EDP shows clearly the Si wafer at $z = 0$ with the highest electron density. The thin hydrophilic SiO_2 layer with a

slightly lower electron density is also reflected in all profiles. A thin layer with an electron density close to water can be identified near the hydrophilic surface. Further, thicker layers close to the surface of the Si wafer are visible as oscillations in the electron density, which approach the electron density of the bulk solution at a distance of about 450 Å away from the surface. Upon pressurization to 4000 bar, these oscillations become more pronounced, indicating higher ordering of the lamellae. Further, the maxima of oscillations shift towards the surface at 4000 bar. This indicates a compression of the lamellar layers. The latter was found to be reversible upon pressure release. We did not find an increase in the number of layers upon compression, which might be attributed to the low curvature of the surfactant within the bicontinuous phase of a microemulsion consisting of equal volumes of water and oil [8].

Our results clearly show that bicontinuous microemulsions form a lamellar phase close to hydrophilic interfaces, which are markedly compressible. Pressure increases the lamellar order, but does not significantly extend the correlation length of lamellar order induced by the presence of the hydrophilic interface. A biological implication of this finding would be that cellular interfaces would not hinder cellular fusion events under pressure by preventing the formation of disordered bicontinuous phase intermediates.

[1] V. Cherezov, D. P. Siegel, W. Shaw, S. W. Burgess, M. Caffrey, *J. Membr. Biol.* **2003**, *195*, 165–182.
[2] J. Lendermann, R. Winter, *Phys. Chem. Chem. Phys.* **2003**, *5*, 1440–1450.
[3] C. Conn, O. Ces, X. Mulet, S. Finet, R. Winter, J. Seddon, R. Templer, *Phys. Rev. Lett.* **2006**, *96*, 108102.
[4] M. Kerscher, P. Busch, S. Mattauch, H. Frielinghaus, D. Richter, M. Belushkin, G. Gompper, *Phys. Rev. E*, **2011**, 83, 030401.
[5] X.-L. Zhou, L.-T. Lee, S.-H. Chen, R. Strey, *Phys. Rev. A* **1992**, *46*, 6479–6489.
[6] F. J. Wirkert, M. Paulus, J. Nase, J. Möller, S. Kujawski, C. Sternemann, M. Tolan, *J. Synchrotron Radiat.* **2014**, *21*, 76–81.
[7] L. G. Parratt, *Phys. Rev.* **1954**, *95*, 359–369.
[8] D. D. Lee, S. H. Chen, *Phys. Rev. Lett.* **1994**, *73*, 106–109.

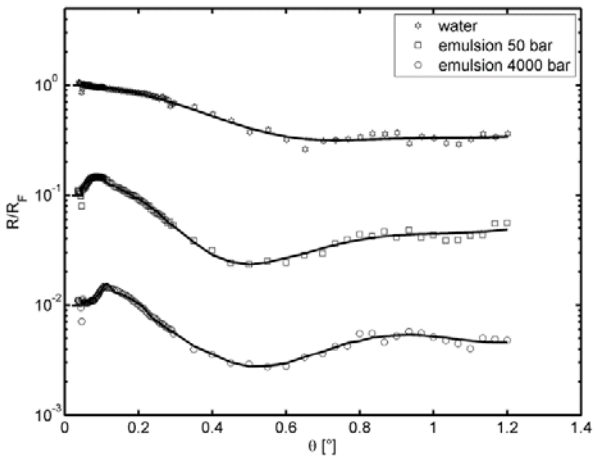

Figure 1: X-Ray reflectivity profiles of water (astra), and the bicontinuous microemulsion at 50 bar (squares) and 4000 bar (diamonds) with corresponding fits calculated using Parrat algorithm [7](solid lines).

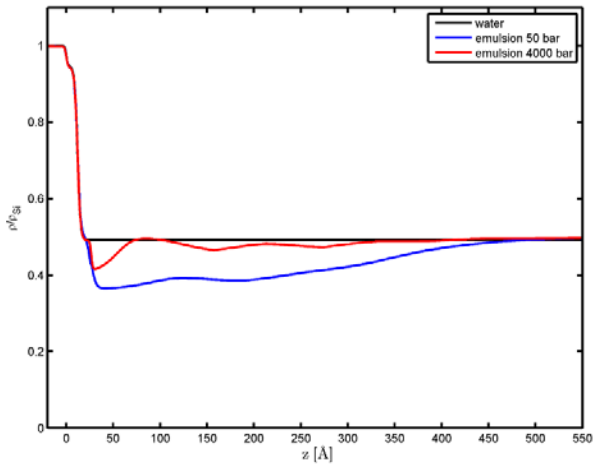

Figure 2: Electron density profiles of water (black) and the bicontinuous microemulsion at 50 bar (blue) and 4000 bar (red) corresponding to the experimental data of Figure 1.

Ions at hydrophobic interfaces

Yury Forov[1], Michael Paulus[1], Paul Salmen[1], Karin Julius[1], Hendrik Rahmann[1], and Metin Tolan[1]

[1]Fakultät Physik/DELTA, TU Dortmund, 44221 Dortmund, Germany

The investigation of the microscopic structure of water is one of the important areas of modern research [1]. In particular, the understanding of the behavior of water at interfaces is essential for the explanation of interfacial phenomena in several natural and technological environments [2]. Much pioneer work has been done to describe the interactions between ions and hydrophobic surfaces, but a complete description of the physical mechanism for the hydrophobic interaction is still pending [3]. From MD simulations, different parameters like polarizability, size and charge have been identified, effecting the accumulation of ions at interfaces.

We measured the adsorption behavior of ions at hydrophobic interfaces as a function of different ion radii and concentrations. The experiment was performed at beamline BL 9 using the high energy x-ray reflectivity setup and a cell developed by I. Kiesel [4]. The hydrophobic surface was provided by coating of silicon wafers with octadecyltrichlorosilane (OTS) as described in [5]. Afterwards, different salts (with different combinations from alkali metals and halogens, e.g. NaCl, NaBr or RbCl) were diluted in MilliQ water in different concentrations and given into the sample cell.

The pure surface was first characterized in MilliQ water. Afterwards, the water was removed and the salt solution was filled into the cell. The reflectivity data and the corresponding electron density profiles of NaCl and NaBr, obtained by a refinement of the XRR data, are shown in figure 1.

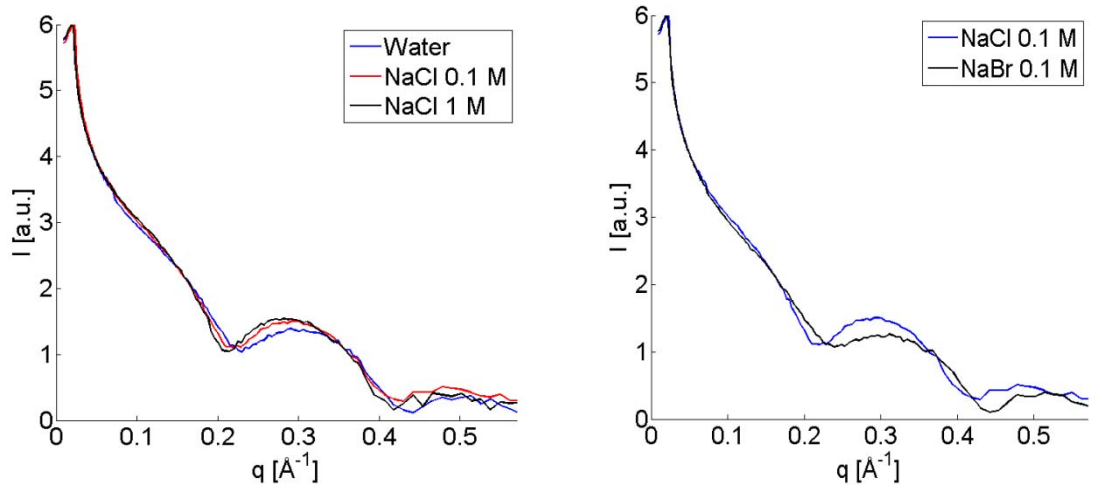

Figure 1: XRR data of pure water and NaCl solutions with different concentrations (left) and comparison of the XRR data of 0.1 M NaCl and NaBr solutions on an OTS-coated silicon wafer.

The left side of figure 1 shows the XRR data for pure water and NaCl solutions with different concentrations on the hydrophobic surface of an OTS-coated silicon wafer. Systematic changes in the reflectivity curves of the first minimum around q = 0.21 Å^{-1} are observed. The changes in the q-position of the minimum indicate a structural change of the solid-liquid interface, which seems to change as a function of the salt concentration. The right side of

figure 1 shows a comparison of the reflectivity curves of 0.1 M concentrated NaCl and NaBr. Again, the minima positions of the reflectivity curves are different for each salt. This indicates a different adsorption behavior for different salt types. Thus, with changing ion radius the reflectivity curves are varying. Corresponding to the reflectivity curves on the right side of figure 1, electron density profiles can be calculated. The electron density profiles are shown in figure 2.

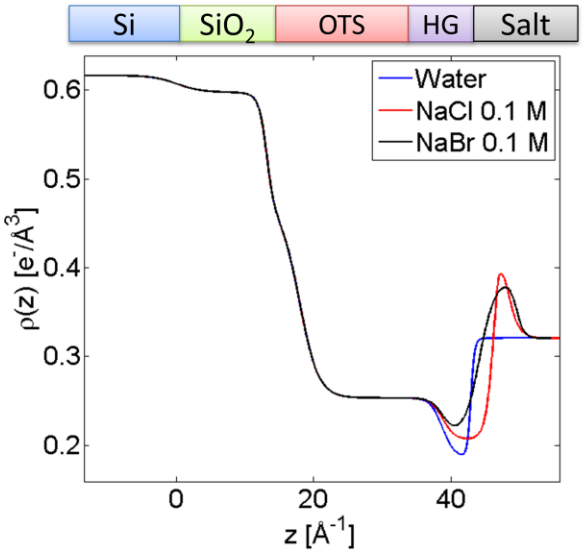

Figure 2: Electron density profiles of water, 0.1 M concentrated NaCl and 0.1 M concentrated NaBr on an OTS-coated silicon wafer calculated from the reflectivity curves shown on the right side of figure 1. Between the OTS-coating and the salt a hydrophobic gap (HG) occurs.

Figure 2 shows electron density profiles of water, 0.1 M concentrated NaCl and 0.1 M concentrated NaBr solution on an OTS-coated silicon wafer. The profiles show the existence of the in [5] predicted hydrophobic gap as well as a change in the shape of the hydrophobic gap with different salts. Further analysis of all measurements will help us to understand the behavior of ions at hydrophobic interfaces as well as the behavior of the hydrophobic gap. A hydration enthalpy dependent layer formation will be analyzed in detail.

Acknowledgment:

The authors thank the DELTA machine group for providing synchrotron radiation. This work was supported by the Cluster of Excellence RESOLV (EXC 1069) funded by the Deutsche Forschungsgemeinschaft. PS acknowledges the DFG Forschergruppe 1979 for funding.

References:

[1] A. Nilsson and L.G.M. Pettersson, Chem. Phys. **389**, 1 (2011);
[2] D. Chandler, Nature **437**, 640-647 (2005);
[3] S. H. Donaldson et al., Langmuir **31**, 2051-2064 (2015);
[4] I. Kiesel et al., Langmuir **30**, 2077 (2014);
[5] M. Mezger et al., PNAS **103**(49) 18401-18404 (2006)

The adsorption of lysozyme at the titanium dioxide - water interface as a function of pressure

Yury Forov[1], Michael Paulus[1], Paul Salmen[1], Andreas Behrendt[2], Julian Schulze[1], Thomas Riedl[2], and Metin Tolan[1]

[1]Fakultät Physik/DELTA, TU Dortmund, 44221 Dortmund, Germany
[2]Bergische Universität Wuppertal, 42119 Wuppertal, Germany

The investigation of solid-liquid interfaces is one of the important areas of modern research. In particular, the adsorption of proteins and nanoparticles at liquid and solid surfaces is in the focus of actual research [1, 2]. Interfaces between liquids and solids, the solid-liquid interfaces, occur for example on implants in the body or in production facilities in the food industry. Especially in the case of the dental medicine, titanium with a TiO_2 layer on top is used as a preferred implant material. The study of the adsorption of proteins is in so far important as adsorbed proteins can initiate the formation of biofilms, which is usually resulting in unwanted consequences [3]. A biofilm on an implant surface may support the growth of bacteria, so that the risk of an inflammatory reaction rises [4]. Here, the use of high energy x-rays allows the analysis of buried interfaces and thin films in-situ by reflectivity measurements.

We measured the adsorption of lysozyme at the titanium dioxide - water interface as a function of pressure for pressures between 60 and 4530 bar. The experiment was performed at beamline BL 9 using the high energy x-ray reflectivity setup and a high pressure cell developed by F. Wirkert [5]. The titanium dioxide surfaces were prepared by a coating of a silicon wafer with a TiO_2 layer on top, gained by atomic layer deposition from $TiCl_4$ and H_2O. Afterwards, lysozyme was diluted in a BisTris buffer solution in a concentration of 1 mg/ml and given into the sample cell. The pressure was increased from 60 to 4530 bar and afterwards decreased again to 60 bar.

The reflectivity data and the corresponding electron density profiles, obtained by a refinement of the XRR data, are shown in figure 1 as a function of temperature.

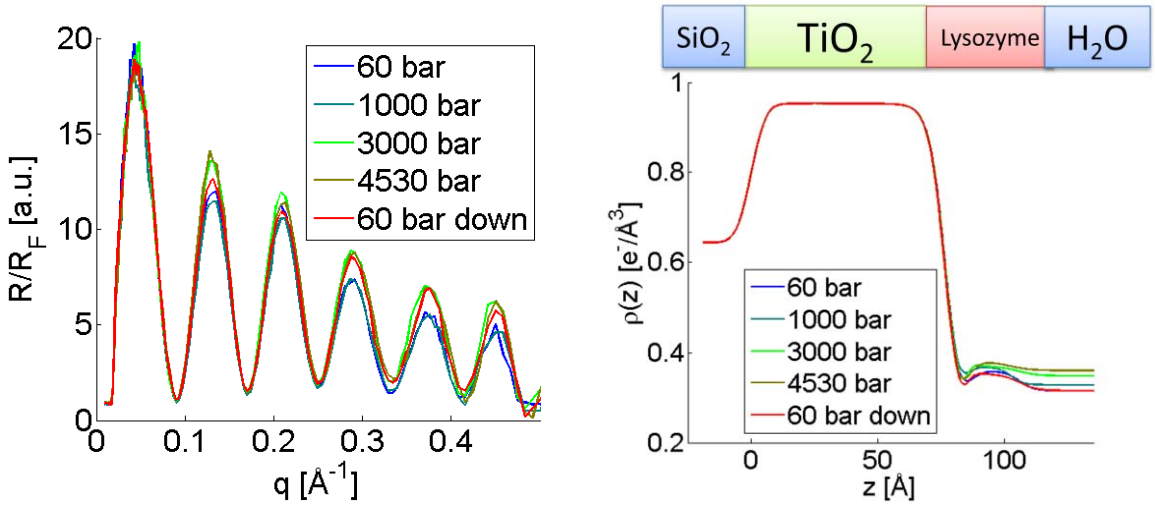

Figure 1: XRR data of lysozyme solution as a function of pressure in Fresnel representation (left) and corresponding electron density profiles (right).

Figure 1 shows the adsorption behavior of lysozyme on TiO_2 as a function of pressure. The oscillations in the reflectivity profiles on the left side of figure 1 correspond to the TiO_2 layer on the silicon wafer, while changes in the reflectivity amplitude correspond to changes in the adsorption behavior of lysozyme. On the right side of figure 1 corresponding electron density profiles are shown. For further analysis of the adsorption behavior of lysozyme, volume fraction profiles are calculated from the electron density profiles.

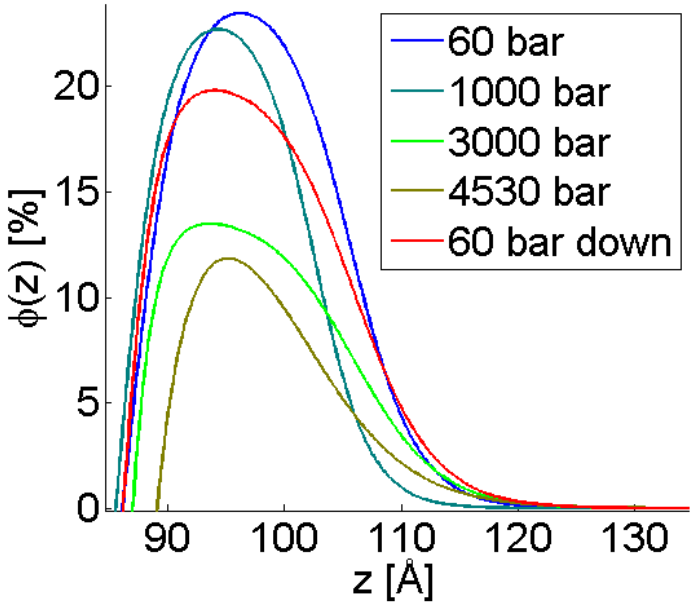

Figure 2: Volume fraction profiles as a function of pressure describing the covered wafer surface by lysozyme.

Figure 2 shows the surface coverage as a function of the layer height. For increasing pressures up 4530 bar the surface coverage decreases from 23.45 % to 11.84 % and increases again to 19.80 % for decreasing pressures down to 60 bar again. This behavior is contrary to the expected behavior of lysozyme adsorption as a function of pressure, since it is known that rising pressure leads to destabilization of lysozyme and destabilized lysozyme uses to better adsorb on a surface. For further explanation of the results, measurements of lysozyme adsorption on TiO_2 as a function of the pH-value are planned, which will give us a new insight into the adsorption behavior of lysozyme on this material and thus may give us new hints for the explanation of the results.

Acknowledgment:

The authors thank the DELTA machine group for providing synchrotron radiation. This work was supported by the Cluster of Excellence RESOLV (EXC 1069) funded by the Deutsche Forschungsgemeinschaft. PS acknowledges the DFG Forschergruppe 1979 for funding.

References:

[1] T. Brenner et al., J. Colloid Interface Sci., **374**, 287–290 (2012).
[2] I. Kiesel et al., Langmuir **30**, 2077 (2014).
[3] C. Czeslik, Chem. Unserer Zeit, **40** (4), 238–245 (2006).
[4] P. S. Stewart and J. W. Costerton, Lancet **358** (9276), 135–138 (2001).
[5] F. J. Wirkert et al., Journal of Synchrotron Radiation 21, 76 (2014)

The adsorption of lysozyme at the titanium dioxide - water interface as a function of temperature

Yury Forov[1], Michael Paulus[1], Paul Salmen[1], Andreas Behrendt[2], Christopher Weis[1], Susanne Dogan[1], Thomas Riedl[2], and Metin Tolan[1]

[1]Fakultät Physik/DELTA, TU Dortmund, 44221 Dortmund, Germany
[2]Bergische Universität Wuppertal, 42119 Wuppertal, Germany

The investigation of solid-liquid interfaces is one of the important areas of modern research. In particular, the adsorption of proteins and nanoparticles at liquid and solid surfaces is in the focus of actual research [1, 2]. Interfaces between liquids and solids, the solid-liquid interfaces, occur for example on implants in the body or in production facilities in the food industry. Especially in the case of the dental medicine, titanium with a TiO_2 layer on top is used as a preferred implant material. The study of the adsorption of proteins is in so far important as adsorbed proteins can initiate the formation of biofilms, which is usually resulting in unwanted consequences [3]. A biofilm on an implant surface may support the growth of bacteria, so that the risk of an inflammatory reaction rises [4]. Here, the use of high energy x-rays allows the analysis of buried interfaces and thin films in-situ by reflectivity measurements.

We measured the adsorption of lysozyme at the titanium dioxide - water interface as a function of temperature for temperatures between 20°C and 80°C. The experiment was performed at beamline BL 9 using the high energy x-ray reflectivity setup and a cell developed by I. Kiesel [2]. The titanium dioxide surfaces were prepared by a coating of a silicon wafer with a TiO_2 layer, gained by atomic layer deposition from $TiCl_4$ and H_2O. Afterwards, lysozyme was diluted in a phosphate buffer solution in a concentration of 1 mg/ml and given into the sample cell.

The pure surface was first characterized in pure buffer solution. Afterwards, the buffer was removed and the lysozyme solution was filled into the cell. The reflectivity data and the corresponding electron density profiles, obtained by a refinement of the XRR data, are shown in figure 1 as a function of temperature.

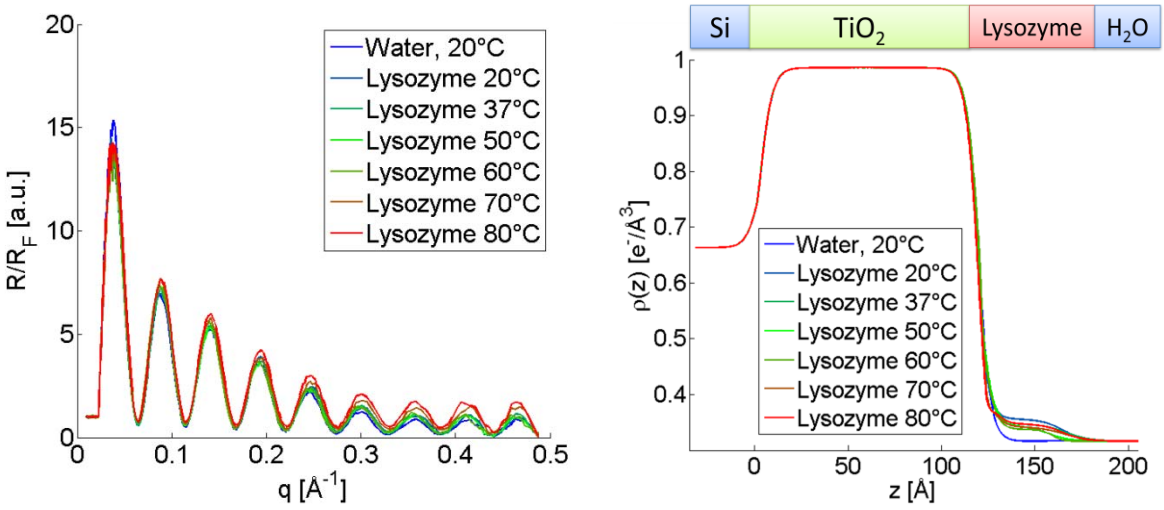

Figure 1: XRR data of lysozyme solution as a function of temperature in Fresnel representation (left) and corresponding electron density profiles (right).

The oscillations in the reflectivity profiles on the left side of figure 1 correspond to the TiO_2 layer on the silicon wafer, while changes in the reflectivity amplitude correspond to changes in the adsorption behavior of lysozyme. The electron density profile on the right side of figure 1 demonstrate the desorption behavior of lysozyme as the electron density decreases around a value of z between 130 Å and 180 Å with increasing temperature. To clarify this result, volume fraction profiles have been calculated from the electron density profiles and are shown on the left side of figure 2.

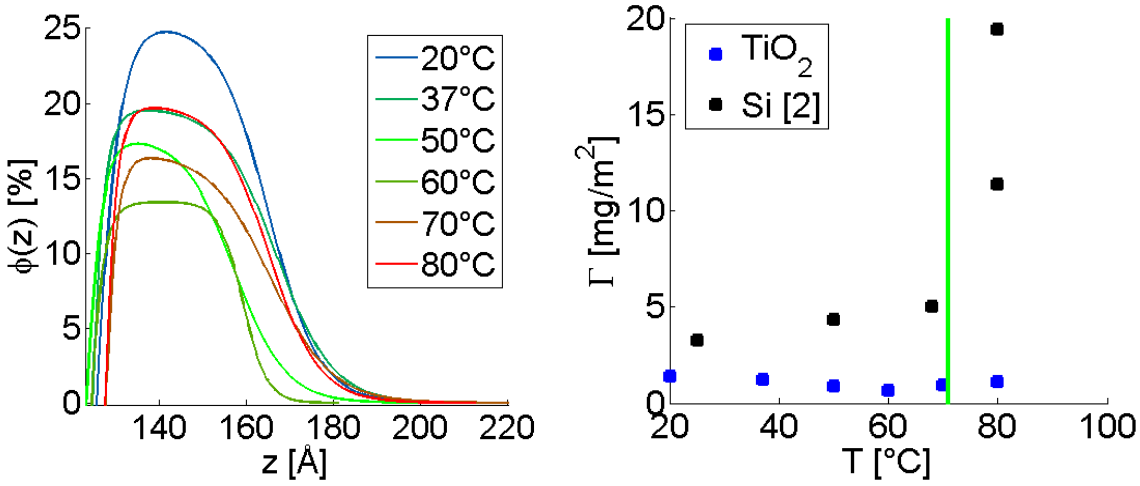

Figure 2: Volume fraction profiles as a function of temperature (left) and the comparison of the adsorbed amount of lysozyme on SiO2 [2] and TiO2 surfaces.

Figure 2 shows on the left side the surface coverage as a function of the layer height. For increasing temperatures up to 60°C the surface coverage decreases from 24.75 % to 13.40 % and increases again to 19.68 % for further rising temperatures. This behavior is contrary to measurements on SiO_2 surfaces [2], where the surface coverage, and thus the adsorbed amount of lysozyme (see right side of figure 2) rises continuously with rising temperature. Especially above the denaturation temperature of lysozyme at 71°C on silicon surfaces a strong layer growth occurs. This effect can't be observed by our measurements on TiO_2. One reason for that result could be that SiO_2 has a stronger negatively charged surface at a pH-value of 7 than TiO_2 and thus the positively charged lysozyme adsorbs more likely on SiO_2. For this reason a further experiments are planned, where we measure the adsorption of lysozyme on TiO_2 as a function of the pH-value.

Acknowledgment:

The authors thank the DELTA machine group for providing synchrotron radiation. This work was supported by the Cluster of Excellence RESOLV (EXC 1069) funded by the Deutsche Forschungsgemeinschaft. PS acknowledges the DFG Forschergruppe 1979 for funding.

References:

[1] T. Brenner et al., J. Colloid Interface Sci., **374**, 287–290 (2012).
[2] I. Kiesel et al., Langmuir **30**, 2077 (2014).
[3] C. Czeslik, Chem. Unserer Zeit, **40** (4), 238–245 (2006).
[4] P. S. Stewart and J. W. Costerton, Lancet **358** (9276), 135–138 (2001).

Tethered solid supported membranes with natural, deuterated lipids extracted from yeast

Irena Kiesel, Simon Wulle, Yuri Gerelli, Giovanna Fragneto
Institut Laue Langevin, Grenoble, France

Scientific Background

Transport processes through membranes are fundamental for the biological function of cells in living organisms. Until now, the transport mechanisms of e.g. drugs into cells are not fully understood. To investigate these processes, it is necessary to build a reproducible and stable model membrane system, accessible for analytical methods. Typically, model membranes are created as solid-supported lipid bilayers, as they are feasible for surface-sensitive techniques as X-ray- or neutron reflectivity. In order to allow the penetration of guest molecules through membranes, it is necessary to use a highly hydrated spacer between the lipid bilayer and the solid substrate. One approach to produce a substrate-separated lipid-bilayer was introduced by *Hertrich et al*. [1], using a polymer-lipid support on a silicon wafer. The chosen polymer cushion consist of a mixture of long and short polyethylenglycol (PEG) chains. The combination of different chain-lengths have shown to decrease the roughness of the polymer surface, allowing a high resolution investigation with reflectometry. Lipids attached at the end of the long PEG-chains serve as anchor for the formation of a lipid-bilayer.

The lipid bilayer was easily spread on this surface by spin coating and characterized by x-ray- and neutron reflectometry. *Hertrich et al.* prepared the lipid bilayer with SOPC (1-stearoyl-2-oleoyl-*sn*-glycero-3-phosphocholine), which has two carbon chains of which one is unsaturated. Natural membranes are composed by several different saturated and unsaturated lipid species. The purpose was to model a more natural mimicking membrane based on the use of natural lipid extracts obtained from *Pichia pastoris* yeast cells [2]. The availability of natural extracts in both hydrogenated and deuterated forms allowed the use of the so-called contrast variation method. This method is used in neutron reflectometry to increase the spatial resolution of the technique allowing a structural characterization at the Å length scale. The aim of this project was to create reproducible, stable and tethered model membranes with natural extracted lipids to mimic real membranes and to allow the investigation of transport processes through this membrane.

Experiment

The used substrates, PEG brushes on cleaned silicon single crystals (10x19 mm^2), were prepared by the protocol described by *Hertrich et al.* [1]. The quality, like roughness and coverage, were checked with atomic force microscopy. We have used two different kind of lipids: commercially available SOPC (Avanti Polar Lipids) and natural lipids extracted from *Pichia pastoris* yeast. The yeast was grown by the protocol of *de Ghellinck et al.* in normal hydrogenated medium (hYeast) or in deuterated medium in order to receive fully deuterated lipids (dYeast) [2]. These lipids were solved in organic solvent, SOPC in isopropanol and the natural lipids in a 2:1 mixture of chloroform and methanol. The concentration was 1.5 mg/mL. A few droplets of these lipid solutions were dropped onto the substrates for spincoating. The rotational speed was 12 rps for 5 s and 17 rps for 90 s. The coated substrates were freshly prepared and transferred into MilliQ water before each measurement. The reflectometry measurements were performed at beamline BL9 at DELTA with the 27 keV reflectometry setup [3].

Results and Discussion

The measured reflectivities shown in figure 1 are normalized to the Fresnel reflectivity R_F (theoretical reflectivity of a perfectly flat substrate) and shifted with respect to each other by a constant factor for clarity. The PEG-polymer brushes (grey) show nearly no differences compared to the bare silicon substrate (black dots) in water due to a nearly similar electron density of hydrated PEG and the surrounding water. Fringes become visible by adding lipids. Measurements of repeated preparations (1 and 2) with deuterated and hydrogenated natural lipids from yeast (blue and green, respectively) are similar within experimental errors. The fringes are enhanced for SOPC (red). The black lines are calculated reflectivities corresponding to the refined electron density profiles (EDP, figure 2). The EDPs consist of the silicon sub phase (Si), the natural silicon dioxide layer (SiO_2), a denser polymer layer close to the surface (PEG dense), a polymer layer with an electron density close to water (PEG) and the lipid bilayer (lipids). Including layers for lipid head groups does not improve the refinement. The sensitivity and resolution to highlight head groups can be decreased by roughness and a low contrast between head groups and water or PEG.

The resulting size of the bilayer fits well to the thickness of one bilayer. The difference in the reflectivities between SOPC and natural yeast lipids can be explained by a different electron density between the natural lipids and SOPC, probably due to a different packing density, and therefore a stronger contrast in the case of SOPC. The refinement for the SOPC reflectivity (red) for higher wave vector transfers q_z needs still to be improved. It could be that with spincoating not only one bilayer was formed but patches of a second bilayer were built. It will be checked in further analysis if the refinement could be improved by such a model.

In general, it was shown that bilayer with natural lipids are easily prepared with spincoating on polymer brushes and the experimental feasibility is comparable to the one for commercially available lipids.

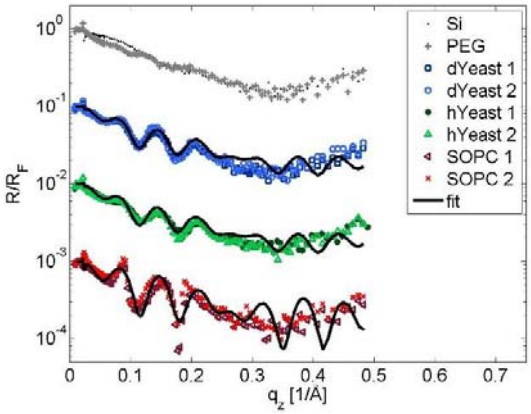

Figure 1 Fresnel normalized reflectivities shifted with respect to each other for clarity. Repeated measurements are freshly prepared samples.

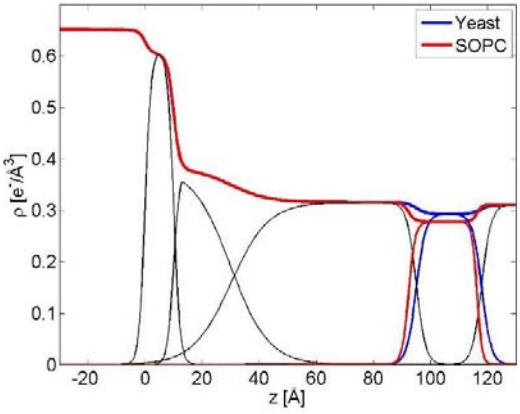

Figure 2 Electron density profiles corresponding to refinements of the reflectivities in fig. 1. The corresponding layer system is Si/SiO_2/PEG dense/PEG/lipids/water.

References

[1] Hertich et al., Langmuir 2014, 30, 9442−9447

[2] de Ghellinck et al., PLOSOne 2014, 9, 4, e92999

[3] Paulus et al., J. Synchrotron Rad. 2008, 15, 600-605

Acknowledgement:

We would like to thank the DELTA machine group for providing synchrotron radiation. Furthermore, we are thankful for support at beamline BL9 by P. Salmen, J. Nyrow, M. Paulus and C. Sternemann. We thank PSCM and NMI3 for travel funding.

The adsorption of soy proteins at the solid - liquid interface

Paul Salmen, Michael Paulus, Yury Forov, Patrick Degen, Julia Nase and Metin Tolan

Fakultät Physik/DELTA, TU Dortmund, 44221 Dortmund, Germany

The adsorption of denaturized or fragmented proteins is important for many applications in industry and biology. For example, it was found, that fat capsules with liquids inside are much more stable against dehydration when soy sauce is added in the liquid phase. In a previous beamtime at BI9 of DELTA, the behaviour of soy sauce and acid hydrolysed soy protein on hydrophobic silicon wafers has been investigated, see also our user report from 2014. In our current experiment, these were continued. We used the 27 keV x-ray reflectivity setup of BI9 and a cell for measurements at solid/liquid interfaces described in [1] at a temperature of 20 C°.

Reflectivity curves and electron density profiles of the interface between an octadecyltrichlorosilane(OTS)-coated silicon wafer and aqueous acid hydrolyzed soy protein solutions are shown in figure 1. The protein concentration was varied between 0.1 mg/ml and 25 mg/ml in a 1 mmol phosphate buffer solution. The measurements show a clear concentration dependence. For low concentrations of 0.1 mg/ml (red curve), the adsorbed layer consist of two sublayers. The first sublayer has an electron density of 0.394 $e^-/\text{Å}^3$, the layer on top has a much lower density of only 0.363 $e^-/\text{Å}^3$. The overall thickness is 17 Å. When the concentration is raised to 1 mg/ml (orange curve), thickness and electron density are constant for the whole layer (0.398 $e^-/\text{Å}^3$). For 10 mg/ml acid hydrolyzed soy protein (green curve), the layer thickness increases slightly and the electron density again is sligthly higher (0.408 $e^-/\text{Å}^3$). When the concentration is raised to 25 mg/ml (blue curve), the layer thickness rises to 25.5 Å while the electron density stays constant. It is important to note, that the size of the hydrophobic gap is doubled. The reason for this might be, that amino acids with low

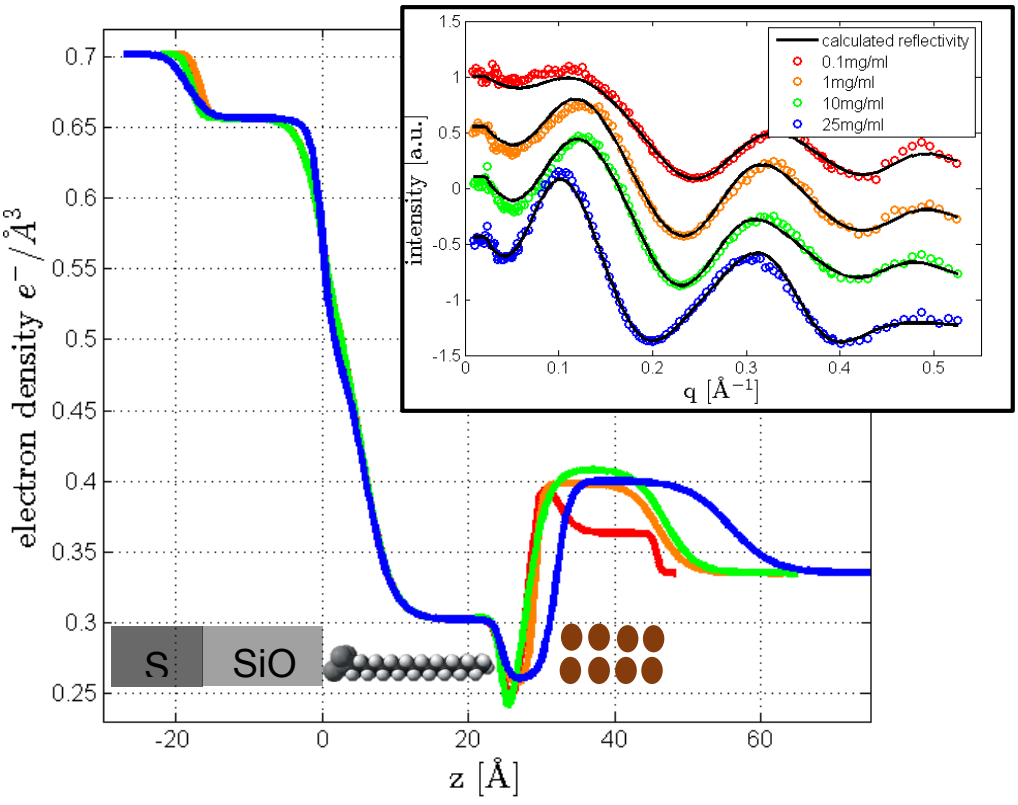

figure 1: Electron density profiles of OTS coated silicon samples. The inset shows the XRR-measurements divided by the Fresnel reflectivity of an ideally flat silicon surface and the corresponding fits.

electron density adsorb at the surface. In a different experiment, adsorption was also observed at the hydrophobic liquid/air interface. In this case, the adsorbed layers have an even higher electron density. Thus we conclude, that hydrophobic interactions are the driving forces for the adsorption. For a better understanding of the observed effects, a hydrophilic SiO_2 interface was investigated. The measurements and corresponding electron density profiles are shown in figure 2. As the silicon wafer in water (red curve) and in an acid hydrolyzed soy protein solution (blue curve) shows very similar results, it can be concluded that there is no adsorption at the hydrophilic interface. This confirms the assumption that hydrophobic interactions are the driving forces behind the observed effects.

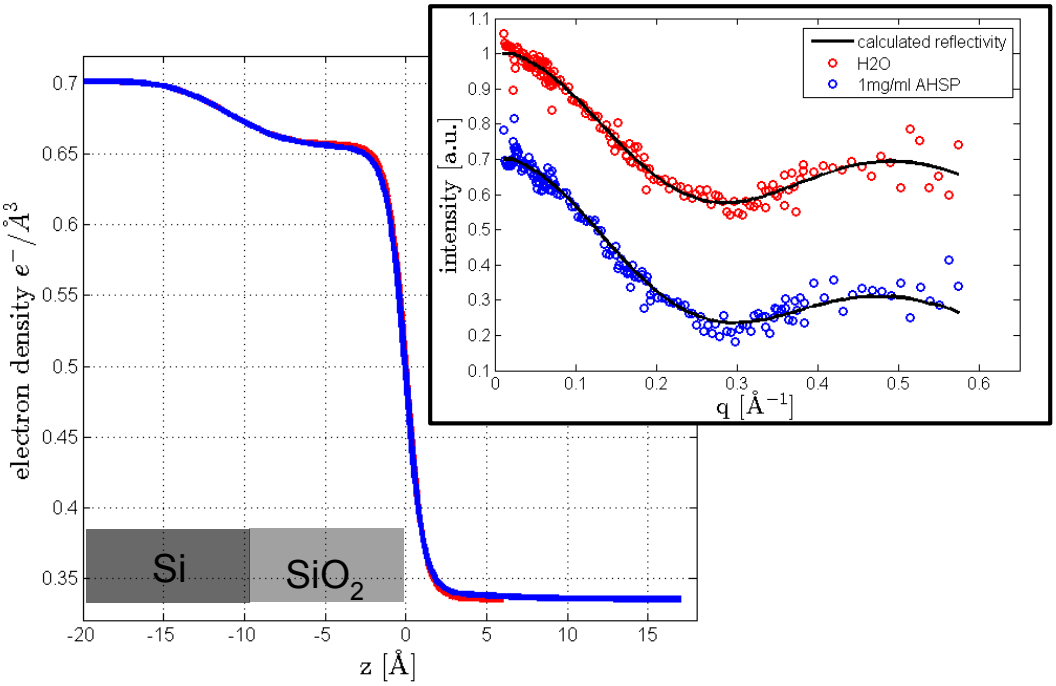

figure 2: Electron density profiles of a silicon with and without acid hydrolyzed soy protein in the liquid phase. The inset shows the XRR-measurements divided by the Fresnel reflectivity of an ideally flat silicon surface and the corresponding fits.

Acknowledgment

The authors thank the DELTA machine group for providing synchrotron radiation. This work was supported by the Cluster of Excellence RESOLV (EXC 1069) funded by the Deutsche Forschungsgemeinschaft. PS acknowledges the DFG Forschergruppe 1979 for funding.

[1] I. Kiesel, M. Paulus, J. Nase, S. Tiemeyer, C. Sternemann, K. Rüster, F.J. Wirkert, K. Mende, T. Büning, M. Tolan, *Temperature Driven adsorption and desorption of proteins at solid-liquid interfaces*, Langmuir **30** 2077-2083 (2014)

DELTA User report 2015
Proposer: Prof. Dr. A. Ludwig
Co-Proposers: F. Brüssing, S. Salomon, P. Decker

Structural characterization of a $[Fe_{57}Co_{43}/Au_{25}Cu_{75}]_{10}$ superlattice

F. Brüssing, V. Alexandrakis

Werkstoffe der Mikrotechnik, Institut für Werkstoffe, Fakultät Maschinenbau

Ruhr-Universität Bochum, D-44801 Bochum

$[Fe_{57}Co_{43}/Au_{25}Cu_{75}]_{10}$ superlattice structures were deposited via magnetron sputtering on MgO (001) single crystal substrates at a temperature of 200°C. 10 nm thick Cr (100) and a subsequently deposited 40 nm $Au_{25}Cu_{75}$ (001) spacer were used to enhance the epitaxial growth of the superlattice structures. The thickness of the Fe-Co layers in the different superlattice structures were 2, 5, 10 or 15 nm. All thin films were covered with a 3 nm Cr-layer for oxidation protection. A sketch of the sample design is shown in Figure 1b.

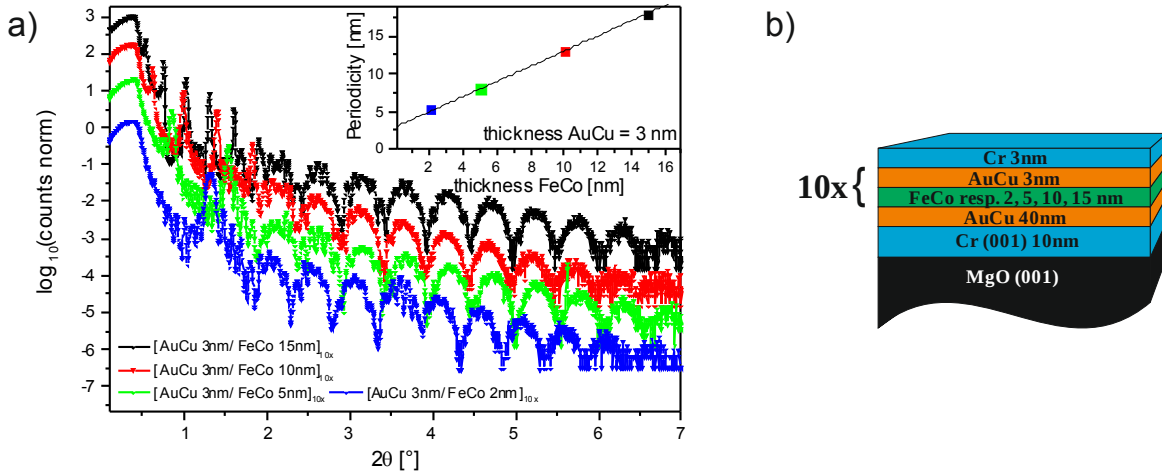

Figure 1: a) X-Ray reflectivity measurements performed at the DELTA Dortmund using a wavelength of 0.083 nm. The periodicity extracted from the superlattice peaks of the thin films is shown in the inset at the top right. b) Sketch of the thin film design.

X-ray measurements were performed to investigate the sample quality and the epitaxial relations of the layers. An X-ray source of high brilliance is indispensable for the investigation of the structural properties of such complex systems. Therefore, the synchrotron X-ray source DELTA (BL09) was used. Figure 1a shows the reflectivity measurements of the $[Fe_{57}Co_{43}/Au_{25}Cu_{75}]_{10}$ thin films at a wavelength of 0.083 nm. Well defined oscillations appear after the initial drop of intensity. These oscillations indicate a high quality of the layers and their interfaces. The periodic structure causes superlattice peaks to occur which are related to the periodicities of the thin films. In the inset of figure 1a the extracted periodicities are plotted in respect to the expected thickness of the $Fe_{57}Co_{43}$ layers revealing a linear relation and a thickness of the AuCu layers of about 3 nm.

The crystalline quality of the thin films perpendicular to the sample surface is revealed by an out-of-plane high angle radial scan at a wavelength of 0.062 nm, which is shown in Figure 2a. The sharp $Au_{25}Cu_{75}$ and Cr/FeCo peaks indicate a high crystal quality. The similar lattice parameters of 0.2885 nm for Cr and of 0.2857 nm for FeCo lead to an overlap of the Cr- and FeCo -peaks resulting in one peak at $2\theta = 24.92°$. For all samples the integrated intensity of the $Au_{25}Cu_{75}$ peak is in the same order, which is a result of the constant amount $Au_{25}Cu_{75}$ for the different samples. In comparison to this the integrated intensity of the Cr/FeCo peak is increasing with an increase of the periodicities. This is related to the increase of the $Fe_{57}Co_{43}$ layer thickness (2 nm, 5 nm, 10 nm, 15 nm). In between the $Au_{25}Cu_{75}$ and the $Fe_{57}Co_{43}$ peak a superlattice peak is visible representing the averaged lattice parameter of the layers within one periodicity. The position of this peak is shifting in respect to the different amounts of the $Au_{25}Cu_{75}$- and $Fe_{57}Co_{43}$-layers and their different lattice parameters.

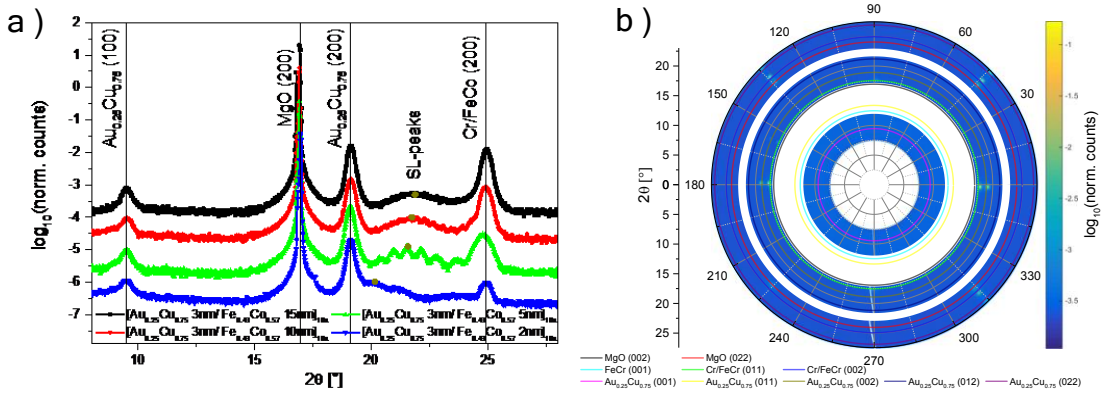

Figure 2: XRD measurements performed at the DELTA Dortmund using a wavelength of 0.062nm; a) out-of-plane and b) in-plane for the sample with the 15 nm thick FeCo layer

Furthermore, the in-plane structural correlation of the different layers was investigated via surface x-ray scattering techniques at glancing incident and exit angles. For this purpose the samples were rotated such that the scattering plane is close to parallel to the sample surface. Additionally, a line detector oriented parallel to the sample surface simultaneously measures the intensity for different in-plane Bragg peaks when the sample is rotated about its normal. To reveal the epitaxial relation of the layers the intensity distribution as a function of sample rotation by 360° is plotted in Fig. 2b. The positions of the MgO(002), MgO(022), FeCr(001), Cr\FeCr(011), Cr\FeCr(002), AuCu(001), AuCu(011), AuCu(002), AuCu(012), and AuCu(022) peaks are marked, revealing the epitaxial relation between Cr/FeCo, AuCu and MgO due to the coexistence of the Cr/FeCo(002), AuCu(022) and the MgO(022) peaks for one sample orientation and Cr/FeCo(011), AuCu(002) and the MgO(002) for an orientation rotated by 45° in respect to the other alignment.

A more detailed analysis of the in-plane peak position reveals a four-fold symmetry, indicating two equivalent in-plane axes with an angle of 90° in between. The corresponding lattice parameter for $Au_{25}Cu_{75}$ is about 0.385 nm for all samples. In case of $Fe_{57}Co_{43}$ it varies between 0.285 nm for 2 nm $Fe_{57}Co_{43}$ and 0.291 nm for 15 nm FeCo. These values, in combination with the values which can be extracted from the out-of-plane measurements, reveal the strain of the cubic lattice of the $Fe_{57}Co_{43}$- and $Au_{25}Cu_{75}$-layers. Identified was a constant tetragonal distortion of about 98% in case of the $Au_{25}Cu_{75}$-layers and a decreasing distortion from 102% to 99% in case of the $Fe_{57}Co_{43}$-layers between 2 nm and 15 nm thickness respectively.

DELTA User report 2015
Proposer: Prof. Dr. A. Ludwig
Co-Proposers: H. Stein, S. Salomon, P. Decker, A. Siegel, F. Brüssing

Investigation of phase regions in the materials system Ni-Co-Al

P. Decker

Werkstoffe der Mikrotechnik, Institut für Werkstoffe, Fakultät Maschinenbau

Ruhr-Universität Bochum, D-44801 Bochum

Ni-Co-Al alloys are of interest in high-temperature applications. A large variety of Ni-Al- or Co-Al-based superalloys exists. They are broadly used as turbine blade material for both power generation and aircraft turbines. A variety of binary phase diagrams for Ni-Co, Co-Al and Al-Ni as well as ternary Ni-Co-Al phase diagrams have already been established. The latter however cover only small parts of the ternary diagram. Some of them differ in the phase distributions. Therefore, it is necessary to gain valid information about the basic Ni-Co-Al materials system. This will be helpful for developing complex alloys including more than three elements.

To gain a better understanding of the phase formation in the Ni-Co-Al system, a materials library was deposited on a 4" Si/SiO_2 wafer via magnetron-sputtering. This materials library has a wide composition spread covering over 90% of the Ni-Co-Al materials system. A grid consisting of 342 measurement areas is used to define distinct measurement regions, with each area being 4.5 mm by 4.5 mm (fig. 1).

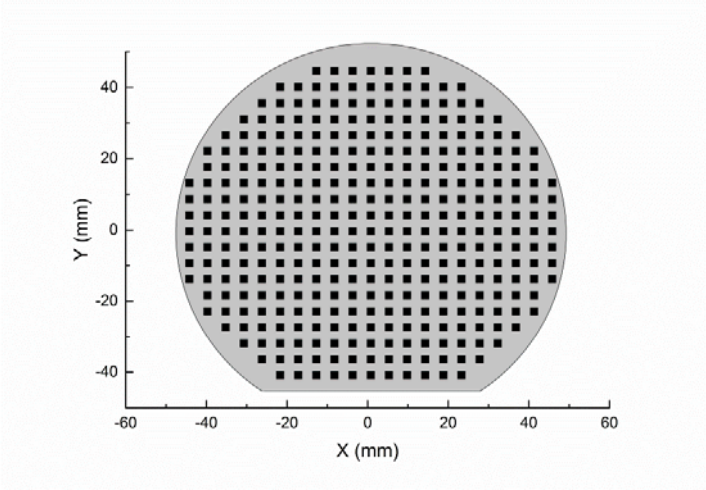

Figure 1: Visualization of the 342 point measurement grid on a 100 mm diameter wafer. The areas are defined by photolithographic processing.

The materials library was characterized by synchrotron XRD using a grazing incidence setup in combination with the mar345 detector at BL9. Because the thin film peeled off in some parts of the materials library prior to the beam time, a fraction of the materials library could not be measured. For the

measurements, a beam energy of 20 keV with a wavelength of 0.06199 nm was chosen. Pairing a macro-based control of the system and a translation stage with a large movement range allowed a high-throughput characterization of the materials library. A cluster analysis using the XRDsuite software developed in the group of Prof. I. Takeuchi, University of Maryland, was performed on the resulting diffraction data. It shows that the materials library consists of 19 different groups consisting of up to three different phases (fig. 2). The pure Ni and the pure Co phase were not detected in the preliminary XRD measurements performed in Bochum due to their weak signals. However, the excellent signal-to-noise ratio of the synchrotron allows the detection of such small signals.

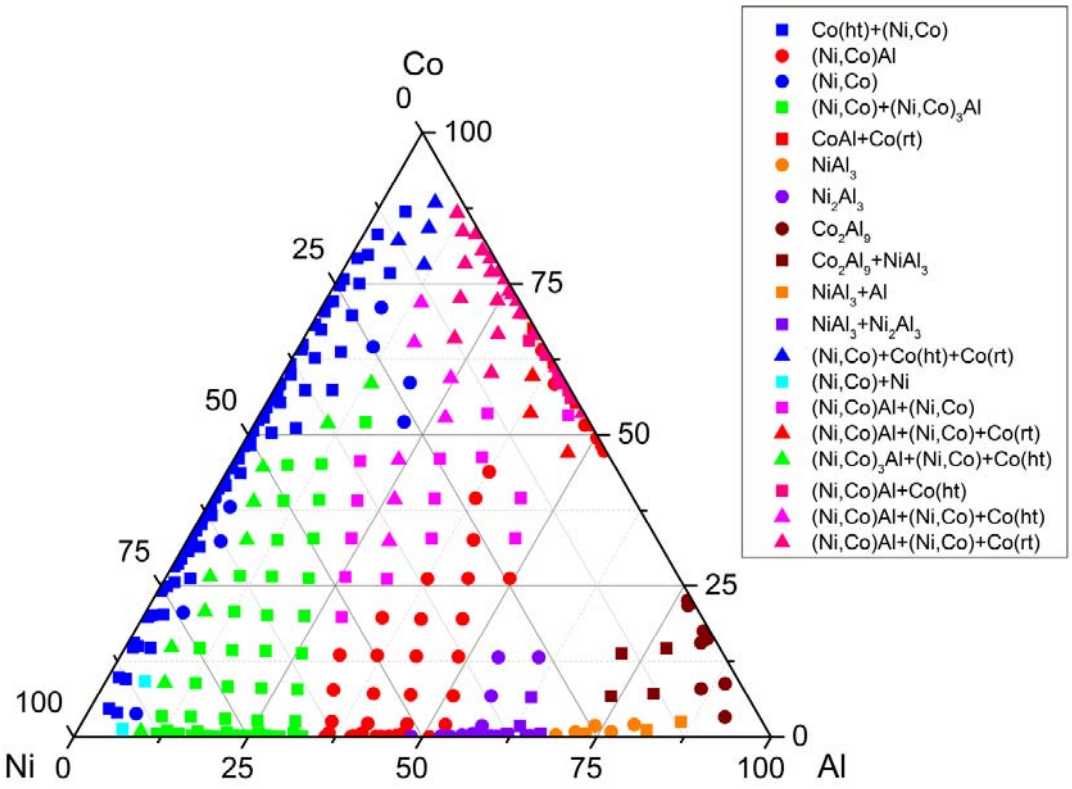

Figure 2: Cluster analysis of the Ni-Co-Al materials library as derived from the high-throughput XRD measurements performed at BL09.

Fig. 3 includes several radially integrated diffraction patterns as a plot of intensity over the diffraction angle. It shows the appearance and disappearance of several phases along an Al gradient with a constant Co content. By investigating the materials library in a high-throughput manner with the excellent signal-to-noise ratio provided, exact boundaries of the phase regions could be determined. Using this data more accurate Ni-Co-Al phase diagrams will be derived.

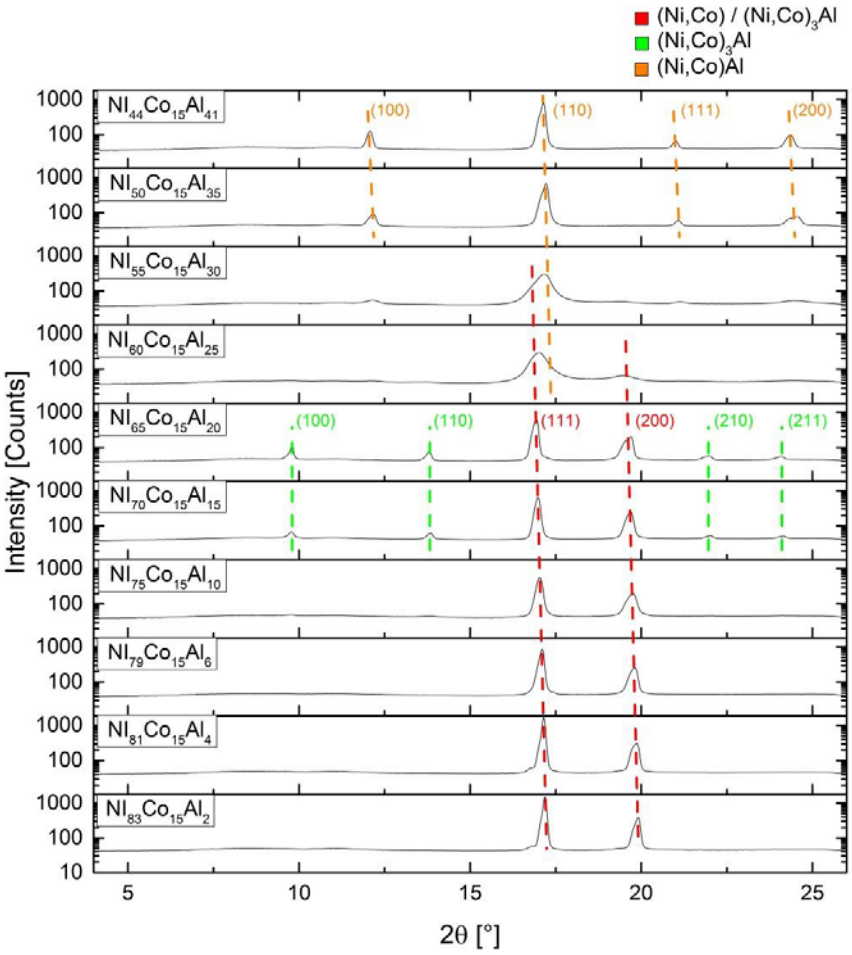

Figure 3: The appearance and disappearance of phases along the Al gradient for a constant Co content.

Thermal induced lattice distortion of diluted magnetic semiconductors

H. Göhring, M. Paulus, T. Büning, C. Sternemann, S. Bieder, K. Esch, H. Rahmann,

C. Schröder, M. Bayer, M. Tolan

Fakultät Physik/DELTA, Technische Universität Dortmund, 44221, Germany

Diluted magnetic semiconductors which combine the properties of semiconductors and ferromagnets have been an important subject in materials science. Semiconductors with Curie temperatures above room temperature could revolutionize the field of spintronics by allowing control of the magnetization via application of voltage as observed e.g. for the ferromagnetic material galfenol [1]. Magnetic semiconductors, which are currently under investigation, still show a rather low Curie temperature making them inapplicable for technical use. However, GaMnAs seems to be a promising candidate for high Curie temperature material. GaMnAs is typically grown epitaxially on GaAs substrates with a limited manganese content of a few percent, as higher Mn contents cause the formation of Mn nanocrystals. This system was studied intensively in the past years. Starting at Curie temperatures of around 60 K, special hybrid systems containing GaMnAs show ferromagnetic behaviour up to temperatures of 200 K [2]. A detailed knowledge about the interrelation between structural properties and magnetism is still not existing for these systems.

To overcome this lack of knowledge high resolution x-ray diffraction experiments were performed at beamline BL9 of DELTA using a photon energy of 15 keV and a helium flow cryostat setup. In order to minimize vibrations due to the transfer tube the cryostat is connected to the diffractometer using ball bearings which ensure an excellent steadiness on the one hand and still allow sample movement along the z-axis on the other. Figure 1 shows a photo taken of the experimental setup. A PILATUS 100K detector was used for data acquisition. Two samples with Curie temperatures of 60 K and 120 K were investigated. The goal of our experiment was to detect structural changes due to magnetostriction passing the Curie temperature. The small changes in the GaMnAs lattice were determined by measuring both, the GaAsMn (004) and the GaAs(004) reflection of the substrate which serves as an internal reference. The measurements were carried out over a temperature range from 80 K to 160 K not

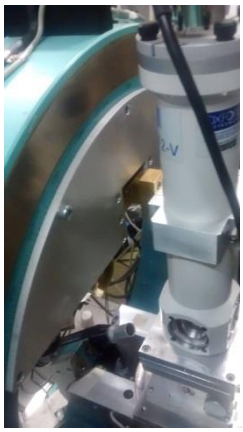

Figure 1: The cryostat is mounted on a Huber Z-stage and connected to the diffractometer via ball bearings to minimize vibrations to the system.

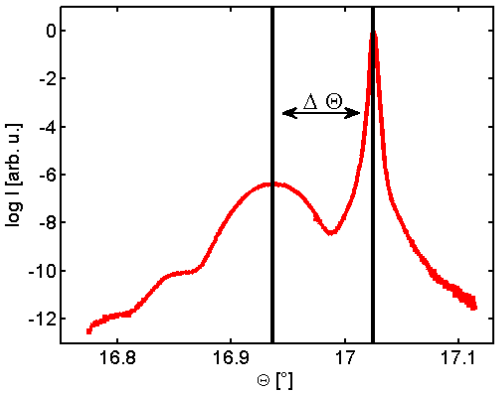

Figure 2: Measured (004) Bragg rod of the 120 K sample. The relative changes between the GaAs substrate and GaMnAs layer Δθ are investigated.

reaching the Curie temperature of the control sample. Figure 2 shows a Bragg rod taken with the 120 K sample.

To investigate the structural changes due to magnetostriction, the thermal effect on the lattice has to be separated. The separation can be achieved in a first step of the data analysis by determining the relative changes Δθ between the GaAs and GaMnAs (004) Bragg peak positions.

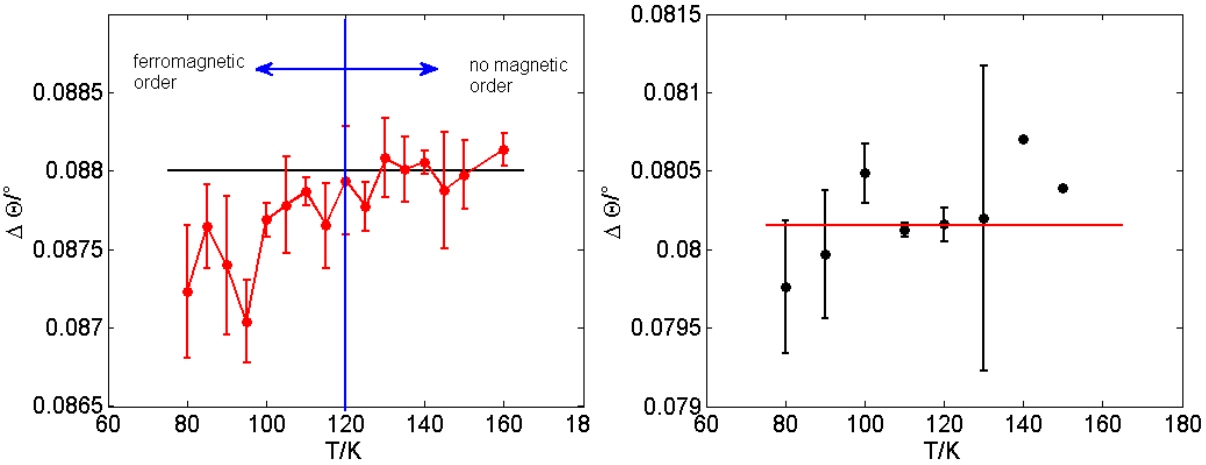

Figure 3: The angular separation Δθ between the GaAs and the GaMnAs (004) Bragg reflection. Red and black points represent the experimental data corresponding to the 120 K and 60 K control wafer, respectively. The blue line marks the Curie temperature while the black and red lines serve as a guide to the eye.

The data presented in figure 3 shows the averaged angular separation Δθ for the Wafer with a curie temperature of 120 K on the left and the control wafer with a 60 K on the right in red and black points, respectively. The black and red lines serve as a guide to the eye. The red data indicate that Δθ remains roughly constant above and decreases below the Curie temperature which hints on an impact of the ferromagnetic order on the GaMnAs lattice. For the control wafer one expects that Δθ remains constant along the whole temperature range because the Curie temperature was not reached. For a final conclusion more data has to be taken and a final analysis needs to be made.

Reference:

[1] D. E. Parkes, S. A. Cavill, A. T. Hindmarch, P. Wadley, F. McGee, C. R. Staddon, K. W. Edmonds, R. P. Campion, B. L. Gallagher and A. W. Rushforth, *Non-volatile voltage control of magnetization and magnetic domain walls in magnetostrictive epitaxial thin films*, Appl. Phys. Lett. **101**, 072402 (2012).

[2] A. M. Nazmul, T. Amemiya, Y. Shuto, S. Sugahara and M. Tanaka, *High temperature ferromagnetism in GaAs-based heterostructures with Mn delta doping*, Phys. Rev. Lett. **95**, 017201 (2005).

Acknowledgement

We would like to thank the DELTA machine group for providing synchrotron radiation and technical support. We thank Xinyu Liu for preparing and providing the samples. Holger Göhring acknowledges the support by BMBF through grant no. 05K12PE1 and the DFG through TRR160. Thomas Büning is funded by the BMBF within the FSP-302 with grant no. 05K13PE2 and Mercur AN-2014-0036. Karin Esch would like to thank DFG (TO 169/17-1) for financial support.

Investigation of phase formation

in HVOF sprayed and remelted NiCrBSiFe Coatings

Wolfgang Tillmann, Leif Hagen, Dominic Stangier
Institute of Materials Engineering, Technische Universität Dortmund

Introduction

The tribological behavior of NiCrBSi coatings, conducted by laser or flame assisted remelting processes have been investigated in different studies [1-5]. Miguel et al. [4] investigated the tribological behavior of these coating systems, obtained with different thermal spray processes and post-heat treated procedures. It was reported that the sprayed and fused coatings obtain the best sliding wear resistance. In contrast to that, ball-on-disc tests of NiCrBSiFe coatings reveal an enhanced wear resistance for HVOF (High Velocity Oxy Fuel) sprayed samples (AS) compared to HVOF sprayed and laser remelted specimen (LM) (**Fig.1**, left side) as shown by a reduced wear coefficient k.

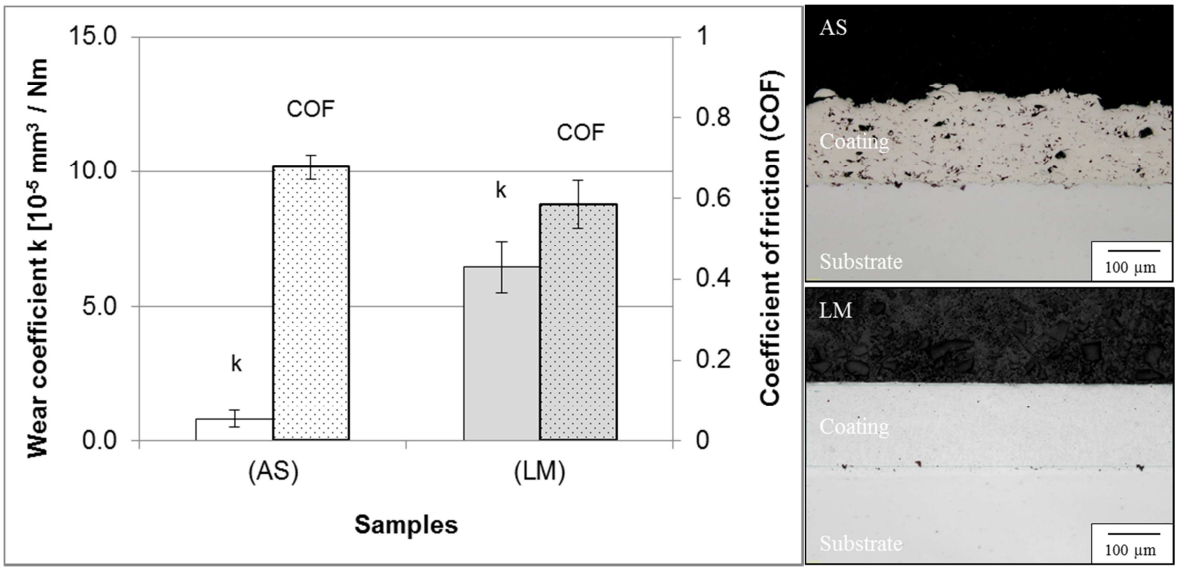

Fig. 1: Tribological behavior of different samples (left); Cross-section images showing the microstructure of different specimens (right): (AS) as-sprayed and (LM) sprayed and laser remelted

Since the addition of iron to the feedstock material can lead to different phase evolution during spraying and remelting, x-ray analyses and metallographic observation of the NiCrBSiFe coating were conducted.

Experimental

Cross-section images of the microstructure of the coating were taken using a field emission scanning electron microscope (FE-SEM) with backscattered electron detectors type JSM-7001F (Fa. Jeol, Germany). Regarding the determination of coating characteristics, nanoindentation tests (Fa. Agilent Technologies, California) were carried out on the surface in order to analyze the hardness and Young's modulus. The phase evolution in the coating after the deposition and remelting process was analyzed via X-ray diffraction (XRD) at beamline BL9 of the synchrotron light source DELTA. The photon energy was 15 keV (wavelength λ= 0.826 Å). To detect the scattered intensity, a PILATUS 100k detector was used.

Results

Experiments using nanoindentation reveal an average hardness of 10.1 ± 1.5 GPa and a Young's modulus of 261.7 ± 12.8 GPa for the laser remelted layer (LM), whereas the coating under as-sprayed and polished conditions (AS) possesses an average hardness of 11.3 ± 2.0 GPa and a Young's modulus of 194.6 ± 23.4 GPa. Due to the relation between the mechanical response of the coating and the H / E ratio [6], moreover, as demonstrated in [7] the resistance to plastic deformation, the H^3/E^2 ratio is a significant factor governing sliding wear behavior. Thus, high H^3/E^2 ratios provide increased resistances to erosion. For sample (AS) the H / E ratio is about 0.058 (H^3/E^2 = 0.038), whereas the remelted sample (LM) provides a value of 0.039 for the H / E ratio (H^3/E^2 = 0.015). Based on this interrelationship it is obvious that sample (AS) have a slightly better wear resistant behavior as shown in Fig. 1. Regarding the nanoindentation experiments, sample (LM) exhibits significant deviations of the measured values increasing to more than 20 GPa. As reported in the literature, the hardness values for CrB ranges from 21.1 ± 0.9 to 22.4 ±1.7 GPa [8]. EDX analyses show the evidence of Cr-rich precipitations, which are heterogeneously distributed in the melted layer (**Fig. 2** (right), dark grey areas).

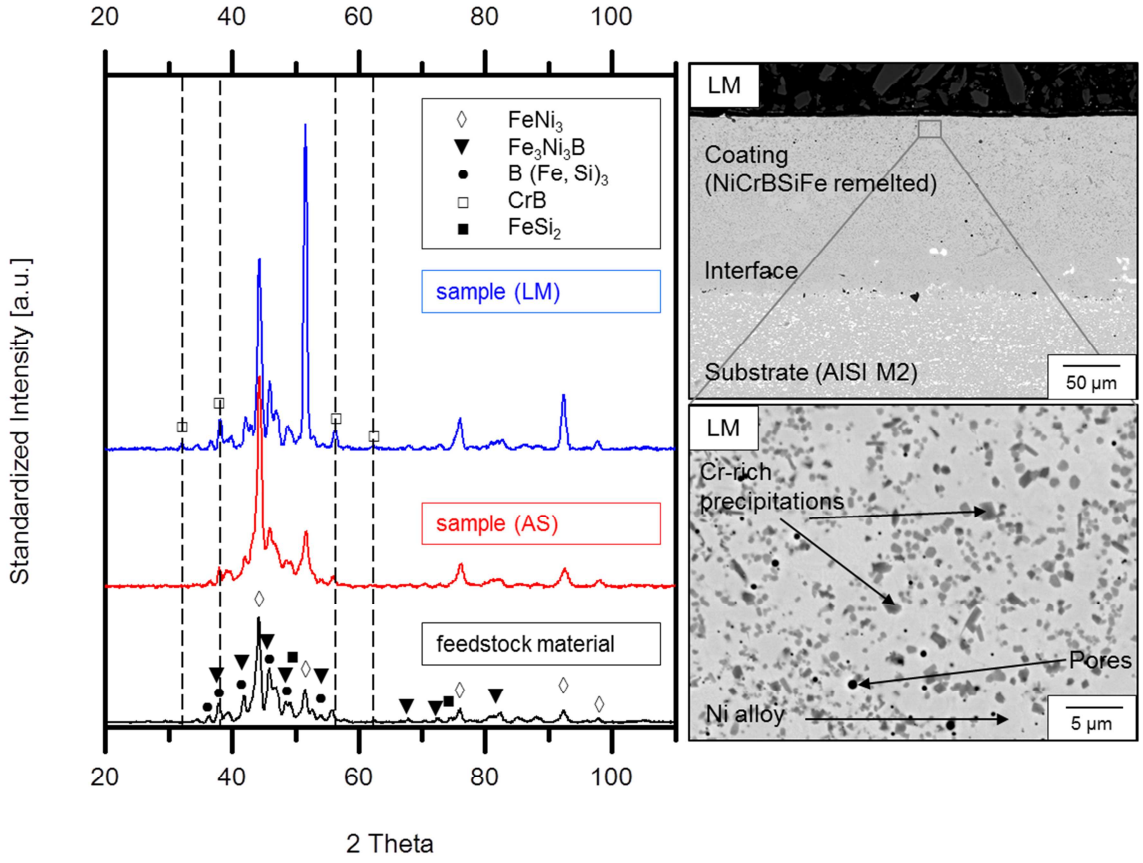

Fig. 2: XRD pattern for different samples, showing the results for the feedstock material, the coating under as-sprayed conditions, and the laser remelted sample (left); SEM images showing the cross-section of the laser remelted NiCrBiSiFe coating bonded to the substrate, and a solid solution of Cr-rich precipitations in the surrounded Ni matrix (right)

In terms of XRD analyses, the NiCrBSiFe powder (80.15.1, Fa. GTV, Germany) mainly consists of a mixture of $FeNi_3$, Fe_3Ni_3B and $B(Fe,Si)_3$ phases. Comparing these results with the ones of the sample (AS), it is revealed that most of the powder phases are also present in the thermally sprayed coatings, see **Fig. 2**. The XRD pattern for the sample (AS) shows a similar phase evolution, containing a reduced amount of Fe_3Ni_3B and an increase of bimetallic $FeNi_3$ phase. In terms of laser remelted

samples (LM), the XRD analyses reveal that the coating is composed of $FeNi_3$, Fe_3Ni_3B, $B(Fe,Si)_3$ and $FeSi_2$, whereby it possesses mainly $FeNi_3$. In addition, CrB is detected as found here in the diffraction pattern. The change of the scattering intensity observed around 51.5° and 92.2° for the remelted representative sample, the position of $FeNi_3$ (200) and (311) Bragg reflection, can be explained by the crystal growth due to laser remelting as seen in the diffraction image.

Acknowledgement

The authors gratefully acknowledge the financial support of the German Research Foundation (DFG) within the Transregional Collaborative Research Center SFB/TR73 subproject B5. The authors acknowledge the DELTA machine group for providing the synchrotron radiation and technical support.

References

1. E. Fernández et al., Wear 259 (2005) 870-875.
2. R. González et al., Wear 262 (2007) 301-307.
3. N. Serres et al., Wear 270 (2011) 640-649.
4. J.M. Miguel et al., Tribol. Int. 36 (2003) 181-187.
5. C. Navas et al. Surf. Coat. Technol. 200 (2006) 6854-6862.
6. J. Musil et al. Surf. Coat. Technol. 154 (2002) 304-313.
7. F. Cai et al. Wear 324–325 (2015) 27-35.
8. S. Okada et al., J. Cryst. Growth 166 (1996) 429-435.

The Detachment Behavior of Polycarbonate on Thin Films above the Glass Transition Temperature

W. Tillmann[1], L. Hagen[1], F. Hoffmann[1], M. Dildrop[1] A. Wibbeke[2], V. Schöppner[2], M. Pohl[2], C. Krumm[3], J. C. Tiller[3], M. Paulus[4], C. Sternemann[4]

[1]*Technical University of Dortmund, Institute of Materials Engineering, Germany*
[2]*University of Paderborn, Polymer Engineering Paderborn - Polymer Engineering, Germany*
[3]*Technical University of Dortmund, Chair of Biomaterials and Polymer Science, Germany*
[4]*Technical University of Dortmund, Fakultät Physik / DELTA, Germany*

Introduction

For the mono-axial stretching of amorphous polycarbonate films, the process parameters settings, as their affect the orientation degree of the stretched polycarbonate films, are significant factors which influence the quality of these films. Due to the mono-axial stretching process of polycarbonate, the molecular chains are highly-oriented, thus enabling to use their high covalent binding forces for strengthening [1]. An anisotropy, which significantly increases mechanical characteristic values, such as the stiffness and strength [2], when compared to injection molded base material [3, 4], is generated because of this specific orientation of molecules. The introduced self-reinforcement is, among other things, dependent on the temperature control [3]. Since an unfavorable adhesion of the films on the stretching rolls was observed especially at higher temperatures, suitable coatings may affect the detachment behavior of polycarbonate on functional surfaces.

For this purpose, Cr/CrAlN [5, 6], WC/CoCr and hydrogen-doted DLC (a-C:H, diamond like carbon) [7] coatings have been developed and produced in order to examine the pull-off forces of the polycarbonate film in dependence on the temperature and contact time. A model, which reconstructs the process of the contact of the film on the heated surface of the rolls, was produced to measure the pull-off force of Makrolon® 3105. The Cr/CrAlN was determined to be the most suitable coating for a mono-axial stretching unit as this coating reduces the adhesion of Makrolon® 3105. In contrast to the results obtained by the Cr/CrAlN and WC/CoCr coatings, the highest pull-off force occurs when the DLC coating become in contact with the Makrolon® 3105. Here, the adhesion tendency significantly increases at temperatures above the glass transition temperature of Makrolon® 3105 which is 149°C as determined by differential scanning calorimetry measurement.

Experimental

The temperature dependent phase behavior of the three coating was analyzed via x-ray diffraction (XRD) at beamline BL9 of the synchrotron light source DELTA. The photon energy was 15 keV (wavelength λ= 0.826 Å), for the detection of the scattered intensity a PILATUS 100k detector was used. The angle of incidence was 0.5°. The sample surface temperature was steered by an Oxford cryojet system between room temperature and 500 K. In addition, surface energies of the coatings were calculated using the Owens, Wendt, Rabel and Kaelble (OWRK) method by measuring the static contact angle of different polarity liquids on a given sample. Seven different liquids having different polarity were used as probes for surface free energy calculations: Water, Diiodomethane, Thiodiglycol, Ethylene glycol, 1-Oktanol, Trichloromethane and Dimethylformamide.

Results

The WC/CoCr coating exhibits strong WC Bragg reflections and some weak contributions of Co_3W_3C and W_2C as indicated in **Fig. 1** top. The phase composition is stable over the entire temperature range. Also, the Cr/CrAlN coating shows no phase changes with rising temperature (**Fig. 1** middle). However, the DLC layer behaves differently. The diffraction data show two different contributions. Three broad Bragg reflections can be identified, which can be attributed to the underlying CrN layer. As the DLC layer is in an amorphous state, only a broad intensity distribution covering the whole scanning range is expected. This is observed by a strong background, which decrease with increasing scattering angle. However, changing the temperature yields a change of this intensity distribution as indicated in **Fig. 1** bottom. While the scattering intensity drops down at higher scattering angles an intensity increase is observed around 14°, the position of the graphite (002) Bragg reflection. Hence, a temperature induced formation of sp^2 coordinated carbon is suggested.

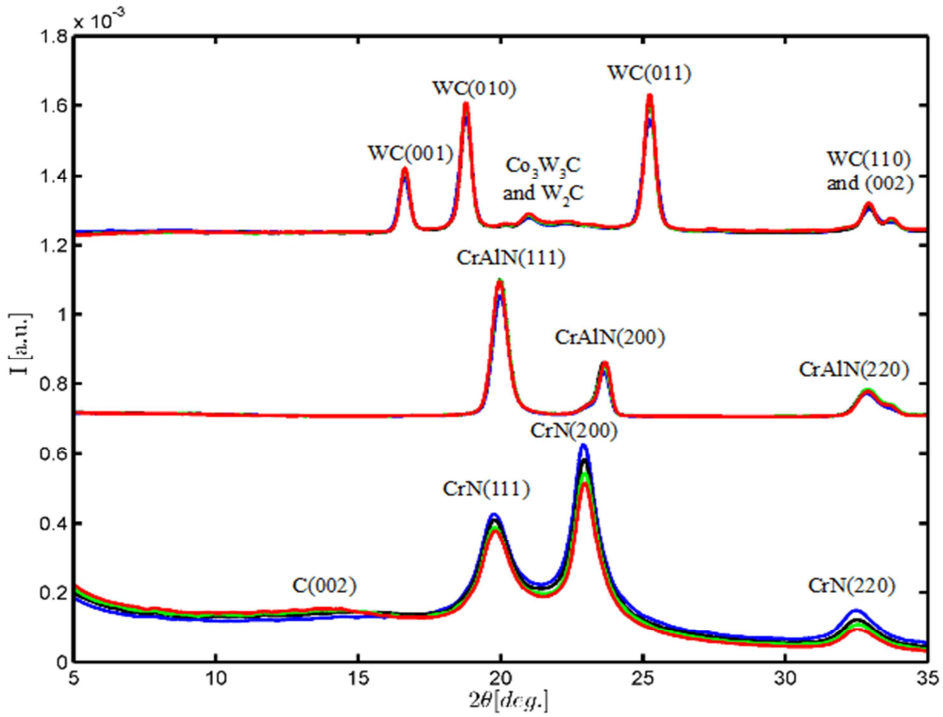

Fig. 1: XRD pattern show the phase evolution of the different coatings for different processing temperatures in a range from room temperature to a temperature of 220°C.

The OWRK method was used to estimate the surface energy of the coatings by measuring the static contact angle of different polarity liquids on a given sample (see **Table 1**).

Tab. 1: Surface energy calculations by OWRK for different coating systems. In addition to the total surface energy (SE_{Total}), split into the dispersive component ($\sigma_{s,d}$) and the polar fraction ($\sigma_{s,p}$), the regression coefficient (RQ) and its standard deviation (s_{Chi}) are determined.

Coating	SE_{Total} [mN / m]	$\sigma_{s,d}$ [mN / m]	$\sigma_{s,p}$ [mN / m]	RQ	s_{Chi}
a-C:H	48.825	31.243	17.585	0.879	6.337
a-C:$H_{220°C}$	62.386	50.490	11.896	0.900	1.690
WC/CoCr	51.615	28.643	22.973	0.848	9.254
Cr/CrAlN	42.162	30.786	11.376	0.830	4.498

In comparison to the other samples, the Cr/CrAlN coating has the lowest value for the total surface energy and polar fraction. According to this, Cr/CrAlN coating possesses the lowest energy needed to detach a medium from the surface. The surface energy of the Cr/CrAlN surface revealed the lowest surface energy, which could be expected from pull-off force measurements in the preliminary tests. The samples with the DLC coating showed more complicated results. In preliminary tests it showed the highest pull off force. This is in contrast to the obtained surface energy of 48.825 mN / m, which is lower as the surface energy of the WC/CoCr sample (SE_{Total} = 51.615 mN / m), although it has a significant higher pull off force at elevated temperatures. X-ray measurements showed, that the DLC coating altered during the thermal treatment. The investigations on the phase evolution of the DLC coating during a change in temperature (up to 220℃) reveal the formation of sp^2 coordinated carbon. Repeated measurements (in-situ) going down to reduced temperatures (220℃ → 185℃ → 150℃ to RT) give the fact that the formation of sp^2 coordinated carbon is irreversible. Because of this the estimation of the surface energy of the heat treated DLC coating was done ex-situ. The values for the DLC coating after processing are shown in Table 1 as well. It is obvious that the heat treated DLC (a-C:$H_{220℃}$) coating shows an increase of the total surface energy, which is about 62.386 mN / m. According to this, DLC (a-C:$H_{220℃}$) coating possesses the highest energy.

Acknowledgements

This paper is based on investigations carried out in the collaborative research center CRC/TRR 30, subprojects A4 und A8, which is kindly supported by the German Research Foundation (DFG). We thank DELTA for providing synchrotron radiation.

References

1. A. Karbach, Wachstumsmechanismus von Eigenfasern, in: G. W. Ehrenstein, Kolloquium Technologie der Eigenverstärkung von Thermoplasten, Institut. für Werkstofftechnik, Kassel, Germany (1987). pp. 5-18
2. J. Klimke et al., Kunststoffe International, 92 (2002) 45-49
3. M. Sasse et al., Manufacture of self-strengthened polycarbonate by extrusion, Proceedings of the 27th World Congress of the Polymer Processing Society, Marrakech, Morocco (2011).
4. M. Sasse et al., Self-reinforcement of uniaxially stretched polycarbonate film, Proceedings of the 70th Annual Technical Conference of the Society of Plastics Engineers, Orlando (2012).
5. W. Tillmann et al., China Surface Engineering, 26 (2013) 3
6. W. Tillmann et al., Adhesion and tribological behavior of Cr/CrAlN multilayer coatings on thermally sprayed substrates for hot metal forming, in: H.-P. Heim, D. Biermann, J. Maier, Proceedings of the 1st Int'l Conference on Thermo-mechanically Graded Materials, Kassel, Wissenschaftliche Scripten, Auerbach (2012). pp. 11-18
7. W. Tillmann et al., Mater. Sci. Forum, 706–709 (2012) 2596-2601

DELTA User report 2015
Proposer: Prof. Dr. A. Ludwig

Phase identification in thin film materials via grazing incidence XRD

C. Khare, Y. Motemani, S. Salomon, A. Ludwig

Werkstoffe der Mikrotechnik, Institut für Werkstoffe, Fakultät Maschinenbau

Ruhr-Universität Bochum, D-44801 Bochum

During last year's beam times at BL09 several thin film materials were investigated. For some materials the investigation focused on the identification of occurring phases without the need of a cluster analysis on full materials libraries. These were investigated as either defined areas on materials libraries or separate thin films on chips. The measurements were performed with a beam energy of 20 keV in a grazing incidence geometry using the mar345 area detector. In combination with the excellent signal-to-noise ratio provided at BL09 this setup is ideal for the investigation of the phases present in thin films. Amongst others, materials with interesting magnetocaloric, solar water splitting, energy storage and shape memory properties were investigated. In the following two exemplary experiments are presented.

Identification of phases in Ti-W-Fe-O samples annealed at different temperatures

C. Khare

A specific composition investigated on a Ti-W-Fe-O materials library demonstrated promising photoelectrochemical (PEC) solar water splitting characteristics. Therefore, homogeneous Ti-W-Fe-O samples, annealed at 600°C and 700°C, were analyzed at BL09 for the identification of phases, as the XRD measurements in Bragg-Brentano geometry with a lab diffractometer were not conclusive.

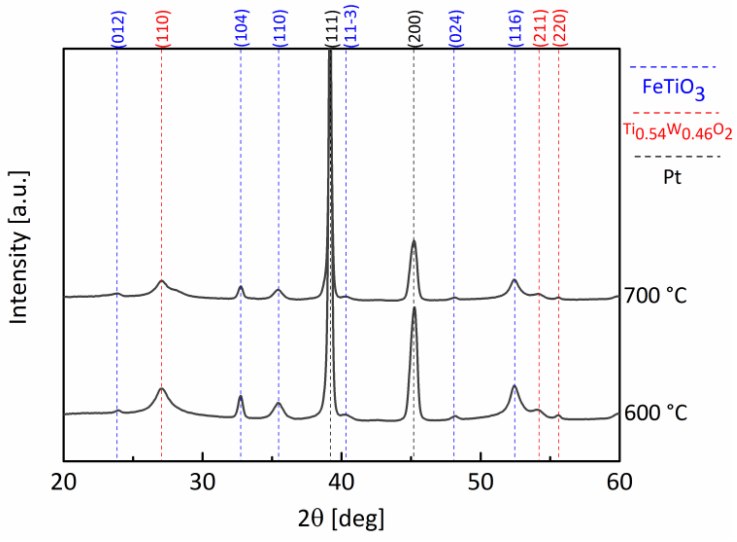

Figure 1: Synchrotron X-ray diffraction patterns of homogeneous Ti-W-Fe-O films annealed at 600°C and 700°C.

The synchrotron XRD measurements demonstrated that the film contains a mixture of two phases: $FeTiO_3$ and $Ti_{0.54}W_{0.46}O_2$ (Pt is used as a back contact for PEC measurements). The investigated homogeneous samples also demonstrated the promising electrochemical properties that were observed in the specific measurement region on the materials library. This phase analysis enabled further assessment of the original materials library. On the materials library, since the films are highly textured and as the peak intensities are low, the use of conventional XRD measurements (Bragg-Brentano geometry) for phase identification was insufficient. However, it was found that the combination of both XRD measurements, Bragg-Brentano geometry for overall mapping and synchrotron for further in-depth analysis presented a reliable way to identify the phases of interest on the materials library.

Phases in multifunctional Ti-Ta-O nanocolumnar thin films

Y. Motemani and C. Khare

Multifunctional Ti-Ta-O samples were chosen for in-depth phase identification. The investigated compositions demonstrated promising applications in Li-ion batteries and in solar water splitting (both as an anode material). Synchrotron XRD analysis enabled the distinction of the occurring phases and the correlation of those with the electrochemical properties of the thin films. Based on the XRD analysis, both of the compositions are mixtures of rutile (TiO_2) and $Ti_{0.8}Ta_{0.2}O_2$ phases. The intensity of the peaks of the rutile phase is higher for $Ti_{80}Ta_{20}$. As this sample contains higher amounts of Ti, formation of more TiO_2 is expected. A higher volume fraction of the rutile phase in the Ti-rich sample could be a plausible reason that the $Ti_{80}Ta_{20}$ sample did not show the expected electrochemical performance in battery applications (as the rutile phase is not an active phase from the electrochemistry perspective). On the other hand, a better electrochemical performance of $Ti_{70}Ta_{30}$ sample could be attributed to the lower volume fraction of TiO_2 and a dominating $Ti_{0.8}Ta_{0.2}O_2$ phase.

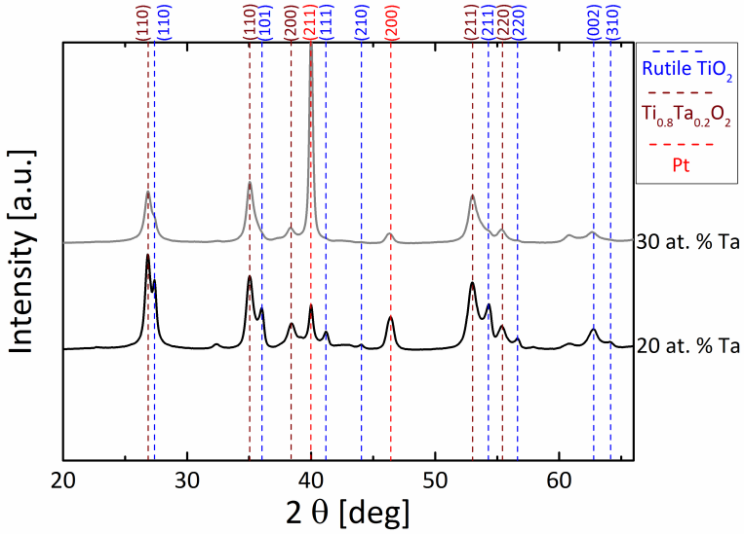

Figure 2: Synchrotron X-ray diffraction patterns of homogeneous Ti-Ta-O films.

DELTA User report 2015
Proposer: Prof. Dr. A. Ludwig
Co-Proposers: H. Stein, S. Salomon, P. Decker, A. Siegel, F. Brüssing

High-throughput XRD based phase mapping in Cu-Si-Ti-O and in-depth crystallographic investigation of Al-Cr-Fe-O photocathodes for solar water splitting

H. Stein

Werkstoffe der Mikrotechnik, Institut für Werkstoffe, Fakultät Maschinenbau

Ruhr-Universität Bochum, D-44801 Bochum

For the design of tandem solar absorbers in oxide photoelectrochemical and photovoltaic absorber systems stable, intermediate bandgap, p-type absorbers are needed. During the recent beam time new materials found by combinatorial materials science from the systems Cu-Si-Ti-O and Al-Cr-Fe-O were investigated for occurring phases in these multinary metal oxide materials libraries. In the Al-Cr-Fe-O system a new absorber material based on Al:Cr_2FeO_4 was identified [1]. This material exhibits an outstanding photovoltage of 1 V, promising photocurrents and a bandgap of 1.5 eV. Due to the limited resolution of our in-house XRD system, it was not possible to assign a spinel or corundum type structure to the identified p-type material. Using the translation stage at BL09 we were able to investigate the crystallographic changes across the Al-Cr-Fe-O materials library when going from the p- to the n-type compositions with a well-defined line scan. The identified subtle changes in crystal structure and how they influence the semiconducting behavior are currently under evaluation. With the help of TEM diffraction and complementary XRD results during this beam time, we were finally able to identify the crystal structure of Al:Cr_2FeO_4 that exhibits p-type semiconducting properties. In Figure 1 a 2D synchrotron-XRD pattern is

shown, with the Cr_2FeO_4 peaks marked. These findings will help us to further develop and understand the material's properties and aid theoreticians to perform quantum mechanical calculations.

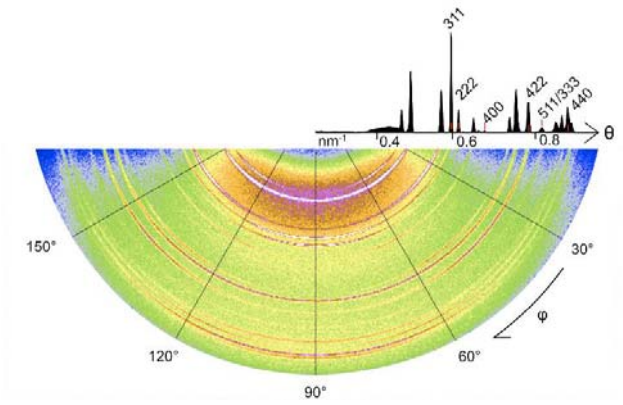

***Figure 1**: 2D Synchrotron XRD diffraction image (bottom) with φ integration with relevant Cr_2FeO_4 peaks marked*

To address the thermodynamic instability of Cu_2O by alloying with third elements, a combinatorial study in the system Cu-Si-Ti-O was performed. Two new p-type materials based on Si:Cu_3TiO_x and Ti:$CuSiO_3$ (dioptase) were found to show promising photoelectrochemical properties. Without a co-catalyst, photocurrents of up to 430 μA/cm^2 at 416 mV vs. RHE were observed under simulated AM1.5G irradiation in Si:Cu_3TiO_x. Ti:$CuSiO_3$ was found to be a highly doped semiconductor. The high-throughput translation stage allowed to record four high quality XRD patterns for each investigated PEC measurement area (Figure 2) on a full ternary metal oxide materials library for the first time at DELTA BL09. In Figure 3 the identified phases are shown. Region I denotes a mixed phase consisting of CuO and Cu_2O and probably X-ray amorphous Si-Ti-O. Region II comprises the Cu-Ti-O quasi-binary phase in which several mixed phases (Cu_2O, CuO, TiO_x, $Cu_{1-x}Ti_xO_y$) exist. Region III consists of X-ray amorphous Ti-rich Ti-Cu-Si-O and off-stoichiometric $SiTiO_x$ phases. The phase region IV near a nominal composition of $Cu_{50}Si_{50}O_x$ is identified to be a mixture of dioptase and copper-polysilicate.

In Figure 4 the X-ray diffraction pattern for $CuSiO_3$, which was identified to be a solid solution of copper-polysilicate (CuSiO3) and dioptase ($Cu_6Si_6O_{18}$) is shown. The obtained ternary phase diagram is correlated

with photoelectrochemical data. The manuscript is currently in the resubmission process to Journal of Materials Chemistry A.

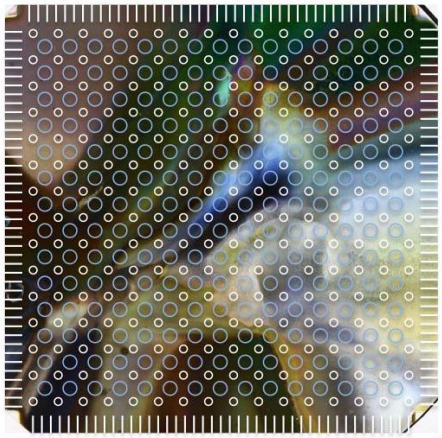

Figure 2: Overlay of the measurement areas for each high-throughput measurement technique over a cropped photograph of the Cu-Si-Ti-O materials library. EDX and PEC measurements were performed on the same 16 x 16 grid (small white circles), XRD measurements were performed on a 15 x 15 grid (large blue circles).

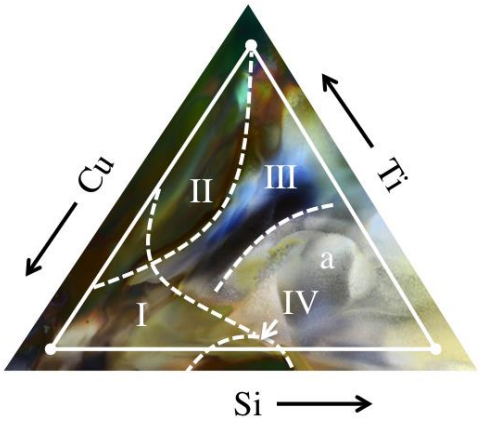

Figure 3: Quasi-ternary diagram showing the results of phase region identification overlaid with a RGB image of the oxidized Cu-Si-Ti library. White lines mark the rough boundaries of the ternary composition space whereas the dashed lines mark regions of different phase regions as identified by synchrotron XRD mapping.

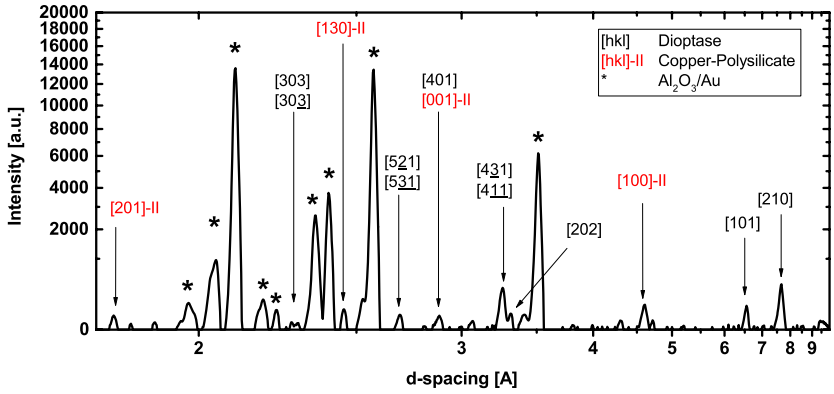

Figure 4: Synchrotron-XRD for phase region IV near a nominal composition of $Cu_{50}Si_{50}O_x$ that is identified to be a mixture of dioptase and copper polysilicate. This phase region exhibits promising PEC properties. Black stars denote substrate peaks from Au/Al_2O_3. The black indexes are corresponding to peaks from dioptase whereas the red indexes followed by the Roman numeral II denote those of copper-polysilicate.

Investigation of metal-organic framework thin films by X-ray scattering methods: crystallinity, crystallographic orientation and structural flexibility

Suttipong Wannapaiboon, Min Tu, Andreas Schneemann, Inke Schwedler, Wenhua Zhang, Konstantin Epp, Raghavender Medishetty, Olesia Kozachuk, Roland A. Fischer*

Chair of Inorganic Chemistry II-Organometallics and Materials Chemistry, Faculty of Chemistry and Biochemistry, Ruhr-Universität Bochum, D-44780 Bochum, Germany

Metal-Organic Frameworks (MOFs) or porous coordination polymers (PCPs), a new class of porous inorganic-organic hybrid materials, have been extensively investigated during the past decade due to their outstanding porosity, chemical modularity and structural diversity. MOFs are constructed by a building-block principle showing the formation of well-defined crystalline networks by coordination bonds between various kinds of metal centres (or inorganic clusters) and organic linkers. The versatility in the range of precursor components that can be used at the molecular scale offers possibilities for precise manipulation of the framework structure as well as its associated properties. This versatility makes MOFs promising materials for various real-world applications, ranging from gas storage, sensing, separation, and more recently, catalysis, bioreactors, and controlled drug release. In addition to tuning of the composition of MOFs, their physical form in the mesoscopic and macroscopic scales is known to uniquely affect their properties. The structuring of MOFs in two-dimensional superstructures (e.g. thin films) is an emerging field that has received an increased attention over the last few years due to their potential use in membranes, coatings, QCM-based sensors and microcantilever-based sensors.

Continuous stepwise liquid-phase epitaxial (LPE) growth is one of the most effective procedures for structuring metal-organic frameworks (MOFs) as two-dimensional superstructures, such as thin-films. Alternation of the building block precursors between the individual LPE growth cycles (i.e. from one linker to the other) allows heterostructured MOF films consisting of two different MOFs with different structural or chemical properties to be synthesized with a precise control of the growth sequence. We employed the LPE growth strategy for the preparation of highly functional, hierarchically structured core-shell architectures consisting of $[Zn_4O(3,5\text{-dialkylcarboxypyrazolate})_3]_n$-based frameworks. Specifically, the small-pore $[Zn_4O(3\text{-methyl-5-isopropyl-4-carboxypyrazolate})_3]_n$ (**Zn-MI**) and $[Zn_4O(3,5\text{-diethyl-4-carboxypyrazolate})_3]_n$ (**Zn-DE**) frameworks are respectively deposited as a size selective layer upon larger-pore $[Zn_4O(3,5\text{-dimethyl-4-carboxypyrazolate})_3]_n$ (**Zn-DM**) and $[Zn_4O(3\text{-methyl-5-ethyl-4-carboxypyrazolate})_3]_n$ (**Zn-ME**) layers. The crystalline phase of the MOF thin films was determined by the out-of-plane cuts of the two-dimensional grazing incidence X-ray diffraction (2D-GIXRD) data collected at Beamline 9 at DELTA Synchrotron, Germany (X-ray beam with energy of 12.38 keV or wavelength of 1.001 Å, sample-to-detector distance of 500 mm and the incidence angle of 0.6°). Multiple-component adsorption experiments in an environment-controlled quartz crystal microbalance (QCM) apparatus revealed size selectivity with respect to the adsorption of alcohols, as well as the molecular recognition of methanol over water, facilitating attractive synergistic properties for adsorptive selectivity and providing a possibility for further development in MOF-based sensing applications. [1]

Moreover, Coordination Modulation (CM) technique is applied into the LPE method to improve the synthetic procedure, so-called coordination-modulation assisted stepwise liquid phase epitaxial growth (CM-LPE), aiming for enhancing the quality of MOF thin films as well as controlling the crystallographic orientation. The presence of acetic acid as a modulator plays a role in altering the coordination equilibrium between metal SBUs and organic linker, which therefore affects the kinetic LPE growth of MOF thin films. Generally, the presence of modulator in the reaction retards the high degree of nucleation at the early stage whereas enhances the growth of the preformed nuclei into well-defined particles. However, the higher mole ratio of modulator retards the kinetic deposition of the MOF thin film on the substrate, resulting in less amount of deposited MOF film on the substrate surface (Figure 1a). Using of modulators in the optimal ratio during the LPE fabrication improves the crystallinity of the MOF films and controls the crystallographic orientation along the film growth direction as shown the preferred

[100]–related orientation in the out-of-plane XRD patterns (Figure 1b) and the discrete 2D-GIXRD patterns (Figure 1c), obtained at Beamline 9 at DELTA Synchrotron, Germany (X-ray wavelength 1.0013 Å, incidence angle 0.6° and refined sample-to-detector distance 440.0 mm). Moreover, the methanol total adsorption capacity of the CM-LPE fabricated MOF films is significantly enlarged according to the higher contribution of the effective mass (or the highly-crystalline MOF component) on the QCM substrate. This integrated CM-LPE method opens the way to fabricate the high-quality MOF thin films on the given substrates in a precise-controlled manner. [2]

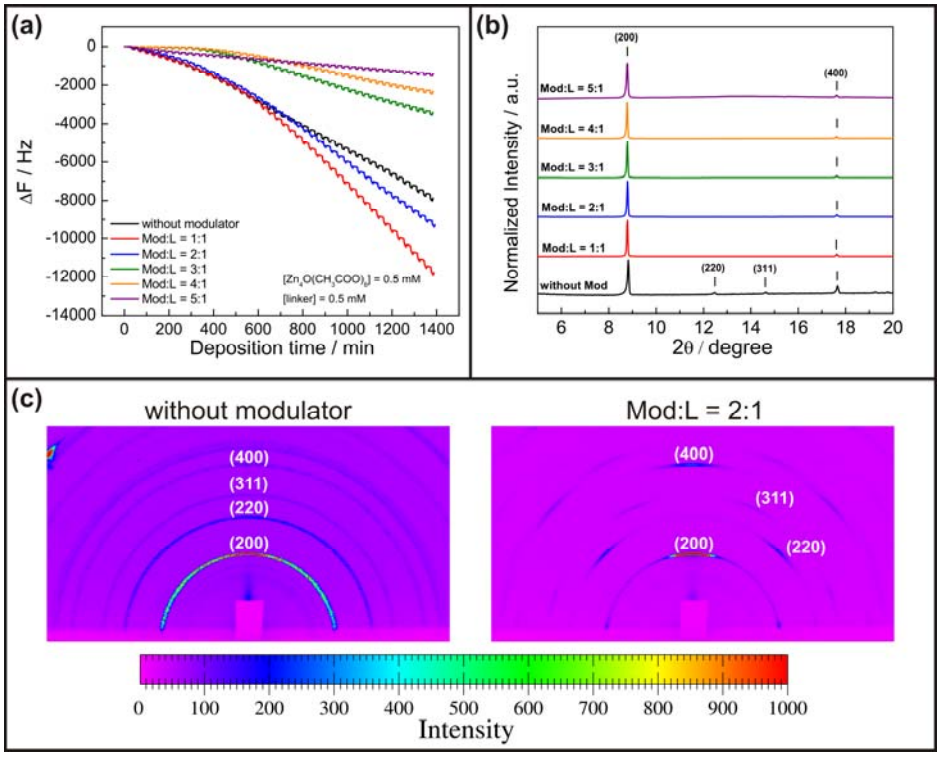

Figure 1 (a) In-situ monitoring of QCM frequency during the fabrication of **Zn-DM** films at 40 °C by CM-LPE method without seeding layer; using $Zn_4O(CH_3COO)_6$ 0.5 mM, H_2DM 0.5 mM as precursor solutions and CH_3COOH as coordination modulator with various modulator-to-linker mole ratio (Mod:L), (b) the corresponding out-of-plane X-ray diffraction patterns of the **Zn-DM** films and (c) the comparison of the 2-dimensional grazing incidence X-ray diffraction patterns (2D-GIXRD) of **Zn-DM** films fabricated without using modulator and with modulator-to-linker mole ratio of 2:1.

Moreover, the structural flexibilities upon guest molecules adsorption/desorption as well as temperature-dependence of the pillared-layered $[Cu_2(fu\text{-}bdc)_2(dabco)]_n$ surface-mounted MOFs (fu-bdc = 2,5-dialkoxy-1,4-benzenedicarboxylate) are investigated by the *in-situ* grazing incidence X-ray diffraction (GID) during the organic vapor adsorption/desorption as well as heating at the Beamline 9, DELTA Synchrotron, Germany. [3]

References

[1] S. Wannapaiboon, M. Tu, K. Sumida, K. Khaletskaya, S. Furukawa, S. Kitagawa and R. A. Fischer, *J. Mater. Chem. A* **2015**, DOI: 10.1039/C5TA05620A.

[2] S. Wannapaiboon, K. Sumida, M. Tu, K. Dilchert, S. Furukawa, S. Kitagawa and R. A. Fischer, manuscript in preparation

[3] This project is continued in the 2015-2016 DELTA Proposal. The results will be provided later.

Characterisation of selective oxidised steel surfaces by GIXRD

D. Wulff[a], U. Holländer[a], D. Lützenkirchen-Hecht[b] , R. Wagner[b], D. Yilkiran[c], B.-A. Behrens[c], K. Möhwald[a], H.J. Maier[a]

a) Institut für Werkstoffkunde, Leibniz Universität Hannover, An der Universität 2, 30823 Garbsen
b) Fachbereich C - Physik, Bergische Universität Wuppertal, Gaußstr. 20, 42097 Wuppertal
c) Institut für Umformtechnik und Umformmaschinen, Leibniz Universität Hannover, An der Universität 2, 30823 Garbsen

In the metal forming industry, especially during the deep drawing process, where a large contact zone between the sheet metal and the tool exists, friction plays a significant role. Nowadays, liquid lubricants and here lubricating mineral oils are mainly used to optimise the friction conditions. Due to the negative impact of liquid lubricants to the environment and the necessity of additional cleaning stages in the production, lubricant-free process concepts by means of friction reducing tool surfaces are required [1].

Approach

In a joint project of the priority program „Dry metal forming – sustainable production through dry processing in metal forming" (SPP 1676) [2], friction reducing tool coatings are generated by selective oxidation at 500°C. The oxidation process took place in a conveyor belt furnace under a defined atmosphere containing N_2 as an inert gas and a small amount of SiH_4 as reducing additive. Depending on the residual level of oxygen, different surface modifications are already apparent on the macroscopic scale on the tool steel (EU alloy grade 1.2379, X153CrMoV12), as reported previously [3]. The characterisation of the oxide layers on the microscopic scale is difficult because the layers can be very thin (< 100 nm), and the layers may consist of different oxides. Therefore GIXRD measurements using synchrotron radiation are a valuable nondestructive technique to analyse the crystal structure and to receive depth profiles by a variation of the incidence angles.
The measurements have been performed at BL 10 using an energy of 10 keV. The incidence angles have been varied between 1° and 10°, while the PILATUS detector has been fixed at diffraction angles of 45° or 30°, respectively. At the elevated distance between detector and sample a diffraction angle segment of about 20° has been recorded by the PILATUS detector. The threshold of the detector was adjusted to 8.5 keV to eliminate the contributions of fluorescence radiation from the samples to the recorded diffraction patterns. The relation between detector channels and diffraction angle has been adjusted by the measurement of various reference materials (e.g. Fe, Cr, α-Fe_2O_3 and γ-Fe_2O_3). Patterns overdrawing a diffraction angle of about 35° have been obtained by merging the data from measurements at the two detector angles.

Results

In Fig. 1, 2D GIXRD patterns of four exemplary samples for an incident angle of $\Theta = 2°$ are presented. RN is an untreated reference sample. R1 and R2 have been processed under $N_2 + SiH_4$ (ca. 10 ppm) resulting in a detected partial oxygen pressure between 10^{-13} and 10^{-17} mbar. On the contrary R3 has been heat treated under pure N_2 and a partial oxygen pressure of $(1.5 \pm 0.5)\ 10^{-1}$ mbar.
Every pattern, regardless of the treatment, has an intensive reflex at about 35.6° and a second reflex at about 51.3° that can be assigned to α-Fe. A third and fourth reflex at about 31.3° and 41.5° can be related to Cr_7C_3. Noticeable the Cr_7C_3 reflexes of the heat treated samples are much more present which can be explained by an increase of the hardness as a result of a secondary hardening process during the heat treatments. All four reflexes (31.3°, 35.6°, 41.5° and 51.3°) are also visible at higher

incident angles and therefore originate from the pristine steel substrate. Because these reflexes are even detectable at Θ = 1°, all formed surface layers can be estimated to be smaller than 250 nm.

Sample R3 shows ten additional reflexes compared to the untreated reference sample RN. All new reflexes belong to Fe_2O_3. Their intensities decrease with higher incident angles, what implicates that Fe_2O_3 has formed on the surface of the sample. The Fe_2O_3 layer is a mixture of α-Fe_2O_3 and γ-Fe_2O_3, whereupon the α-Fe_2O_3 dominates. Only one reflex (24.3°) is assigned just to γ-Fe_2O_3, while two other reflexes (45.5° and 28.5°) can be associated to both species of Fe_2O_3. The intensity of the reflex at 24.3° decreases faster with increasing incident angle than the other reflexes of α-Fe_2O_3. It can thus be assumed that a very thin γ-Fe_2O_3 layer covers the α-Fe_2O_3. On R2, only one additional, less intensive reflex at 28.5° can be detected for small incident angles. It is presumed that it belongs to a small amount of Fe_2O_3 on top of this sample. Scanning electron microscope (SEM) images have shown a dense particle coverage with particle sizes up to 70 nm here. R1 yields the same reflexes as the untreated sample RN and is the only heat treated sample which shows no discolourations on the macroscopic scale. The light partial coverage seen on SEM images must consist of an amorphous phase therefore.

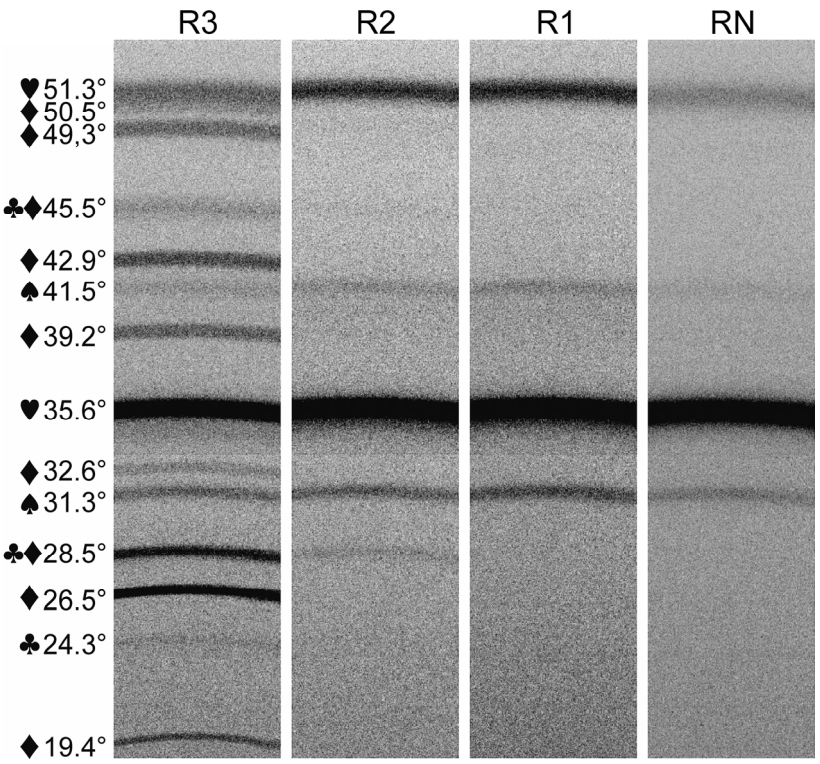

Figure 1: 2D GIXRD patterns of sample R1, R2, R3 and the untreated reference sample RN at an incident angle of Θ = 2°. The measured intersections of the diffraction cone with the detector surface have been assigned as follows: α-Fe (♥), α-Fe_2O_3 (♦), Cr_7C_3 (♠) and γ-Fe_2O_3 (♣).

The performed GIXRD measurements are meaningful concerning the analysing of the modification of crystal structure induced by the heat treatments. Additional analysing methods (EXAFS, XPS etc.) are being in progress, to gain further information about the surface modifications.

Acknowledgements

The research has been funded by the German Research Foundation grant numbers MA1175/41-1 and BE1690/170-1. The authors gratefully thank the DELTA machine group for providing reliably synchrotron radiation.

References

[1] F. Vollertsen, F. Schmidt, Dry metal forming: Definition, chances and challenges. Int. J. Precision Engineering and Manufacturing – Green Technology 1/1 (2014) 59-62

[2] http://www.trockenumformen.de/

[3] D. Wulff, D. Yilkiran, U. Holländer, D. Lützenkirchen-Hecht, R. Wagner, S. Hübner,K. Möhwald, H.J. Maier, B.-A. Behrens, Dry Met. Forming OAJ FMT 1 (2015) 72-78

Hard X-ray spectroscopy

Local atomic and electronic structure of Ag clusters deposited in a polymethylmethacrylate (PMMA) matrix

Stefanie Roese*,[a], Dominik Wolter[a], Stefan Balk[b], Ralph Wagner[b], Christian Sternemann[a] and Heinz Hövel[a]

[a] *Fakultät Physik/DELTA, TU Dortmund, Otto-Hahn-Str. 4, 44221 Dortmund, Germany;*

[b] *Bergische Universität Wuppertal, Fachbereich C, Fachgruppe Physik, Gaußstr. 20, 42119 Wuppertal, Germany;*

*email: stefanie.roese@tu-dortmund.de

In this report we describe first results of our x-ray absorption near edge structure (XANES) spectroscopy measurements at the Ag L_3 absorption edge of Ag clusters embedded into a polymethylmethacrylate (PMMA) matrix compared to an Ag reference sample performed at beamline BL8 of the synchrotron radiation facility DELTA, TU Dortmund.

Clusters assembled materials are of great impact for future applications in science and nanotechnology [1],[2],[3]. Despite the importance of these materials only a few studies on their local electronic and atomic structure are available. Optical properties of noble metal clusters and nanostructures such as their UV-VIS absorption band alter significantly with size, shape and interparticle spacing as well as with the properties of the local environment. X-ray absorption near edge structure (XANES) spectroscopy yields unique structural and chemical information on supported and embedded Ag clusters. It is well suited to investigate the chemical environment of the Ag clusters and allows the study of changes of the unoccupied density of states (uDOS).

Using embedding media such as PMMA or the polymer polymethylsiloxane (PDMS) it is possible to deposit more clusters than on a SiO_2 substrate without risking coalescence of the clusters [4]. Recent data taken for Ag clusters embedded into PDMS have already shown that the XANES signal of an Ag reference film and the embedded clusters show significant differences. With increasing cluster coverage a transition from the cluster signal to the bulk signal is visible. Furthermore, for the lowest cluster coverages (where all clusters are separated from each other) the embedding material seems to be influencing the XANES spectra of the clusters directly behind the edge onset (see fig. 1).

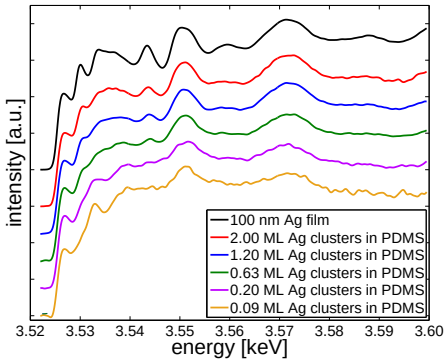

Figure 1: L_2 XANES of Ag clusters embedded into PDMS [5].

The uDOS of clusters is different from that of bulk Ag which manifests depending on their size in quantized or bulk-like properties. Thus, the uDOS is strongly influenced by the size which is under investigation. Starting with Ag clusters of 2 nm size produced with THECLA (Thermal CLuster Apparatus) [6] we investigate sample positions with different cluster coverage. For increasing coverage particles larger than 2nm are formed by coalescence.

In this study the changes in the chemical and physical properties of several cluster sizes obtained by preparation of different cluster densities embedded in a thin film of polymethylmethacrylate (PMMA) are examined. Here the penetration depth is lower than in PDMS [4], thus less cluster material can be embedded into the matrix before coalescence starts. The Ag clusters are produced and deposited with a THErmal CLuster Apparatus (THECLA) which utilizes a high-temperature nozzle to form clusters in a supersonic expansion. By using a wedge shaped aperture we are able to deposit the clusters with a coverage gradient to investigate different cluster densities on the sample as shown in fig. 2.

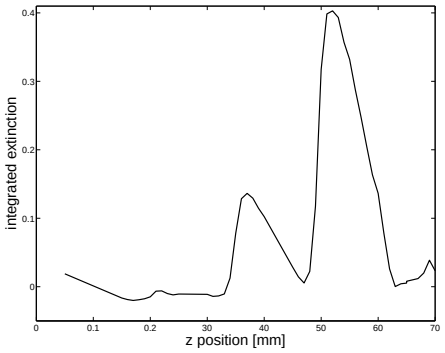

Figure 2: Profile of the PMMA sample with different deposition amounts of Ag clusters.

In addition to UV/Vis transmission experiments showing the Ag cluster plasmon, we performed XANES measurements at BL8, DELTA, using the Si(111) monochromator to investigate the L_3 absorption edge of Ag clusters in PMMA and an Ag reference film. All samples were measured utilizing the vacuum sample environment available at BL8, DELTA. Fig. 3 shows the XANES measurements for different cluster coverages. Although the small amount of cluster material in the samples provided only a low signal to noise ratio there are visible changes of the XANES features at the Ag L_3 absorption edge compared to bulk silver. We do not find extra spectral features of the PMMA in the spectra for the lowest cluster coverage of 0.2 ML. To investigate even lover coverages, additional measurements are planned to be performed.

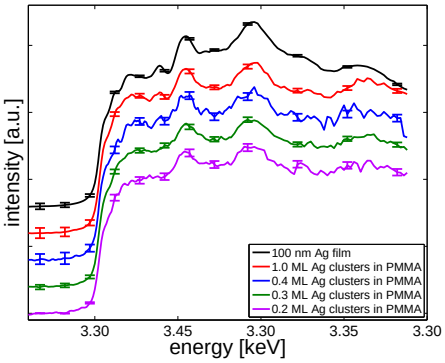

Figure 3: Profile of the PMMA sample with different deposition amounts of Ag clusters.

Conclusion

The performed XANES experiments on Ag clusters embedded into PMMA could not confirm or disprove if PMMA influences the uDOS of the clusters. Due to the low signal to noise ratio it was not possible to measure lower coverages on the PMMA sample to see, if they show different edge features than the higher coverages as it was observed for embedding in PDMS.

Acknowledgments

The authors would like to acknowledge the DELTA machine group for providing synchrotron radiation and technical support.

References

[1] R.E. Palmer, S. Pratontep and H.-G. Boyen, Nature Materials **2**, 443 (2003).

[2] Z.Y. Li, N.P. Young, M. Di Vece, S. Palomba, R.E. Palmer, A.L. Bleloch, B.C. Curley, R.L. Johnston, J. Jiang, and J. Yuan, Nature **451**, 46 (2008).

[3] S. Duffe, N. Grönhagen, L. Patryarcha, B. Sieben, C. Yin, B. von Issendorff, M. Moseler, H. Hövel, Nature Nanotechnol. **5**, 335 (2010).

[4] L. Ravagnan, G. Divitini, S. Rebasti, M. Marelli, P. Piseri and P. Milani, J. Phys. D **42**, 082002 (2009).

[5] S. Roese, D. Engemann, S. Hoffmann, K. Latussek and H. Hövel, submitted, 2015

[6] U. Kreibig, M. Gartz, A. Hilger, H. Hövel, Optical Investigations of Surfaces and Interfaces of Metal Clusters, In: Advances in Metal and Semiconductor Clusters Vol. 4, (ed. M.A. Duncan), JAI press Inc., **345** (1998).

Temperature dependent EXAFS measurements of iron and niobium from room temperature to 900°C

Benjamin Bornmann, Serena Schlottmann, Jonas Klaes, Jonas Klappert,
Ralph Wagner, Ronald Frahm and Dirk Lützenkirchen-Hecht

FK 4 - Physik, Bergische Universität Wuppertal, Gaußstr. 20, 42097 Wuppertal, Germany.

Many treatments of metals and alloys are conducted at high temperatures, employing various gases in order to obtain tailored properties of the materials. For example, niobium may be exposed to N_2 for T > 800°C leading to NbN surfaces layers depending on the temperature [1], and oxide layers on steels can be produced in oxygen-containing atmospheres [2]. On the other hand, a removal of those oxides is feasible in monosilane (SiH_4) – containing gases at elevated temperatures [3], and also a vacuum treatment at temperatures around 900-1000°C may remove those oxides.
The extended X-ray absorption fine structure technique (EXAFS) is able to specify the accurate local short range structure around the X-ray absorbing atom (see, e.g. [4]). In contrast to X-ray diffraction, EXAFS is not relying on the presence of a long-range order structure in the samples of interest, and thus well-suited for the investigation of disordered materials, glasses and liquids, and could be applied for structure measurements at elevated temperatures as well.
Here we focus on the investigation of Nb and Fe metal foils at high temperatures. The main idea of the conducted experiments are observations of anharmonic lattice vibrations making use of the inherent short range order sensitivity of the EXAFS method [5, 6]. For this purpose, a high temperature cell (Anton Paar domed hot stage DHS 1100 with controller TCU 200) has been installed at DELTA beamlines 8 and 10. While a Si(111) monochromator and N_2- and Ar-filled ionization chambers were used for the experiments at the Fe K-edge (7112 eV) at Bl10, a Si(311) monochromator at Bl8 and Ar- and Xe gas fillings were employed for the Nb K-edge (17998 eV) studies.

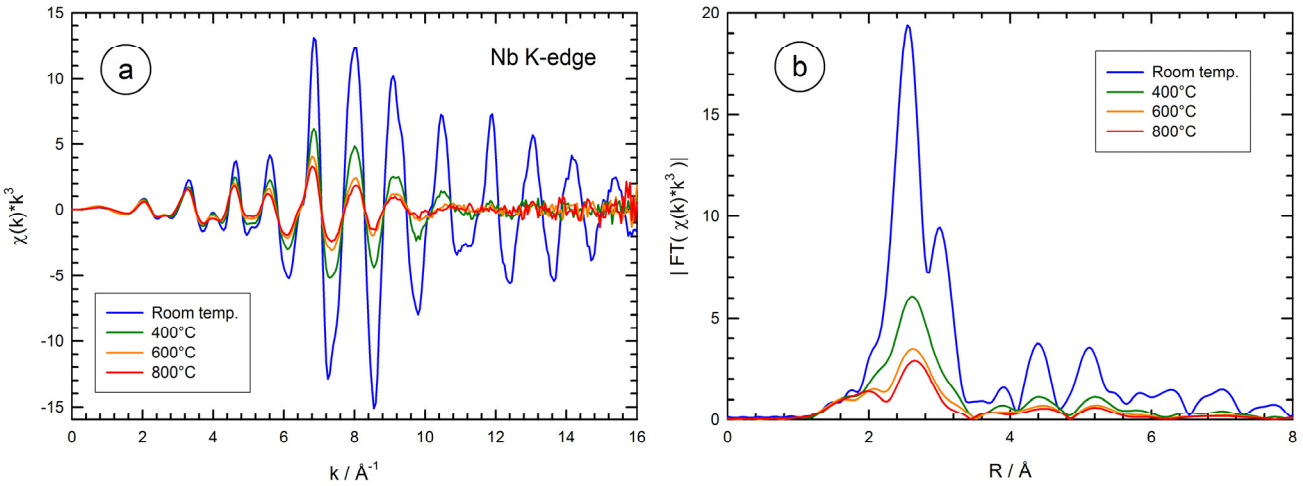

Fig. 1: (a) k^3-weighted X-ray absorption fine structure extracted from absorption data of a Nb metal foil measured at different temperatures in the vicinity of the Nb K-edge (17998 eV) as indicated. (b) Magnitude of the Fourier-transform of the $\chi(k)*k^3$ data for different temperatures.

In Fig. 1, the strong influence of the temperature on the Nb EXAFS data is obvious, both the amplitude of the EXAFS oscillations $\chi(k)*k^3$ as well as the magnitude of the Fourier-transform $|\,FT(\chi(k)*k^3)\,|$ decrease substantially with increasing temperature. While strong EXAFS oscillations are detectable up

to k = 20 Å^{-1} at room temperature, the measured $\chi(k)*k^3$ does not show any well-defined amplitude for k > 12 Å^{-1} already for T = 400°C due to the increasing amplitude of the lattice vibrations and the presence of anharmonic effects. Qualitatively the same features were observed for the temperature dependence of the Fe K-edge data of the Fe foil (Fig. 2).

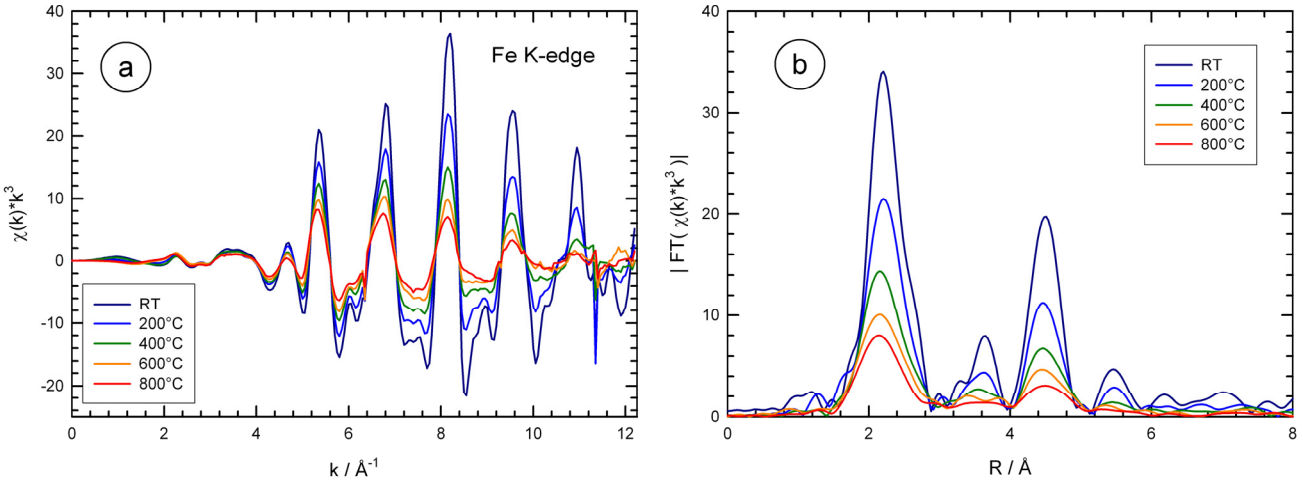

Fig. 2: k^3-weighted X-ray absorption fine structure extracted from absorption data of an iron metal foil measured at different temperatures in the vicinity of the Fe K-edge (7112 eV) as indicated. (b) Magnitude of the Fourier-transform of the $\chi(k)*k^3$ data for different temperatures.

A detailed evaluation of the measured data is currently in progress, preliminary fit results show a substantial increase of anharmonic contributions for temperatures above ca. 400°C in the case of iron. Furthermore, repeated heating and cooling of the Nb metal foil shows that there are irreversible changes in the measured spectra, which are indicating an oxidation of the Nb metal foil at elevated temperatures of more than 500°C. Such a high temperature oxidation may be expected for a valve metal under the vacuum conditions of about 10^{-2} mbar available in the used domed hot stage. In the case of iron, such an oxidation was not observed. However, a high-temperature vacuum chamber offering ultrahigh vacuum conditions is currently under construction and will be commissioned in early 2016, so that high temperature studies in an oxygen-free environment will be feasible.

References

[1] P. Dhakal, et al, Phys. Rev. Special Top. Acc. Beams 16 (2013) 42001.
[2] J.-M. Abels, H.-H. Strehblow. Corrosion Science 39 (1997) 115.
[3] D. Lützenkirchen-Hecht, D. Wulff, R. Wagner, R. Frahm, U. Holländer, H. J. Maier, J. Mat. Sci. 49 (2014) 5454.
[4] D.C. Koningsberger, R. Prins (eds.) X-ray absorption: Principles, Applications, Techniques of EXAFS, SEXAFS and XANES. John Wiley & Sons: New York (1988).
[5] N. van Hung, T.S. Tien, L.H. Hung, R. Frahm. Int. J. Mod. Phys. B 22 (2008) 5155
[6] M.A. Karolewski, R.G. Cavell, R.A. Gordon, C.J. Glover, M. Cheah, M.C. Ridgway. J. Synchrotron Rad. 20 (2013) 555.

Investigation on the Ru-sites of the ruthenium Defect-Engineered Metal-Organic Frameworks by XAS

Wenhua Zhang, Ralph Wagner and Roland A. Fischer

Metal-Organic Frameworks (MOFs), constructed from metal-centers and organic linkers, are an attractive field of research due to their properties in gas sorption, storage, sensors, drug delivery, catalysis, etc.[1] $[Cu_3(BTC)_2]$ (also known as HKUST-1),[2] represents one of the most well investigated porous MOF materials. $[Cu_3(BTC)_2]$, features Cu(II) paddle wheel Secondary Building Units (SBUs) bridged by four carboxylate groups. In the paddle wheel unit of the as-synthesized materials, two copper atoms are coordinated by four carboxylate groups to form a square, and solvent molecules *e.g.* water are weakly connected to the axial positions. Upon heating the samples under vacuum (*i.e.*, activation), the water molecules are removed, and accessible Cu^{II} sites are exposed, which named coordinatively unsaturated metal sites (CUS). These CUS can serve as Lewis acid sites for many catalytic reactions. $[Ru_3(BTC)_2Cl]$ was found to be a structural analogue to $[Cu_3(BTC)_2]$,[3] containing mixed-valence $Ru_2^{II,III}$ paddle wheel units. The same as $[Cu_3(BTC)_2]$, CUS are exposed after the materials were activated. In order to enhance the accessibility of CUS and tailor the property of the materials, the mixed-linker solid solution approach was used for the synthesis and introduction of structural defects into the mixed-valence $[Ru_3(BTC)_2Cl]$(Fig. 1). Compared with the parent Ru-MOF which does not contain defect linker, the defect MOFs featured with modified CUS are more likely to provide fantastic catalytic activity and sorption behavior while keep the overall integrity. [4]

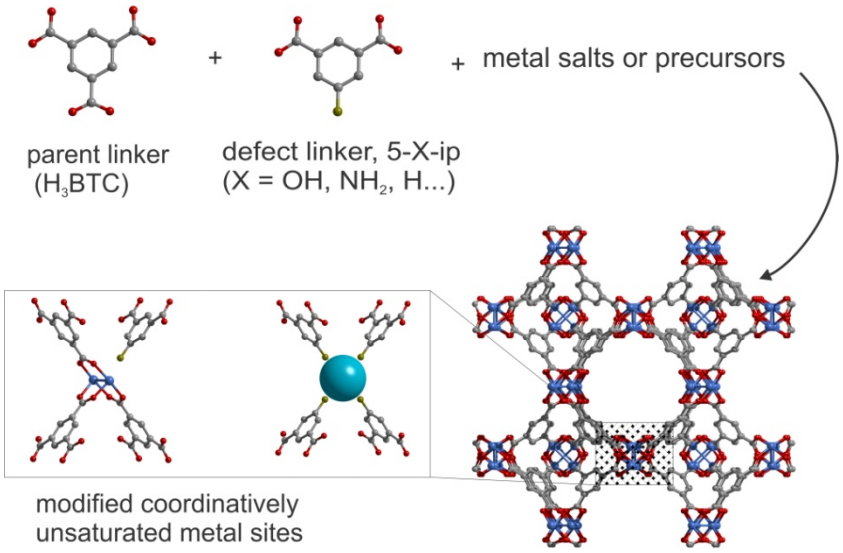

Fig. 1 Scheme of Defect-engineered metal- organic frameworks and the modified coordinatively unsaturated metal sites(CUS).

We have characterized the materials with different technique such as Powder X-Ray diffraction (PXRD), FT-IR, ^{1}H-NMR, Thermogravimetric analysis (TGA) and N_2 Sorption. The PXRD patterns show that the Ru-MOFs are phase-pure crystalline solids, isostructural with parent $[Ru_3(BTC)_2Cl]$. The ^{1}H-NMR spectra indicate there is more amount of defect linker incorporation along with the doping increasing. However, it's difficult to investigate the environment of modified CUS in these materials in detail based on these techniques. In order to know the oxidation state and local structure of the metal sites, X-ray absorption spectroscopy (XAS) was carried on the selected defect-engineered Ru-MOFs.

From the derivative absorption of the edge jump for different materials in the XANES region, the oxidation state of the parent Ru-MOF ($[Ru_3(BTC)_2Cl]$) and its defect materials can be obtained. RuO_2, Ru and $RuCl_3$ are used as standards representing the oxidation state 4+, 0 and 3+, respectively. $Ru_2(AcO)_4Cl$, which has a similar mixed valence $Ru^{II,III}$- paddlewheel unit as that in parent MOF ($[Ru_3(BTC)_2Cl]$) represent the oxidation state 2.5+. In comparison to all the standards, parent Ru-MOF behave an oxidation state between 2.5+ and 3+ (Fig. 2a). The edge-jump from defect Ru-MOFs with various doping level exhibit different position with parent MOFs as we can see from Fig. 2b, which indicate up to 30% 5-OH-ip doping, the average oxidation state of ruthenium in these materials decreased. This is agreement with what we expected from previous characterization and adsorption property. Modified CUS formed in the defect Ru-MOFs materials result in the valence change. Further study on the local structure of the metal sites in the Defect materials are still under processing and will be published later together with our other work on this project.

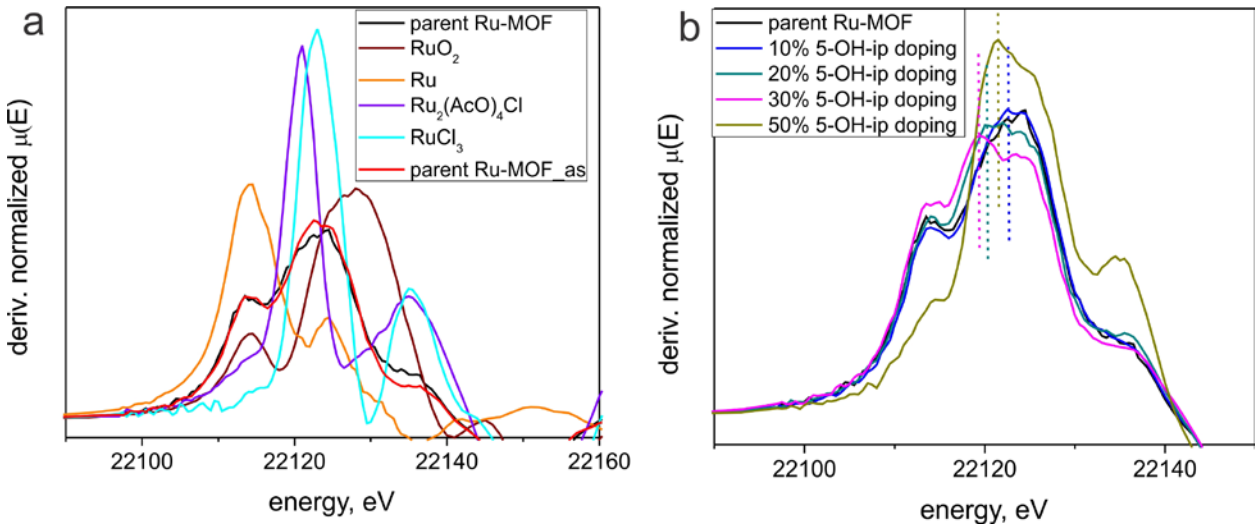

Fig. 2 Derivative absorption of the edge jump in the XANES region for different standards, parent Ru-MOFs(a) and defect-engineered MOFs(b).

[1] a J. L. C. Rowsell, O. M. Yaghi, *Microporous Mesoporous Mater.* **2004**, *73*, 3; b R. B. Getman, Y.-S. Bae, C. E. Wilmer, R. Q. Snurr, *Chem. Rev.* **2012**, *112*, 703; c J. Lee, O. K. Farha, J. Roberts, K. A. Scheidt, S. T. Nguyen, J. T. Hupp, *Chem. Soc. Rev.* **2009**, *38*, 1450.

[2] S. S. Y. Chui, S. M. F. Lo, J. P. H. Charmant, A. G. Orpen, I. D. Williams, *Science* **1999**, 283, 1148.

[3] O. Kozachuk, K. Yusenko, H. Noei, Y. Wang, S. Walleck, T. Glaser, R. A. Fischer, *Chem. Comm.* **2011**, *47*, 8509.

[4] O. Kozachuk, I. Luz, F. X. Llabres i Xamena, H. Noei, M. Kauer, H. B. Albada, E. D. Bloch, B. Marler, Y. Wang, M. Muhler, R. A. Fischer, *Angew.Chem. Int. Ed.* **2014**, *53*, 7058.

Investigation of Eu-doping of barium aluminate ($BaAl_2O_4$) by XANES/EXAFS

D. Lützenkirchen-Hecht[a], B. Gržeta[b], M. Vrankić[b], R. Wagner[a]

a) Fachbereich C - Physik, Bergische Universität Wuppertal, Gaußstr. 20, 42097 Wuppertal, Germany.
b) Ruđer Bošković Institute, Division of Materials Physics, Bijenička cesta 54, 10000 Zagreb, Croatia.

Europium doped barium aluminate $BaAl_2O_4$ is a luminescent material with emission in the red spectral range [1], and is widely used in the field of optical communication and electronics [2]. In particular, $BaAl_2O_4$ exhibits good luminescence properties when it is doped/co-doped with rare-earth or transition-metal cations [2, 3]. Despite the actual use of doped barium aluminate in optoelectronic devices, structural investigations have not yet been precisely performed so far. In this context, we have conducted X-ray absorption measurements at the absorption edges of the dopant and the host elements in order to elucidate the mechanism of incorporation of Eu in the $BaAl_2O_4$ host structure, as well as to understand the origin of the optical/ luminescence properties of Eu-doped barium aluminate. Powder samples of undoped $BaAl_2O_4$ and ones of $BaAl_2O_4$ doped with 4, 6 and 8 at.% Eu (in relation to Ba) were prepared by a hydrothermal method and subsequently annealed at 1100 ºC for 4h [4]. The Eu L_3-edge X-ray absorption experiments on the doped samples were performed at DELTA beamline 10 [5], using the Si(111) channel cut monochromator, ionization chambers for the incident and transmitted intensities, and a silicon drift diode with a multichannel analyzer for the detection of the fluorescence from the samples. In Fig. 1, Eu L_3 XANES spectra of $BaAl_2O_4$ doped with 4, 6 and 8 at.% Eu are compared to those of Eu_2O_3 as a reference for Eu^{3+}, and a glass sample containing both Eu^{2+} and Eu^{3+} in approximately equal amounts. As can be seen, Eu^{2+} leads to a strong white line feature at about 6975 eV, while Eu^{3+} reveals a white line at a substantially higher photon energy of 6983 eV [6], so that a discrimination of Eu^{2+} and Eu^{3+} appears to be straightforward. Accordingly, the Eu_2O_3 reference sample showed a strong absorption maximum at 6983.5 eV. Furthermore, also all of the Eu-doped $BaAl_2O_4$ samples revealed white line features at 6983.2 eV - 6983.5 eV, indicating that the europium in the doped samples possesses a 3+ valence, in contrast to the recent observations where strong indications for Eu^{2+} were given [7].

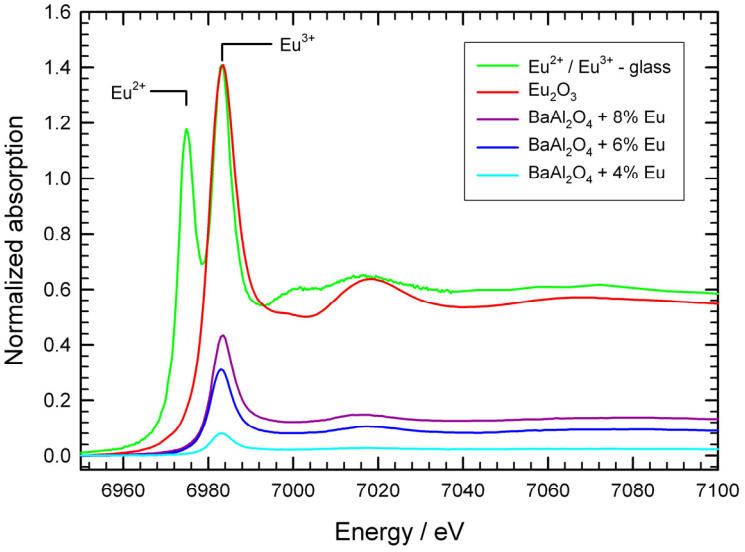

Fig. 1: Comparison of background - subtracted and normalized XANES spectra of Eu_2O_3 (—), Eu-doped $BaAl_2O_4$ with different Eu-concentrations (— 8%Eu, — 6%Eu, — 4 %Eu) as indicated, and a glass sample that contains Eu^{2+} and Eu^{3+} in approximately equal amounts (—).

Pure $BaAl_2O_4$ obeys a hexagonal crystal structure in the space group $P6_3$ at room temperature, with two structurally inequivalent Ba^{2+}-sites and four different Al^{3+}-sites [8, 9]. While barium atoms are 9-fold coordinated with Ba-O distances in the range from 2.69-3.00 Å, aluminum atoms are 4-fold coordinated with Al-O distances in the range of 1.71-1.83 Å. Thus it is straightforward to determine the Eu-coordination environment from the EXAFS data

measured at BL10. In Fig. 2, the Fourier-transform of the k^3-weighted EXAFS fine structure $\chi(k)*k^3$ of the $BaAl_2O_4$ sample doped with 8 at.% Eu is shown. From the Fourier-transformed data, the peak belonging to the first Eu-O coordination was isolated by means of a filter function, back-transformed into k-space and fitted with phases and amplitude functions calculated by FEFF [10]. A single Eu-O shell, with a nearest neighbour bond length R_1, coordination number N_1, and a mean square relative displacement σ_1^2, was used for the modeling of the experimental data. A typical fit result for the Eu-doped $BaAl_2O_4$ sample is also included in Fig. 2.

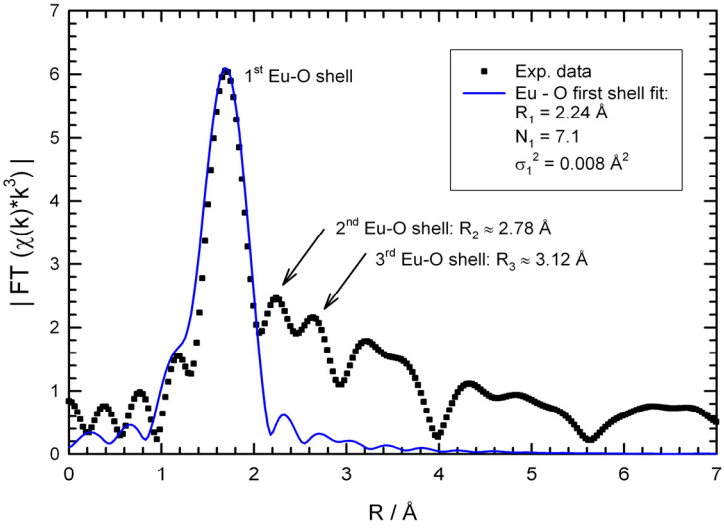

Fig. 2: Magnitude of the Fourier-transform of the k^3-weighted EXAFS fine structure $\chi(k)*k^3$ of a $BaAl_2O_4$ sample doped with 8 at.% Eu (full circles). Contributions of the first few Eu-O shells are indicated. Data related to the first shell are back-transformed to k-space and fitted with a single Eu-O bond. The fit is also depicted (—).

The bond distance determined for the first Eu-O bond (R_1 = 2.24 Å) is substantially smaller compared to the Ba-O bond distance in pure $BaAl_2O_4$ which amounts to ca. 2.8 Å. However, it is also smaller compared to pure Eu_2O_3, for which an Eu-O bond distance of 2.35 Å was determined, in accordance to the crystallographic data. The large coordination number determined is not at all compatible with a tetrahedral or octahedral coordination symmetry with 4 or 6 nearest neighbors, but suggests the location of Eu^{3+} on the Ba^{2+}-sites instead. Additional EXAFS experiments are planned in order to elucidate the short-range order structure around the Eu in more detail, and a detailed structural evaluation of the EXAFS data appears useful for all the Eu concentrations. Furthermore, an $EuAlO_3$ reference sample [11] will be measured to exclude the presence of such a secondary phase in the doped $BaAl_2O_4$ sample.

References

[1] Y. Lin, Z. Zhang, Z. Tang, J. Zhang, Z. Zheng, X. Lu. Mater. Chem. Phys. 70 (2001) 156.
[2] C. Kim, I. Kwon, C. Park, Y. Hwang, H. Bae, B. Yu, C. Pyun, G. Hong. J. Alloys Compounds 311 (2000) 33.
[3] K. Fukuda, T. Iwata, T. Orito. J. Solid State Chem. 178 (2005) 3662.
[4] M. Vrankić, PhD-thesis, University of Zagreb, Croatia (2014).
[5] D. Lützenkirchen-Hecht, R. Wagner, S. Szillat, A.K. Hüsecken, K. Istomin, U. Pietsch, R. Frahm. J. Synchrotron Rad. 21 (2014) 819.
[6] C. Paßlick, O. Müller, D. Lützenkirchen-Hecht, R. Frahm, J.A. Johnson, S. Schweizer. J. Appl. Phys. 110 (2011) 113527 (1-5).
[7] M. Peng, G. Hong. J. Luminescence 127 (2007) 735.
[8] W. Hörkner, H.K. Müller-Buschbaum. Z. Anorg. Allg. Chem. 451 (1979) 40.
[9] S.-Y. Huang, R. von der Mühll, J. Ravez, J.P. Chaminade, P. Hagenmüller, M. Couzi. J. Solid State Chem. 109 (1994) 97.
[10] A. L. Ankudinov, B. Ravel, J. J. Rehr, S. D. Conradson. Phys. Rev. B 58 (1998) 7565.
[11] D. Petrov, B. Angelov, V. Lovchinov. J. Alloys Compounds 509 (2011) 5038.

Ex-situ EXAFS characterization of Co-electrodeposition

Damir Hamulić[a,b], Dirk Lützenkirchen-Hecht[b]

[a] *Faculty of Chemistry and Chemical technology, University of Ljubljana, Večna pot 113, 1000 Ljubljana, Slovenia*
[b] *Fachbereich C-Physik, Bergische Universität Wuppertal, Gaußstr. 20, 42097 Wuppertal, Germany*

1. Introduction

Coatings of transition metals such as Cobalt, Iron and Nickel have many applications in various technological fields, and Co-based materials are in particular used e.g. for energy storage [1] and solar energy conversion [2], electrochromic [3] or magnetoresistive devices [4], as well as for catalysts [5]. In this context, electrodeposition is a versatile technique for the preparation of metal and oxide coatings, and the composition of the electrolyte solution (i.e. pH, concentration of anions and cations, additives, etc.) have a decisive influence on the deposition and the resulting properties of the deposits. In this contribution, we will consider the electro-deposition of Co on Gold-coated Kapton foils, and study the resulting film properties (structure, thickness, morphology) as a function of the electrolyte composition and the deposition time using electrochemical methods, ex-situ scanning electron microscopy (SEM) and EXAFS experiments at DELTA beamline 10.

2. Experimental

Cobalt deposition was studied using different electrolytes, i.e. 0.1 M solutions of $CoSO_4$, $CoCl_2$ and $Co(NO_3)_2$. Electrodeposition took place at room temperature in a standard three electrode cell (ca. 100 cm^3) with a gold-coated Kapton foil as a working electrode, a platinum wire as a counter electrode and an Ag/AgCl reference electrode (E^0_h = 0.210 V), against which all potentials are reported. The gold working electrodes (1.70 cm^2) on polyimide (Kapton) were prepared by sputtering in an Ar-atmosphere for 360 s, resulting in a thickness of about 200 nm. The samples were prepared in the different solutions under a variation of the deposition potential and time. After preparation, they were removed from the electrolyte, carefully rinsed with destilled water and dried using nitrogen gas. Ex-situ SEM investigations were performed using a JEOL JSM 6510 system, and the X-ray investigations have been performed at DELTA beamline 10 using a Si(111) channelcut monochromator. N_2-filled ionization chambers were employed as detectors for the incident and transmitted X-ray intensities, and a third, Ar-filled ionization chamber was used to monitor a Co metal reference sample simultaneously with the actual samples under investigation. In a first series of experiments, different Co^{2+}-solutions with 0.1M concentration were studied for a deposition time of 300 s. In a second series, the concentration of $CoCl_2$ was varied from 0.005M to 1.0M, and in a third series, the influence of the deposition time was studied for a 0.02M $CoCl_2$ solution.

3. Results and discussion

Deposition of cobalt on gold surface was first investigated with 0.1M solutions of $CoSO_4$, $CoCl_2$ and $Co(NO_3)_2$ using cyclic voltammetry. Deposition was also tested in CoC_2O_4-solutions, but unfortunately the cobalt oxalate is not soluble in aqueous solution. The effect of the different solutions can be seen in Fig. 1 (left), where $CoCl_2$ shows the largest cathodic currents. The current density obtained for $Co(NO_3)_2$ is very similar to that of $CoCl_2$, but the anodic peak at ca. -0.23 V observed for $CoSO_4$ and $CoCl_2$ is absent for $Co(NO_3)_2$. Scanning electron microscopy (SEM) proves that the morphology of the deposits obtained in $CoSO_4$ and $CoCl_2$ are similar with a polycrystalline structure with grains of about 0.5 µm lateral size, with a slightly larger density of the crystallites for the deposition in $CoCl_2$. In contrast, the samples resulting from cathodic depositions in $Co(NO_3)_2$ as electrolyte obey fibrous, needle-like structures (Fig. 1, middle). The different structure of the latter deposits is also visible in the EXAFS data shown in Fig. 1, right, where depositions in $CoSO_4$ and $CoCl_2$ resulted in EXAFS signals that are very similar to those of a Co-metal reference. In contrast, the deposit from the $Co(NO_3)_2$ solution shows a completely different spectrum, that is not comparable to various reference compounds measured for comparison, i.e. $Co(OH)_2$, $Co(NO_3)_2$, CoO, Co_2O_3, etc. A more detailed analysis of this spectrum is currently under way and will be subject of future studies.

The electrochemical experiments have shown that the $CoCl_2$ electrolyte gave the largest cathodic currents during electrodeposition, as well as deposition in $CoCl_2$-solutions resulted in homogeneous polycrystalline Cobalt layers. Furthermore, the thickness of the deposits in $CoCl_2$ is substantially larger than those in $CoSO_4$, as can be anticipated from the larger edge-jump of the EXAFS spectra displayed in Fig. 1. While the edge jump

amounts to about 0.13 for 0.1M $CoCl_2$, only 0.07 were determined for $CoSO_4$, suggesting that the thickness of the film deposited in $CoSO_4$ is only half of that prepared in $CoCl_2$.

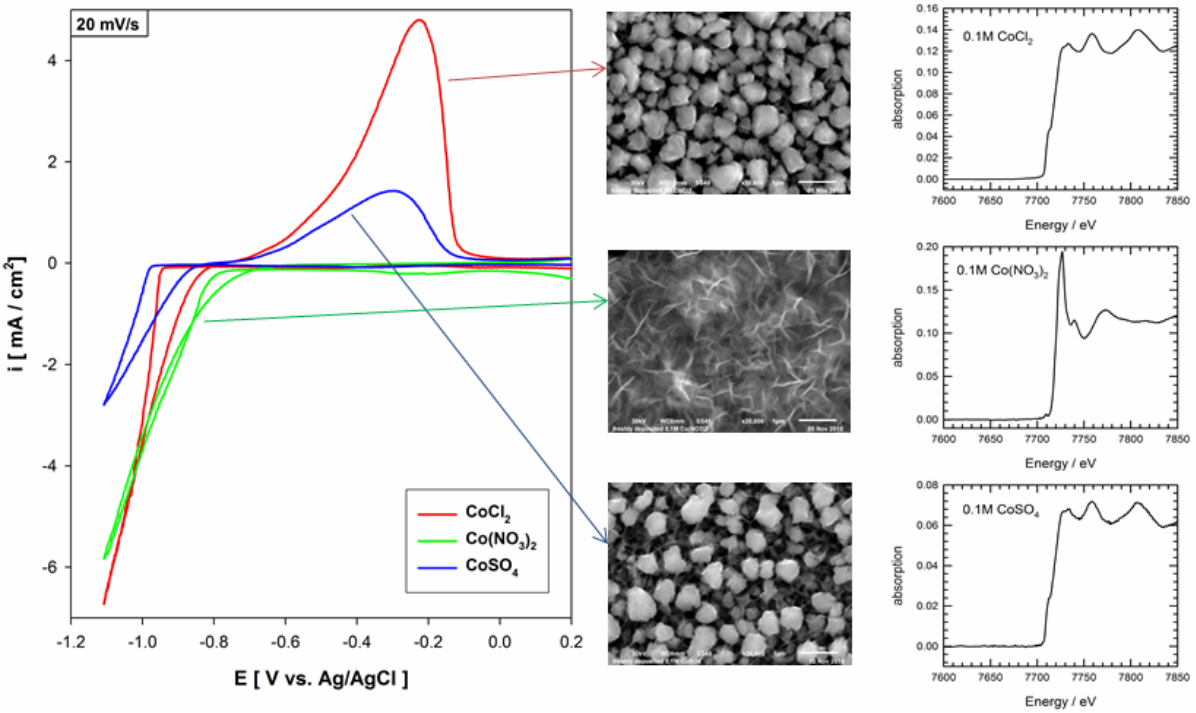

Fig. 1. (*left*) Cyclic voltammetry (20 mV/s) of different 0.1 M Co^{2+} solutions as indicated. (*middle*) The resulting film morphologies as determined by SEM at 20,000× magnification) of 0.1M $CoSO_4$, $Co(NO_3)_2$ and $CoCl_2$ (from top to down) obtained by deposition at -1.11 V for 300 s. (*right*) The measured EXAFS data of the three samples.

Therefore additional EXAFS investigations have been performed in $CoCl_2$ solutions to study the effect of Co^{2+}-concentration and deposition time on the deposits in more detail. Typical results are compiled in Fig. 2(a) for a deposition potential of -1.11 V and a deposition time of 300 s. As can be seen, metal deposits are formed for all the different $CoCl_2$ concentrations studied here. The edge-jump, i.e. the increase of the absorption above the edge, linearly increases with the Co-concentration, as depicted in more detail in Fig. 2(b), where the thickness derived from the edge jump by

$$d = \frac{\Delta A}{308.4\frac{cm^2}{g} \times \rho\,(Co)}$$

is shown for the various concentrations examined. Here, ΔA denotes the edge-jump, i.e. the difference in the absorption below and above the edge, ρ = 8.89 g/cm^3 is the bulk density of metallic Co, and the value of 308.4 cm^2/g is the change of the atomic X-ray absorption cross section at the Co K-edge according to ref. [6].

In a double-logarithmic plot, Fig. 2(b) clearly reveals a linear relation between the Co^{2+}-concentration in the used electrolyte and the resulting thickness, with a slope of about 3 μm per Mole Co^{2+}. This suggests that the growth is limited by the diffusion of the Co^{2+}-ions from the solution to the working electrode (see [7]). More important is the linear increase of the Co-thickness with deposition time, which is presented in Fig. 2(b). The growth rate determined from the linear slope of this graph amounts to ca. 0.52 ± 0.01 nm/s, i.e. about two monolayers of Co metal are deposited within a second.

For the future, a more elaborate analysis of the deposition process is under way. Besides the continuation of ex-situ experiments with EXAFS, also in-situ studies during growth are planned.

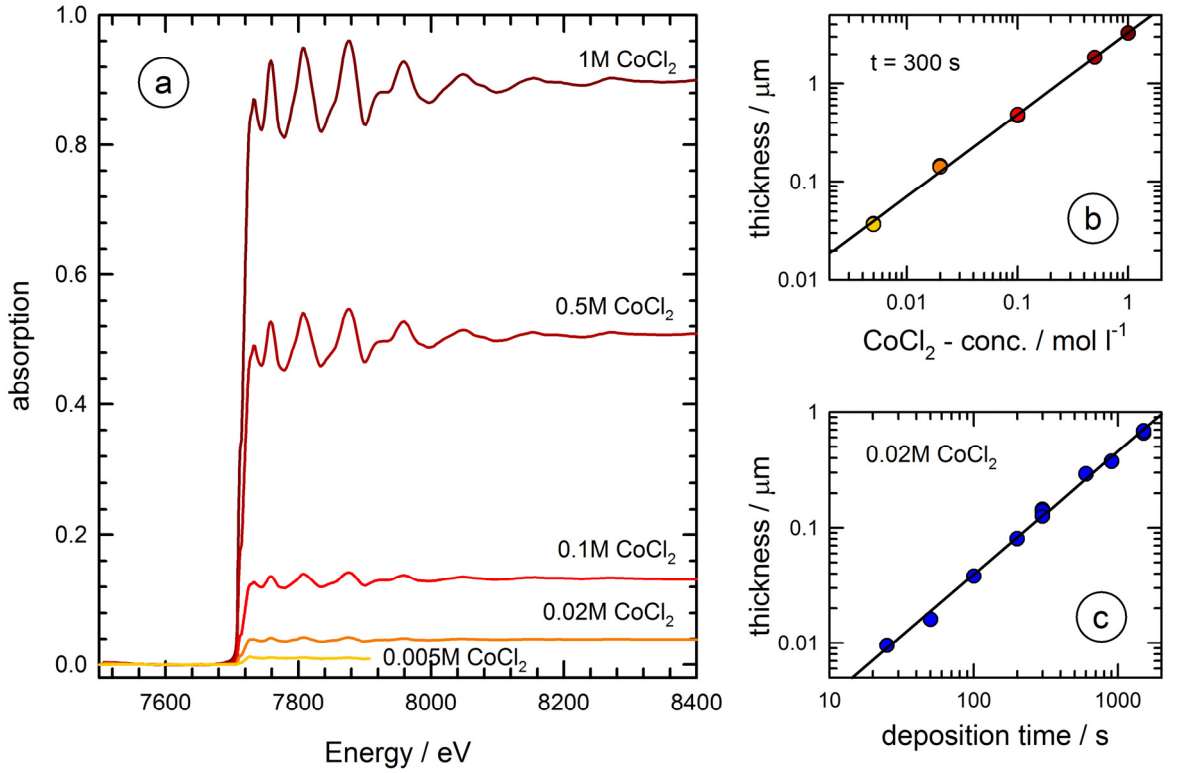

Fig. 2. (a) EXAFS of electrodeposited Co prepared at -1.11 V for different concentrations of $CoCl_2$ and 300 s deposition time. (b) Dependence of the thickness of the cobalt layers as a function of the Co^{2+}-concentration in the solution for a deposition time t = 300 s, and (c) Co-thickness as a function of the deposition time at -1.11 V in 0.02M $CoCl_2$-solution.

Acknowledgement

We gratefully acknowledge the DELTA machine group for providing synchrotron radiation reliably. D. Hamulić would like to thank the ERASMUS student exchange programme for the financial support of his visit in Wuppertal.

4. References

[1] J.J. Auborn, Y.L. Barberio, J. Electrochem. Soc. 134 (1987) 638.
[2] E. Barrera, I. Gonzales, T. Viveros, Solar Energy Mat. Solar Cells 51 (1998) 69.
[3] P.M.S. Monk, S. Ayub, Solid State Ionics 99 (1997) 115.
[4] Y. Ueda, N. Kikuchi, S. Ikeda, T. Houga, J. Magn. Mater. 198 (1999) 740.
[5] I.G. Casella, M.R. Guascito, Electrochim. Acta 45 (1999) 1113.
[6] D.C. Creagh, J.H. Hubbell, X-Ray Absorption (or Attenuation) Coefficients, Sec. 4.2.4. in *International Tables for Crystallography,* Vol. C, A.J.C. Wilson, ed. (Kluwer Academic Publishers, Dordrecht) (1992) 189-206.
[7] J. O'M. Bockris, A.K.N. Reddy, M. Gamboa-Aldeco. Modern Electrochemistry 2A Fundamentals of Electrodics. 2nd. Ed., Kluwer Academic/Plenum Publishers (2000) 1083.

Analytical characterization of a portrait of J. S. Bach.

A. von Bohlen[1], M. Paulus[2], A.K. Hüsecken[2,3], J. Hansen[2], W.-D. Köster[4] and M. Tolan[2].

[1] Leibniz-Institut für Analytische Wissenschaften ISAS-Dortmund
[2] Fakultät Physik/DELTA TU Dortmund, 44221 Dortmund
[3] Dept. Physics. Universität Siegen; [4]Dortmund

Three paintings showing J. S. Bach (1685-1750) were subjected to SR based XRF. Two of them belong to the permanent collection and exhibition in the "Bach House" in Eisenach. The question of genuineness of a third painting was of great interest. The reason is simple and astonishing as well: Beside the two paintings stored in Eisenach there is no other painting showing J.S. Bach and which was made during his life time.

The third painting was acquired by a gatherer to complete his Bach collection. As he knows that Bach's portraits are not common he decided to proof the genuineness of the painting. Therefore he contacted the "Bach House" and DELTA. The result was a first insight of the element composition of the three paintings. Fortunately, there are two options for realize a raw estimation of the age of the paintings: There are three white pigments – first, White Lead ($2PbCO_3$. $Pb(OH)_2$) known since the antiquity, Lithopone ($ZnS+BaSO_4$) first used in paintings around 1871, and Titanium White (TiO_2) first use about 1924.

The three paintings showing Johann Sebastian Bach, in the center the new piece (above) and the position of the painting ready for XRF-analysis at BL 10 / DELTA (below).

By Roland Beage/TU-Dortmund 2015.

The first characterization of selected areas (showing white paint) showed that the two issues of Eisenach contain only Pb. This fact can be regarded as there is only lead used in the white painted areas. The situation is quite different in the new discovered work. There we detected Zn and Ba in

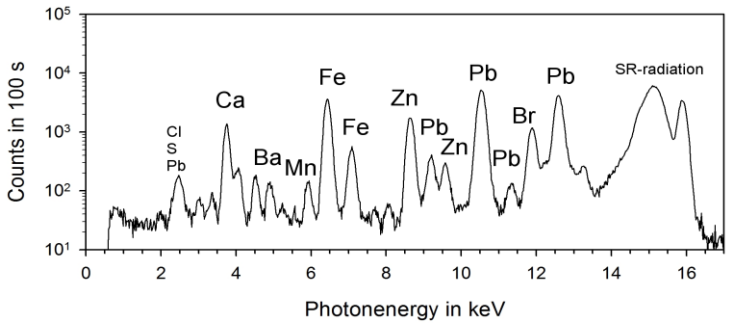

X-ray fluorescence spectrum of the third painting of J. S. Bach showing strong Zink and Barium signals

a white area. We could not exclude the possibility of analyzing a retouched region of the hair. Therefore, we applied for a second beamtime in which more accurate results of different well defined areas of the painting will be analyzed carefully.

As the painting is applied on parchment we will excite to fluorescence in transmission geometry. This will also allow a simultaneous detection of X-ray diffraction and fluorescence as well. In such a way we will be able to confirm or decline the presence of Lithopone or other compounds.

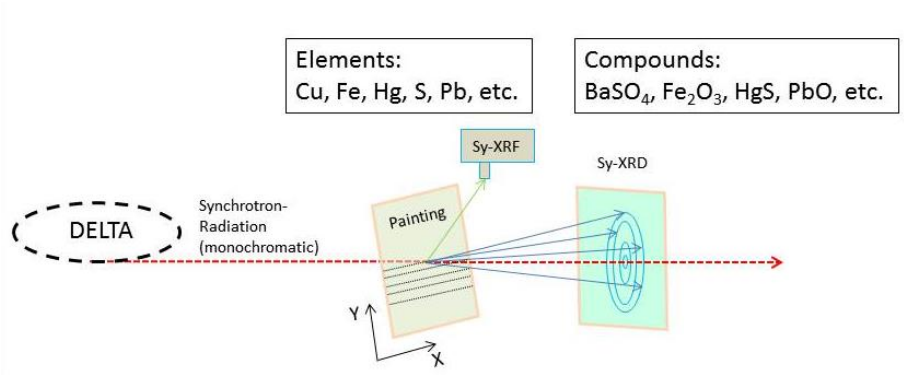

Set-up for the analysis in transmission mode of a Bach painting. Record of simultaneous detection of fluorescence and diffraction pattern is intended.

The authors thank the DELTA staff for support and for supplying beamtime.

NiAl formation in Ni-Al-multilayers studied by temperature dependent grazing incidence EXAFS measurements

Dirk Lützenkirchen-Hecht, Khalid Maadour, Ralph Wagner, Ronald Frahm

Fachbereich 4 - Physik, Bergische Universität Wuppertal, Gaußstr. 20, 42097 Wuppertal, Germany.

Grazing incidence X-ray absorption spectroscopy is an excellent method to study the near surface structure of thin films, surfaces, adsorbates etc. (e.g. refs. [1-5]) and it has also been used in the past for the investigation of intermetallic layers [1]. Here we have *in-situ* explored the formation of NiAl induced by a heat treatment of Al-Ni-multilayers in vacuum using Ni K-edge XAFS. The samples were prepared by thermal evaporation of Al and Ni on float glass substrates under high-vacuum [6]. X-ray reflectivity measurements were used to determine the thickness of the Al and Ni layers in the multilayers, and grazing incidence X-ray absorption spectroscopy provides *in-situ* information about the structure of the nickel with the multilayers. For those experiments, a high temperature cell (Anton Paar DCS 1100) was installed on the diffractometer of beamline 10.
As can be seen in Fig. 1, the measured XAFS data of an Al/Ni/Al-trilayer on glass closely resembles the spectrum of metallic Ni (fcc structure) for temperatures below 200°C. Due to the grazing incidence geometry, the amplitude of the EXAFS oscillations is smaller compared to the Ni foil measured in transmission. NiAl formation starts at about 210°C, resulting in XAFS structures very similar to those of polycrystalline bcc NiAl. The data obtained at T = 210°C were measured for two different incidence angles with different penetration depth, however without any noticeable changes of the XAFS oscillations. This results suggests that the originally about 40 nm thick Ni layer has completely transformed into the bcc NiAl phase during the heat treatment at 210°C [6].

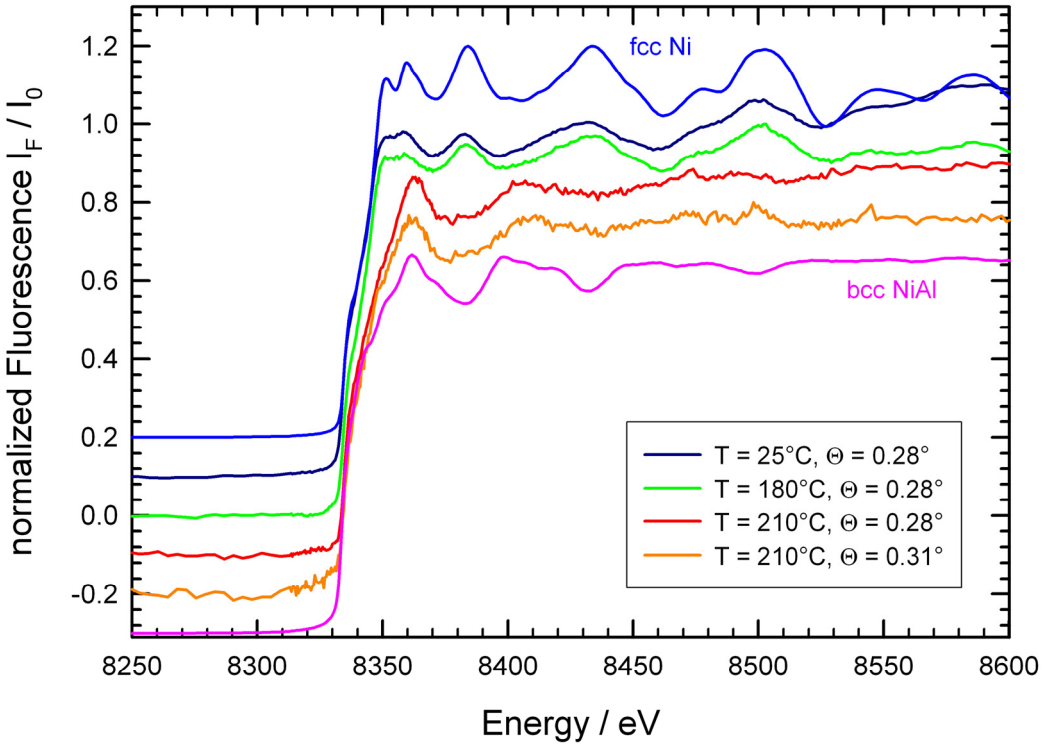

Fig. 1: Grazing incidence XAFS at the Ni K-edge measured *in-situ* during the annealing of a Al (40 nm) / Ni (40 nm) /Al (40 nm) - trilayer on a glass substrate for different incidence angles Θ and temperatures as indicated. The presented X-ray absorption spectra were measured in fluorescence mode using a large area PIPS diode. For comparison, the spectrum of a Ni-metal reference foil with fcc-structure and the bcc NiAl intermetallic compound are also shown.

In Fig. 2, in-situ measured XAFS spectra for different incidence angles Θ are displayed for an Al-Ni-bilayer system, consisting of 80 nm Al on 72 nm Ni on the glass substrate heated to a substrate temperature of 230°C. Again, spectra of the NiAl reference sample and Ni metal are shown for comparison. As can be seen, the XAFS data from the heated bilayer sample closely resemble that of the NiAl reference for incidence angles below the critical angle of total reflection of Ni, while they are dominated by XAFS fine structure of Ni metal for larger incidence angles $\Theta > 0.35°$. The present results suggest that a thin NiAl-film has formed at the interface between the metallic Al- and Ni-sublayers. In contrast to the experiment described above, only a smaller fraction of the Ni sublayer has reacted to NiAl. From a fit of the experimental data, the thickness of this layer can be estimated to about 20 nm. Experiments at more elevated temperatures show that the NiAl film thickness is not increasing further, and it should also be noted that no evidence for other Ni-Al compounds such as $NiAl_2$, Ni_2Al_3 etc. could be obtained in the present study.

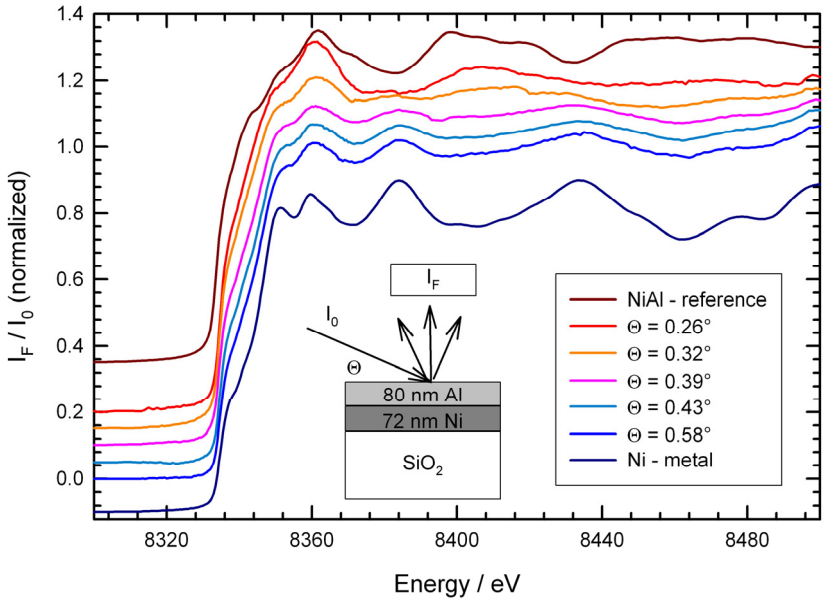

Fig. 2: Grazing incidence XAFS at the Ni K-edge measured *in-situ* during the annealing of a Al/Ni-bilayer on a glass substrate at T = 230°C. X-ray absorption spectra were measured in fluorescence mode using a large area PIPS diode for different incidence angles Θ as indicated in the inset. For comparison, the spectrum of a NiAl intermetallic compound and a Ni-metal reference are also shown.

Additional experiments with smaller film thickness of the Ni sublayer also indicated that those films may already transform to NiAl below a critical thickness of about 20 nm during the preparation in the high-vacuum system. Thus the Ni-Al-multilayers represent a metastable phase, depending on the actual thickness of the Ni layers. A more detailed publication is currently in preparation.

References

[1] S.M. Heald, H. Chen and J.M. Tranquada, Phys. Rev. B 38 (1988) 1016
[2] P. Borthen and H.-H. Strehblow, J. Phys.: Condens. Matter 7 (1995) 3779
[3] D.T. Jiang and E.D. Crozier, Can. J. Phys. 76 (1998) 621
[4] F. d'Acapito, I. Emelianov, A. Relini, P. Cavatorta, A. Ghiozzi, V. Minicozzi, S. Morante, P.L. Solari and R. Rolandi, Langmuir 18 (2002) 5277
[5] D. Lützenkirchen-Hecht, D. Wulff, R. Wagner, R. Frahm, U. Holländer and H.J. Maier, J. Mater. Sci. 49 (2014) 5454
[6] K. Maadour, Diploma Thesis, University of Wuppertal (2015).

Multi-edge XAFS investigation of Y-Fe-Ca-garnets

Dirk Lützenkirchen-Hecht, Stefan Balk, Ralph Wagner

Fakultät 4-Physik, Bergische Universität Wuppertal, Gaußstr. 20, 42097 Wuppertal, Germany

The increasing demands e.g. in catalysis, energy storage and conversion, magnetic data storage devices, microelectronics etc. have led to numerous materials with unique physico-chemical properties in the past few years. Those tailored materials usually have a complex, multi-elemental structure which needs to be analysed in order to understand and predict their properties. Using standard laboratory techniques such as e.g. X-ray diffraction (XRD) alone, it is in many cases not possible to achieve a complete description of those materials, and X-ray absorption fine structure spectroscopy (XAFS) may in those situations a valuable technique, since it is able to probe the local environment of a selected element within the sample [1]. Furthermore, XAFS also gives information about the chemical valence of the investigated elements, and it is thus extremely useful if several absorption edges of the investigated material can be analysed.

In the present contribution, we will report on the analysis of Ca-doped Y-Fe-garnets of the compositions $Y_{(3-x)}Ca_xFe_5O_{12}$ and $0 \leq x \leq 0.5$ [2, 3]. The undoped ferrogarnet has a cubic structure (space group 230, Ia3d) with a lattice parameter a = 12.3835 Å [3], and doping of this material with Ca^{2+} should result to the formation of Fe^{4+} according to $Ca_x^{2+}Y_{3-x}^{3+}\ Fe_2^{3+}\ Fe_{3-x}^{3+}Fe_x^{4+}\ O_{12}^{2-}$, i.e. dodecahedral Ca^{2+} and Y^{3+}, octahedral Fe^{3+}, and tetrahedral Fe^{3+} and Fe^{4+} in stoichiometric amounts [4]. The samples investigated here were prepared by pyrolysis. Nitrates of a certain composition were mixed with glycine to obtain a homogeneous viscous gel. This gel was heated to 600°C in order to combust the nitrates. The obtained friable composite-powders were pressed in the form of tablets and subsequently annealed in air at 900°C for 5 hours. They were slowly cooled to room temperature in the furnace and subsequently investigated with XAFS experiments at DELTA beamline 8, making use of the large spectral range and the different monochromators available at this beamline [5]. While the Si(311) monochromator was used for the experiments at the Y K-edge (17038 eV), a Si(111) monochromator was employed for the Fe K-edge (7112 eV), and InSb(111) and Si(111) were used for the Ca K-edge (4040 eV). While transmission mode experiments using gas-filled ionization chambers were conducted at the Fe and Y K-edges, fluorescence detection using a large area passivated implanted Si detector was employed at the Ca K-edge.

In Fig. 1, a typical XAFS spectrum of the pure $Y_3Fe_5O_{12}$ is shown. The small pre-peak at the edge and the edge position of ca. 7121 eV are typical for an octahedral Fe^{3+}-oxide. In the insert, the edge positions observed for several doped samples are compiled as a function of the Ca-content. A small but clear trend towards larger edge position can be stated, which is in accordance with the increasing presence of Fe^{4+} with Ca-doping. An unambiguous assignment and a calculation of the Fe^{4+}-concentration is however not straightforward due to the possible change of the Y^{3+} and Ca^{2+}-valence during doping, and thus XAFS experiments at the Y and Ca K-edges are important for a detailed understanding of the observed changes in the spectra (see Figs. 2 and 3).

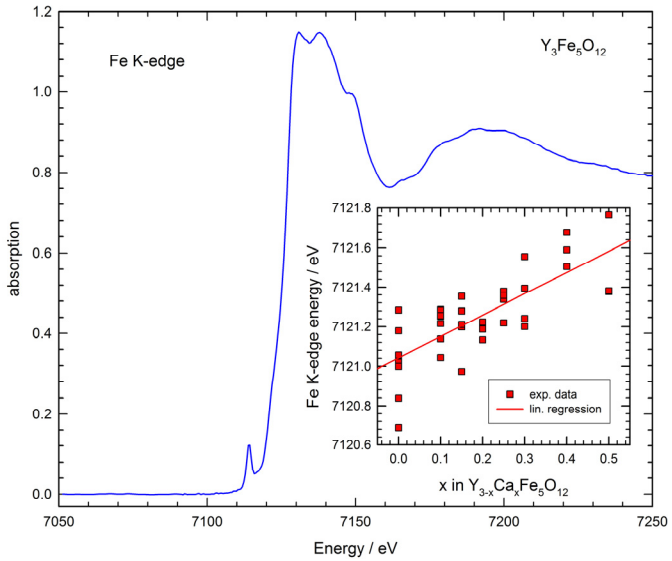

Fig. 1. Fe K-edge XAFS spectrum of the Yttrium-Iron garnet $Y_3Fe_5O_{12}$ measured using the Si(111) monochromator at beamline 8. The small pre-edge peak at 7112 eV as well as the edge position at 7121 eV are typical for octahedral Fe^{3+}. In the insert, the edge position observed for all the investigated, Ca-doped ferrogarnet samples are summarized. The increase of the edge energy with increasing Ca-doping is evident, suggesting the presence of Fe^{4+} in increasing amounts.

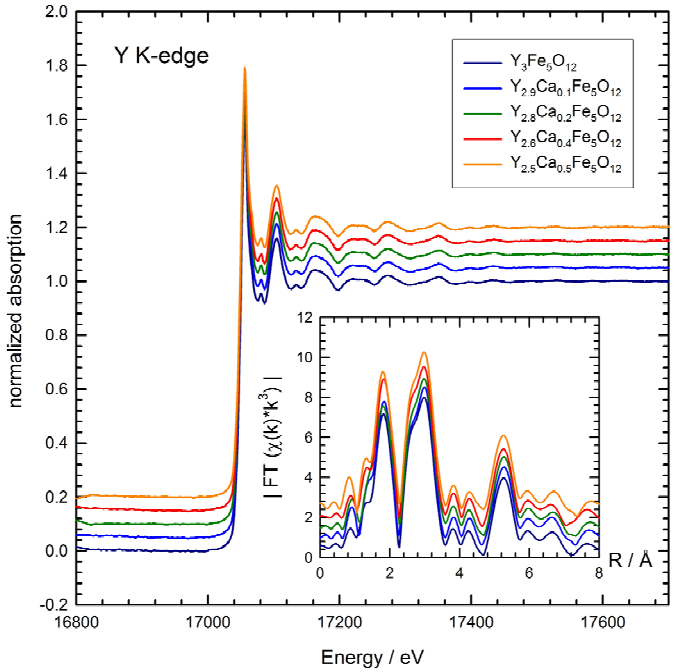

Fig. 2. Y K-edge XAFS spectra measured using the Si(311) monochromator of beamline 8 for Ca-doped Yttrium-Iron garnets $Y_{(3-x)}Ca_xFe_5O_{12}$ and various different Ca-concentrations as indicated. From the invariant shape of the spectra, their edge position and the Fourier-transforms of the extracted k^3-weighted EXAFS fine structures $\chi(k)*k^3$ shown in the insert, it can be concluded that the structure and valence of the Y in the Ca-doped garnet does not substantially change for increasing Ca-concentrations.

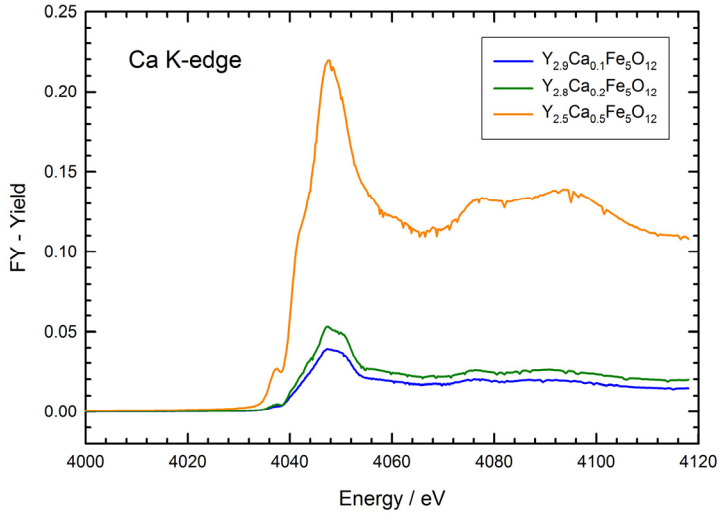

Fig. 3. Ca K-edge XAFS spectra measured using the InSb(111) monochromator of beamline 8 for Ca-doped Yttrium-Iron garnets $Y_{(3-x)}Ca_xFe_5O_{12}$ and various different Ca-concentrations as indicated. The increase of the edge jump with increasing Ca-concentration and the constant edge energy are evident.

From the measured spectra at the Y and Ca K-edges, we are now able to assign the changes observed at the Fe K-edge entirely to the formation of Fe^{4+} during increasing Ca-doping, and a more detailed analysis, especially the comparison with edge positions from other Fe-O compounds with well-known chemical valence, provides the concentration of Fe^{4+}. The results show that the increase of Fe^{4+} concentration meets well the expectation of a charge-balanced incorporation of Ca^{2+} into the lattice of the garnet. A more detailed analysis of the EXAFS data measured at the Fe and Y edges, yielding the Fe-O and Y-O distances and coordination numbers, is currently under way.

Acknowledgements

We would like to thank M. Bulatov (*Astrakhan State University, Astrakhan, 414056, Russia*) for the provision of the garnet samples, and the DELTA machine group for the reliable beam delivery and experimental support.

References

[1] D. Koningsberger, R. Prins, X-Ray Absorption: Principles, Applications, Techniques of EXAFS, SEXAFS and XANES; Wiley, New York (1988)
[2] C. Borghese, R. Cosmi, P. de Gasparis, R. Tappa, Thin Solid Films 51 (1978) L35.
[3] M. Bonnet, A. Delapalme, H. Fuess, M. Thomas, Acta Cryst. B 31 (1975) 2233.
[4] K. Nassau, J. Crystal Growth 2 (1968) 215
[5] D. Lützenkirchen-Hecht, R. Wagner, U. Haake, A. Watenphul, R. Frahm, J. Synchrotron Rad. 16 (2009) 264.

X-ray absorption studies of Niobium and NbN as references for nitration studies of Nb

Jonas Kläs, Benjamin Bornmann, Dirk Lützenkirchen-Hecht, Ralph Wagner, Ronald Frahm

Fakultät 4 - Physik, Bergische Universität Wuppertal, Gaußstr. 20, 42097 Wuppertal, Germany.

Nb is widely used as material for superconducting radio-frequency (SRF) cavities - a key enabling technology for high-energy and high-beam-power accelerators envisioned world-wide. Applications range from particle and nuclear physics to radiation therapies in medicine, and characterizations of chemical or biological samples. One of the main goals is the optimization of the quality factor Q_0 of the cavities (Q_0 = ratio of stored energy in the cavity to dissipated power per RF cycle) in order to minimize the power consumption of future accelerators. Recently, a heat treatment of the Nb-cavities in nitrogen atmospheres showed promising results, with an enhancement of Q_0 by up to a factor of 3 [1-2]. While the formation of NbN phases was discussed, however, a clear relation between the structure of the so-treated Nb materials and the quality factor could not yet be achieved and is a matter of debate.
Therefore temperature and time dependent X-ray absorption fine structure (XAFS) experiments will be performed, and, Nb and NbN reference materials were investigated at the Nb K-edge (18.986 keV) using synchrotron radiation from DELTA beamline 8 [3]. The absorption spectra were collected in transmission mode using Ar-and Xe-filled ionization chambers as detectors for the incident and transmitted intensities and a Si(311) monochromator. While Nb-metal was present in the form of high-purity foils of different thickness, the NbN powder sample was prepared using several layers on sticky Kapton tape. The data merged for each material are shown in Fig. 1 and present clearly distinguishable XAFS-signals for both phases. Besides a small chemical shift of the absorption edge to a larger value, especially the measured fine structures above the edge are clearly different.

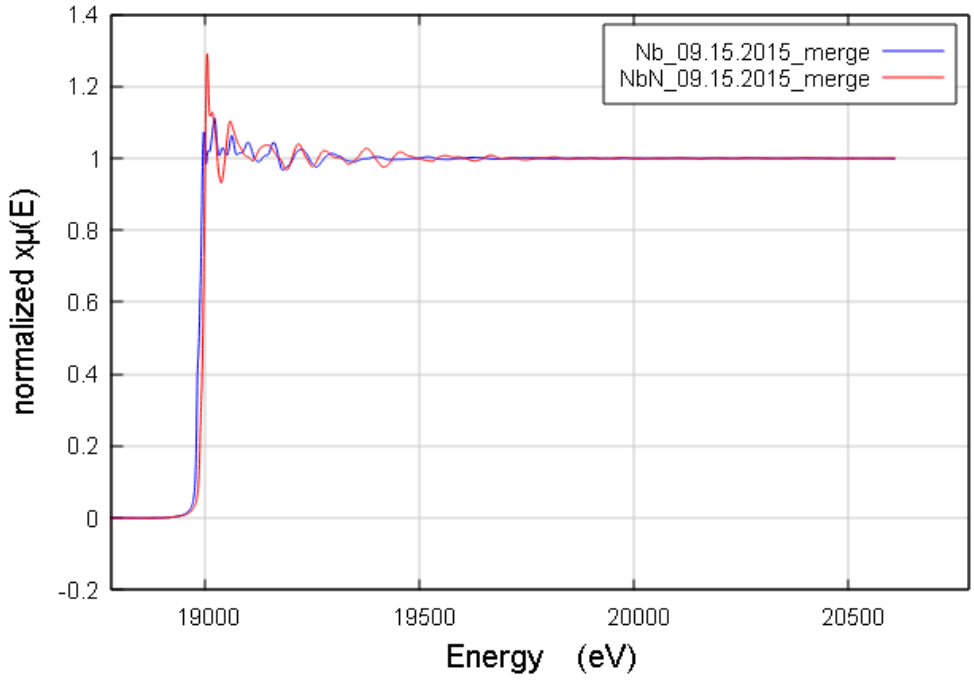

Fig. 1: Merged XAFS data of Nb and NbN obtained using the Si(311) monochromator at DELTA beamline 8. Both data sets were analysed using the software DEMETER [4].

Using a body centered cubic crystal structure model for the Feff calculation for Nb-metal, Fig. 2 shows that this model corresponds well to the measured Nb data, with a cell parameter

of (3.316 ± 0.001) Å, which is well in agreement with literature data [5]. In the case of NbN, two possible structure models were evaluated: Nb being in a face-centered cubic configuration inside the NbN, and the Wurtzite structure. From the comparison of the best fits, the Wurtzite structure seems to be more appropriate for the structure description of the investigated NbN-sample (Fig. 3).

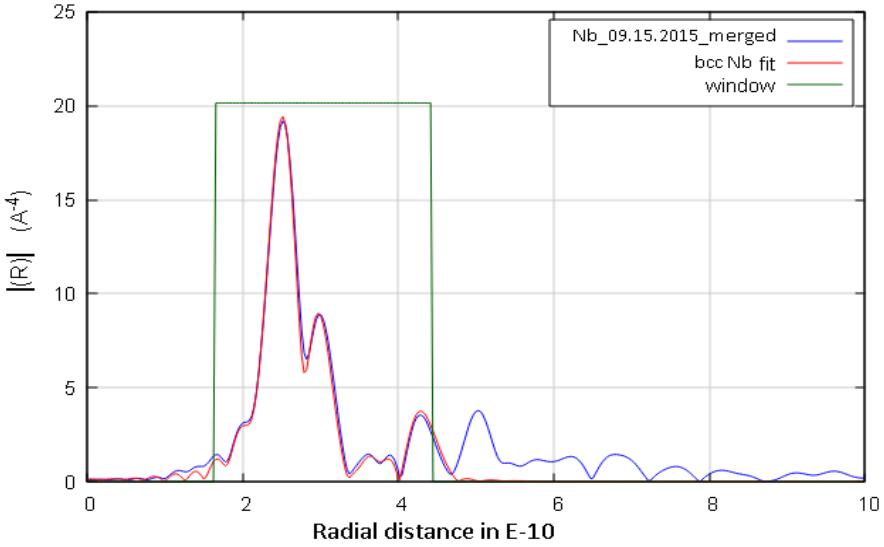

Fig. 2: Magnitude of the Fourier-transform of the k^3-weighted fine structure oscillations of Nb-metal fitted with a bcc structure model in DEMETER (k-range for the Fourier-transform 3.0 $Å^{-1} \leq k \leq 16.9$ $Å^{-1}$).

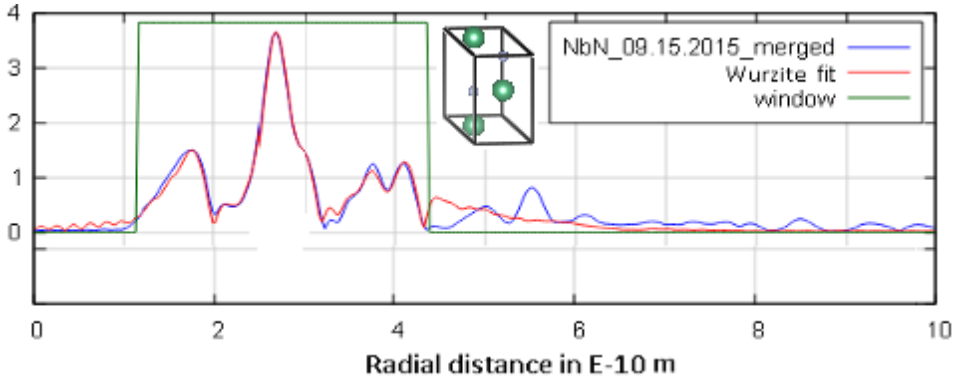

Fig. 3: Magnitude of the Fourier-transform of the k^3-weighted fine structure oscillations of NbN fitted with two different structure models each with 11 scattering paths. The fit was performed using the Wurtzite structure k-range for the FT 3.0 $Å^{-1} \leq k \leq 19.5$ $Å^{-1}$).

As both reference materials Nb and NbN are clearly distinguishable in the shape of their XAFS data, it can be expected that XAFS measurements are well suited to follow nitration processes in situ. Additional reference samples of different NbN structures and possibly also various niobium oxides Nb_xO_y or oxynitrides $Nb_xN_yO_z$ may be required as well.

References

[1] A. Grasselino, et al., Supercond. Sci. Technol. 26 (2013) 102001.
[2] P. Dhakal, et al, Phys. Rev. Special Top. Acc. Beams 16 (2013) 42001.
[3] D. Lützenkirchen-Hecht, et al. J. Synchrotron Rad. 16 (2009) 264–272.
[4] B. Ravel and M. Newville, J. Synchrotron Rad. 12 (2005) 537–541.
[5] C. Kittel, Introduction to solid state physics, Wiley, New York (1971).

Notes

Notes